Computational Study of and Model Development for Morphological Evolution in Metallic-Nanostructure Heteroepitaxy

by

Nirand Pisutha-Arnond

A dissertation submitted in partial fulfillment
of the requirements for the degree of
Doctor of Philosophy
(Materials Science and Engineering)
in The University of Michigan
2013

Doctoral Committee:

Associate Professor Katsuyo Thornton, Chair
Professor Mark Asta, The University of California, Berkeley
Professor Ken Elder, Oakland University
Professor Michael Thouless
Associate Professor Anton Van der Ven

For my family and my high-school english teacher

ACKNOWLEDGEMENTS

I am grateful to my thesis advisor Prof. Katsuyo Thornton for providing me support and guidance as well as being very patient with me for many years. Without her, I would not have been able to complete my PhD. Without her, I would not have learnt what it takes to be a scientific scholar. I am indebted to my committee members, Prof. Mark Asta, Prof. Ken Elder, Prof. Michael Thouless, and Prof. Anton Van der Ven, for reading my thesis and providing many constructive and valuable comments on my work. I would like to thank the following project collaborators for lending their expertise and for making the work in this thesis possible: Prof. Mark Asta, Prof. Ken Elder and Prof. Vikram Gavini. Furthermore, I would like to thank my current and past colleagues for their useful discussions and support Roberto, Dong-Hee, Hui-Chia, Hsunyi, Larry, Victor, Chal, Chloe, Steve, Bernardo, Nick, Amber, Candace, Susan, Tapiwa, Andrea, and Britta. In additional, I would like to acknowledge the funding support from the National Science Foundation and the Thai Scholar fellowship. Also, I am thankful to Prof. Elizabeth Hildinger for helping me with my English writing. I would not have been able to go through my PhD study without support and encouragement from my parents and my sister. Lastly, I would like to thanks all Thai people that I have met in Ann Arbor for their friendship and fond memories.

TABLE OF CONTENTS

DEDICATION ii

ACKNOWLEDGEMENTS iii

LIST OF FIGURES vii

LIST OF TABLES xi

LIST OF APPENDICES xiii

ABSTRACT xiv

CHAPTER

I. Introduction 1

1.1 The First Contribution: Investigation of a Thermodynamic Driving Force for Dewetting of Magnetic Thin Film with Misfit Dislocations 5
1.2 The Second Contribution: Numerical Techniques to Improve the Phase-Field Crystal Method and Classical Density Functional Theory 7
1.3 The Third Contribution: Calculations of Isothermal Elastic Constants in the Phase-Field Crystal Method 11

II. Background 13

2.1 Overview 13
2.2 Continuum Models of Dislocations and Misfit Dislocations . . 13
2.2.1 The Volterra Model 14
2.2.2 The Peierls-Nabarro Model 19
2.2.3 Van der Merwe Models 26
2.2.4 Film-Substrate Potential 34
2.3 Overview of the Phase-Field Crystal Model 36
2.3.1 Phenomenological Development 36

2.3.2 Theoretical Development 41
2.4 Further Development of the Phase-Field Crystal Model 48
2.4.1 Extension of Free Energy 49
2.4.2 Evolution Equation 50
2.4.3 Coarse-graining of the PFC equations using Amplitude Formulations 52

III. Stability of Strained Thin Films with Interface Misfit Dislocations: A Multiscale Computational Study 54

3.1 Overview 54
3.2 Formulation 55
3.2.1 Energy Considerations 57
3.2.2 Homogeneous Strain Energy 57
3.2.3 Dislocation Elastic Energy 59
3.2.4 Plastic Deformation Energy 63
3.2.5 Surface/Interfacial Energy 63
3.3 Results and Discussions 68
3.3.1 Dislocation Configuration 68
3.3.2 Dislocation/Deformation Energy 70
3.3.3 Effect of Surface Stress 72
3.3.4 Dislocation/Deformation and Surface/Interfacial Energies 74
3.3.5 Applicability to Other Systems 77
3.4 Chapter Summary 78

IV. Modeling Classical Density Functional Theory and the Phase-Field Crystal Method using a Rational Function to Describe the Two-body Direct Correlation Function 79

4.1 Overview 79
4.2 Background and Motivation 80
4.2.1 Classical Density Function Theory of Freezing . . . 80
4.2.2 Phase-Field Crystal Method 82
4.3 Rational Function Fit 84
4.4 Examining the Role of Short-Wavelength Contributions of the Two-Body Direct Correlation Function 85
4.4.1 The Rational Function Fits of the Two-Body Direct Correlation Function of Fe 85
4.4.2 Procedures to Calculate Solid-Liquid Properties . . 86
4.4.3 Results and Discussions 88
4.5 Empirical Parametrization of the Two-Body Direct Correlation Function 92
4.6 Application of RFF to the PFC Method 96
4.7 Real-Space Implementation 99

4.8 Comparison of Fourier-Space and Real-Space Implementations 103
4.9 Chapter Summary and Discussions 107

V. Calculations of Isothermal Elastic Constants in the Phase-Field Crystal Model 109

5.1 Overview 109
5.2 Background 111
5.2.1 PFC Method 111
5.2.2 Measure of Deformation 112
5.2.3 Definitions of Isothermal Elastic Constants from the Thermoelasticity Theory 114
5.2.4 Deformation Types 116
5.3 Calculations of Isothermal Elastic Constants using PFC Free Energy 119
5.3.1 PFC Elastic Constants 119
5.3.2 TE Elastic Constants 121
5.3.3 Numerical Comparison Between PFC and TE Elastic Constants 123
5.4 A General Procedure to Obtain the PFC Elastic Constants . 127
5.5 Thermodynamics of Stressed Solids 129
5.5.1 Formulation 129
5.5.2 Taylor Expansions of Energy Functions 132
5.5.3 Relationships Between the Coefficients of Taylor Expansions 134
5.6 Chapter Summary 138

VI. Conclusion 141

VII. Future Work 143

APPENDICES 144

BIBLIOGRAPHY 152

LIST OF FIGURES

Figure

2.1 A single edge dislocation in a cylinder. This figure has been reproduced from Ref. [96]. 15

2.2 (a) Two semi-infinite cubic crystals with disregistry of $b/2$. (b) Distortion of the crystal after an introduction of the dislocation. The figures have been reproduced from Ref. [96]. 20

2.3 Misfit dislocation at an interface between an infinitely-thick substrate and a finite-thickness film 28

3.1 Contour plot of $(E_{gsfe} - E_0)/V$ showing the BCC(110) substrate potential. The constant r is the nearest-neighbor spacing. The dash lines enclose one unit cell. 61

3.2 Minimum-energy dislocation spacing considering only the dislocation/deformation energy as a function of film thickness for the (a) Fe/Mo(110) and (b) Fe/W(110) systems. The dislocation spacing is normalized by the substrate lattice spacing (SLS). The film thickness is measured in atomic layers (AL). The arrow indicates that the dislocation spacing is infinitely large. The inset in (a) shows the dislocation/deformation energies of misfit dislocations with the spacings of 10 and 11 SLS versus 11 and 10 SLS along $[\bar{1}10]$ and $[00\bar{1}]$ directions, respectively, in the Fe/Mo system. The intersection between the two energy curves occurs between the film thickness of 17 and 18 AL. 67

3.3 (a) Dislocation/deformation energy per surface atom (in eV) associated with the minimum-energy dislocation configurations as a function of film thickness. (b) Dislocation/deformation energy of the Fe/Mo system from the film thickness of 2-6 AL. The chord construction illustrates local instability of the film with the thickness of 4 AL. 71

3.4 (a) Minimum-energy dislocation spacing, considering the surface stress effect for the Fe/Mo system. (b) Surface/interfacial energy (in eV/surface atom) of the Fe film on the Mo(110) substrate as a function of the film thickness. The solid line (square markers) denotes the surface/interfacial energy of the pseudomorphic film. The dash line (circular markers) denotes the strain-dependent surface/interfacial energy of the dislocated film. 73

3.5 The combination of dislocation/deformation and surface/interfacial energies for the Fe/Mo system. (a) Film thickness from 1-10 AL. (b) Film thickness from 1-3 AL. The chord construction illustrates a metastability behavior of the thin film with the thickness of 2 AL. . 75

4.1 The different fits to the embedded-atom-method molecular dynamics (EAM-MD) data, $\hat{C}^{(2)}_{MD}$ [175]. (a) The rational function fits (RFFs) with different number of terms. (b) A magnified section of (a). (c) The fourth-order fit (4P) and the eighth-order fit (8P) [153, 121]. . 87

4.2 The normalized free energies per unit volume of the BCC solids corresponding to different fits of the EAM-MD data. The blue-solid line denotes the liquid free energy density curve whereas the other lines denote the solid free energy density curves. (a) Free energies of the BCC solids from the CDFT simulations using the EAM-MD data, the 9R, the 7R and the 5R. The cross signs at the solid curves denote the solid densities at the solid-liquid coexistence. (b) Free energies of the BCC solids from the CDFT simulations using the 8P and the 3R. The two cross signs show the solid densities at the solid-liquid coexistence. 90

4.3 The BCC solid-liquid density profiles along the direction normal to the (110) plane (z-axis), where a_{BCC} is the lattice spacing. Here, $\langle n \rangle = A^{-1} \int \int n(x, y, z) dxdy$, where A is the surface area and n_l is the normalized liquid density at the solid-liquid coexistence. The arrows indicate the amplitude of the fluctuation in the bulk solid region of the density profiles. 91

4.4 The density profiles on the (100) crystal plane of the BCC solids at the solid-liquid coexistence, where a_{BCC} is the lattice spacing. It should be noted that the vertical scales of (e) and (f) are different from the others. 93

4.5 The normalized free energies per unit volume of the BCC and FCC solids from the CDFT simulations using the EAM-MD data, the 9R, the 7R, and the 5R. The 5R-BCC and 5R-FCC curves do not intersect. The solid free energies are evaluated from the semi-analytical method described in Section 4.4.2. The blue solid curves denote the liquid free energy. 94

4.6 (a) The comparison between the 5R and the M5R. The two fits are similar except for the second peak of the M5R being slightly higher. The solid line denotes the EAM-MD data. (b) The comparison between the normalized BCC solid free energy densities from the CDFT simulations using the EAM-MD data, the 9R, and the M5R. The cross signs indicate the solid densities at solid-liquid coexistence. The cross signs on the M5R and EAM-MD free energy curves nearly coincide at the current graphical scale. 95

4.7 The ideal contribution to the free energy as a function of the normalized density. The solid line denotes the ideal contribution from Eq. (4.3) while the dash line denotes the approximation from Eq. (4.5), where $a_t = 0.6917$ and $b_t = 0.0854$ [121]. (b) The density profile on the (100) crystal plane of the BCC solid from the simulation using the 3R and the ideal contribution represented by the dash line in (a). 98

4.8 The different fits to the EAM-MD data (solid line) using the combined rational and polynomial functions. From the label, "2^{nd} Order Poly." denotes the fits that include up to k^2 in Fourier space and "4^{th} Order Poly." denotes those including k^2 and k^4 terms. The label "Terms" refers to the number of partial fraction terms in Eq. (4.14). 99

4.9 (a) The comparison between the 8P and the 3R2P. The solid line denotes the EAM-MD data. (b)-(c) The density profiles on the (100) crystal plane of the BCC solids at the solid-liquid coexistence from the PFC simulations using the 3R2P (b) and the 8P (c). (d) The difference between the density profiles of the 3R2P and 8P PFC simulations, where the profile of the 8P PFC is subtracted from that of the 3R2P PFC. 100

4.10 (a) The difference between the solid free energy densities calculated from the M5R CDFT simulations using the CIJ/SIJ method and the numerically converged reference value. The reference value is calculated from the M5R CDFT simulation using the Fourier spectral method at a fine grid spacing of $\Delta h = a_{BCC}/256$. (b) The plot of $n(\mathbf{r})$ showing the interface between liquid and BCC solid from the M5R CDFT simulation using the CIJ/SIJ method. 103

5.1 The plots of different sets of elastic constants and hydrostatic pressure as functions of ϕ_{ave}, or equivalently ϕ'_{ave}. (a) The PFC elastic constants. (b) The TE elastic constants in the nonlinear elasticity theory. (c) The TE elastic constant in the linear elasticity theory. (d) The hydrostatic pressure of the undeformed state. 126

5.2 The plots of elastic constants as functions of ϕ_{ave}, or equivalently ϕ'_{ave}. The elastic constants $\mathcal{C}^{fp1}_{\alpha\beta}$ and $\mathcal{K}^{fp1}_{\alpha\beta}$ are calculated from the procedure described in Section 5.3.2, which is similar to how the TE elastic constants are obtained. The elastic constants $\mathcal{C}^{fp2}_{\alpha\beta}$ and $\mathcal{K}^{fp2}_{\alpha\beta}$ are obtained from Eqs. (5.54) and (5.55) which in turn employ the values of $\mathcal{C}^{g}_{\alpha\beta}$ and $\mathcal{K}^{g}_{\alpha\beta}$ calculated from the procedure in Section 5.4. 140

LIST OF TABLES

Table

4.1 The comparison of the liquid and solid properties computed from the CDFT simulations using different fits of the EAM-MD data, $\hat{C}^{(2)}_{MD}(k)$. The liquid and BCC-solid densities shown are at solid-liquid coexistence, and the expansion in melting is for the BCC solid. The abbreviations S, MS, and NS denote "stable," "metastable," and "not stable," respectively (see text). The data are rounded to three significant digits. The comparison between the predictions from the CDFT simulations using $\hat{C}^{(2)}_{MD}(k)$ and those from MD and experimental data can be found in Ref. [121] and therefore is not included. 92

4.2 The liquid and solid properties computed from the M5R CDFT simulations, along with the 5R and 9R CDFT simulation results from Table 4.1. 96

4.3 Comparison of the 8P and the 3R2P: the long-wavelength limit, $\hat{C}^{(2)}(0)$, the location of the first peak, k_m, and the curvature of the first peak, $d^2/dk^2\left[\hat{C}^{(2)}(k_m)\right]$. 99

4.4 The comparison of the convergence values at different time step sizes using the backward Euler time stepping scheme. These values are evaluated at $\tau = 0.2$. 106

5.1 A list of (i) types of deformation, (ii) functional forms of density profiles in terms of the deformed coordinates, $\phi\left(\boldsymbol{\alpha}^{-1}\cdot\mathbf{r}\right)$, (iii) expressions for the integration over the deformed unit cell, and (iv) the deformed volume of the unit cell, $V_n(\xi)$. The unit cell is cubic with a side length of L_a in the undeformed state. 118

5.2 The elastic constants of BCC Fe at the melting point. The unit of the elastic constants is GPa. (i) The PFC elastic constants calculated in this work using slightly different parameters from those in Ref. [78] (see text). (ii) The TE elastic constants in the nonlinear elasticity theory. (iii) The TE elastic constants in the linear elasticity theory. (iv) The PFC elastic constants reported in Ref. [78]. (v) The elastic constants predicted by the MD simulations [78]. For (i) to (iv), the elastic constants are evaluated at $\phi_{ave} = -0.201$. 127

LIST OF APPENDICES

Appendix

A. Gaussian Approximation of Density Profiles 145

B. Taylor Expansion of the Helmholtz Free Energy 147

C. Calculations of $K_{\alpha\beta}$ 150

ABSTRACT

Computational Study of Morphological Evolution in Metallic-Nanostructure Heteroepitaxy

by

Nirand Pisutha-Arnond

Chair: Katsuyo Thornton

In this thesis, we describe computational studies relevant to morphological evolution in metallic-nanostructure heteroepitaxy. Our first contribution focuses on the understanding of the thermodynamic driving force behind morphological evolution of the magnetic thin-film system. Specifically, we study the stability of thin single-crystal, internal-defect-free Fe films on Mo(110) and W(110) substrates through calculations of energetics including contributions from the misfit strain, interfacial misfit dislocations, film surface and interface. The misfit dislocation model is developed through the Peierls-Nabarro framework, employing *ab initio* calculations of the corrugation potential at the film/substrate interface as an input to the model. The surface and interfacial energies for pseudomorphic films are calculated as a function of film thickness from 1 to 10 layers, employing first-principles spin-polarized density-functional theory calculations in the generalized gradient approximation. First-principles calculations are also employed to obtain the Fe surface stress used in the Peierls-Nabarro model to account for the strain dependence of the surface energy. It is found that the

competition between the misfit strain, misfit dislocations, film surface and interfacial energies gives rise to a driving force for solid-state dewetting for a single-crystal, internal-defect-free film, i.e., an instability of a flat film that leads to formation of thicker and thinner regions. The details of the energetics are presented to demonstrate the robustness of the mechanism. Our findings indicate that misfit dislocations and their configurations play a significant role in a morphological evolution of metallic thin films.

Our second contribution lies in the development of numerical methods for the classical density functional theory (CDFT) and the phase-field crystal (PFC) method, both of which are promising tools for modeling metallic-nanostructure hetereoepitaxy. We introduce a new approach to represent a two-body direct correlation function (DCF) in order to alleviate the computational demand of CDFT and enhance the predictive capability of the PFC method. The approach utilizes a rational function fit (RFF) to approximate the two-body DCF in Fourier space. We use the RFF to show that short-wavelength contributions of the two-body DCF play an important role in determining the thermodynamic properties of materials. We further show that using the RFF to empirically parameterize the two-body DCF allows us to obtain the thermodynamic properties of solids and liquids that agree with the results of CDFT simulations with the full two-body DCF without incurring significant computational costs. In addition, the RFF can also be used to improve the representation of the two-body DCF in the PFC method. Lastly, the RFF allows for a real-space reformulation of the CDFT and PFC method, which enables descriptions of nonperiodic systems and the use of non-uniform/adaptive grids.

Our third contribution involves an investigation on how to parameterize the PFC method in a thermodynamically consistent manner; this is important to ensure robust predictions from the model. For this work, we examine procedures for calculating isothermal elastic constants using the PFC method. We find that the conventional

procedure used in the PFC method for calculating the elastic constants are inconsistent with those defined from a theory of thermoelasticity of stressed materials. Therefore, we present an alternative procedure for calculating the elastic constants that are consistent with the definitions from the thermoelasticity theory, and show that the two procedures result in different predictions. Furthermore, we employ a thermodynamic formulation of stressed solids to quantify the differences between the elastic constants obtained from the two procedures in terms of thermodynamic quantities such as the pressure evaluated at the undeformed state. The second and third contributions together will provide necessary modeling capability for quantitative and accurate simulations of morphological evolution in metallic thin films.

CHAPTER I

Introduction

Over the past several decades, a tremendous amount of research has gone into exploring specific properties of materials that are not characteristic of their bulk states. These properties are achieved through nanostructured materials that exhibit special properties as a result of their interface-dominated structures. For example, arrays of nanoscale islands made of semiconductor materials leads to confinement of charge carriers [1]. This confinement, known as the quantum confinement, causes the material to exhibit properties that are characteristic of a discrete molecule and results in size-tunable electronic and optical properties [2, 3, 4]. As a consequence, these properties are exploited in optoelectronic applications such as light-emitting diodes (LED), lasers, and photovoltaic devices. Another example is a nanostructure composed of alternating layers of ferromagnetic and nonmagnetic materials [5, 6]. This structure exhibits electrical resistance that depends on the magnetic states of adjacent ferromagnetic layers, which in turn can be controlled by applying an external magnetic field. This effect, known as giant magnetoresistance, leads to spintronic applications such as magnetic sensors and magnetic memory devices such as hard drives [7].

Nanomaterials can be fabricated in "top-down" and "bottom-up" manners. The top-down techniques involve material removal such as cutting, milling and etching.

Examples of these techniques are a collective range of methods called lithography [8], which is a process of fabricating a pattern on a polymer film, or a resist, by different radiation sources such as photons (photolithography) [9], X-rays (X-ray lithography) [10], electrons (electron beam lithography) [11], or ions (focused ion beam lithography) [12]. The resist is then used to selectively etch the pattern onto the underlying film or substrate by masking the underlying area. Other examples include scanning probe techniques where atoms or molecules are manipulated using devices such as the scanning tunneling microscope (STM) [13] or the atomic force microscope (AFM) [14]. These techniques involve lifting or dragging atoms or molecules using either mechanical or electrical force from the probe tips.

The top-down techniques play an important role in nanostructure fabrication; an important example is the photolithography which is used for mass production of integrated circuits [15, 9]. However, these methods produce structural and chemical imperfections such as surface defects and impurities, which in turn affect physical properties of the nanostructures [9]. Furthermore, to produce high-resolution nanostructures (with features of tens of nanometers), the top-down approach becomes increasingly costly due to the need for more sophisticated instruments and a higher level of serialism; for example, the scanning probe techniques involve manipulating atoms one by one [9].

In contrast, the bottom-up techniques are based on building the nanostructure from building blocks (e.g., atoms, molecules, and colloids). They often take advantage of spontaneous formation of structures from atoms or molecules, the so-called self-assembly and self-organization, during growth and annealing processes. An example of these techniques is a vapor-liquid-solid (VLS) growth of nanowires, which is a method where vapor of a growth species is absorbed into a catalytic liquid droplet and precipitated at the growth surface (liquid/solid interface) [16]. Other examples are molecular beam epitaxy (MBE) and chemical vapor deposition (CVD); MBE is

a technique where a beam of atoms or molecules from a heated source interacts with a substrate material to form an epitaxial film under an ultra-high-vacuum condition, and CVD involves reaction among volatile materials, or precursors, during deposition on a substrate. Sputtering, electrochemical deposition and sol-gel processing are also among the bottom-up techniques to produce thin films and nanostructures [9, 17].

The bottom-up techniques are promising for fabrication of nanoscale features with structural homogeneity and a higher level of parallelism [18]. The challenge for the bottom up techniques is, however, the fact that the nanoscale features are not controlled by direct instrumentation, but instead controlled indirectly through complex interplay between thermodynamic and kinetic processes. Therefore, physical understanding of the underlying processes is crucial for the fabrication of nanostructures with desirable features such as those with uniform shape, size and chemical composition.

One of the widely investigated processes for nanostructure formation is epitaxy—the process in which a monocrystalline solid, or a single crystal, forms on a single crystal substrate, typically by bottom-up techniques such as MBE and CVD. The epitaxial process can be further divided into homoepitaxy and hetereoepitaxy. Homoepitaxy is a process in which a growth species and a substrate are the same material whereas heteroepitaxy is a process in which a material are grown on a different substrate material. In heteroepitaxy, a film grown on a substrate is typically strained because of the difference between the lattice spacings of the film and the substrate. This lattice mismatch results in the development of the strain energy in the system, which in turn plays an important role in the morphological evolution of the film.

In heteroepitaxial growth, three growth modes are observed; these growth modes can be characterized by the resulting film morphologies. They are:

- The Volmer-Weber (VW) mode [19]. This mode results in island formation on a substrate without a wetting layer. An example of this mode is growth of Co

on Cu(111) [20].

- The Frank-van der Merwe (FM) mode [21, 22, 23]. This mode results in layer-by-layer formation of a flat film. An example of this mode is growth of Fe on Cu(111) by pulsed laser deposition [24].

- The Stranski-Krastanov (SK) mode [25]. This mode results in island formation on a wetting film layer. The initial growth stage proceeds in a layer-by-layer fashion (as in the FM mode), followed by island formation (as in the VW mode). The change in the growth behavior is attributed to the strain energy from the lattice mismatch between the film and the substrate. An example of the SK mode is growth of Fe on Mo(110) and W(110) [26, 27].

A thermodynamic criterion for determining the growth mode is to consider the chemical potential, μ, (or equilibrium vapor pressure) as a function of film thickness, n: $\partial u/\partial n < 0$ for the VM mode; $\partial u/\partial n > 0$ for the FM mode; and $\partial u/\partial n > 0$ followed by $\partial u/\partial n < 0$ for the SK mode [28].

For SK growth, different transition mechanisms of a film material from a two-dimensional (2D) layer to three-dimensional (3D) islands have been identified. For example, many researchers [29, 30, 31] have proposed a nucleationless process through gradual evolution of surface roughness driven by a strain-relaxation mechanism, known as the Asaro-Tiller-Grinfeld (ATG) instability [32, 33]. Another proposed mechanism is sequential nucleation of islands and pits, known as cooperative nucleation, which is proposed to explain a locally rippling morphology of $Si_{0.5}Ge_{0.5}$ grown on Si(001) [34].

While the proposed mechanisms listed above could be applied to semiconductor systems such as SiGe/Si or InGaAs/GaAs, they are not directly applicable to other technologically important heteroepitaxial system such as magnetic thin films on metal substrates. The reason is that for a SiGe alloy film on a Si substrate, it is energetically favorable for the film lattice to be coherent with that of the substrate (for relatively

small island sizes) due to the strength of the covalent bonds and a relatively lower lattice mismatch. However, in some other systems, higher lattice mismatch results in early formation of interfacial dislocation networks, which contributes to a higher interfacial energy that serves as a thermodynamic driving force for a morphological evolution [35]. For example, it has been shown that continuous Fe films that are grown on Mo(110) at room temperature break up into nanostripes when annealed at elevated temperatures [26, 36]. In addition, Ag and Cu films grown on Ru(0001) form nanowedge islands on thin wetting layers when annealed [37]. For these systems, due to the presence of misfit dislocations, the evolution pathways from 2D to 3D morphologies are different from those occurring in systems with coherent interfaces. This is because the films with fully developed dislocation networks are nearly strain-free; for example, a tensile strain measured from an Fe/Mo island is less than 0.1% [26] while the bulk lattice mismatch is ≈10%. Therefore, the elastically driven mechanisms described earlier (such as the ATG instability) cannot explain the observed morphological changes in these systems.

To develop an understanding of nanostructure formation in metallic epitaxial systems, we have developed a simpler continuum-mechanical model of such systems and more detailed atomistic model based on the phase-field crystal approach. In the following three sections, we summarize the contributions we have made.

1.1 The First Contribution: Investigation of a Thermodynamic Driving Force for Dewetting of Magnetic Thin Film with Misfit Dislocations

Our first contribution lies in an investigation of the recently proposed mechanism for a hereteroepitaxial system with misfit dislocations. This mechanism, termed "dewetting," is observed in growth of single-crystal, internal-defect-free Cr films on a

vicinal W(110) substrate [38]. It is characterized by mass transport of the film material across the substrate steps, leading to formation of locally thinner and thicker film regions without nucleation of new layers. This discovery provides a new insight into how dewetting occurs in absence of other conventional pathways such as those mediated by grain boundaries [39, 40] or impurities [41]. Instead, the driving force for this mechanism was proposed to be the thickness-dependent strain that alters the surface energy due to the surface stress, which causes the energy of a flat film to be higher than that of a film with regions of different thicknesses. However, in the formulation of this theoretical model, the film/substrate interface was assumed to have the same properties as the surface, and the effect of the interfacial misfit dislocations on the film energetics was not explicitly considered.

Therefore, we examine the thermodynamic driving force for the dewetting mechanism; we take into account the contributions of the misfit strain, interfacial misfit dislocations, film surface and interface to the stability of a single-crystal, internal-defect-free, flat film. We use an equilibrium dislocation model based on the Peierls-Nabarro (PN) formulation [42, 43], which describes long-range elastic fields by continuum equations and takes into account a plastic deformation energy at the film/substrate interface in terms of a corrugation potential that can be obtained from first-principles calculations. In addition to the misfit dislocation/deformation energetics, we use a first-principles method based on electronic density functional theory to calculate the surface/interfacial energy as a function of film thickness and a surface strain. Specifically, we focus on Fe/Mo(110) and Fe/W(110) systems, which are well characterized through fundamental experimental studies that relate the growth, morphology and properties of magnetic thin films [26, 36, 44, 45, 46, 47]. However, the method presented can be applied to a broader range of metallic thin film material systems that form misfit dislocations. We find that, through the competition between energetics of the misfit dislocations, misfit strain, film surface and interface, there is a significant

driving force for a flat film to form thinner and thicker regions, leading to the dewetting process. This driving force is more than one order of magnitude larger than that originated from the film-thickness dependence of the energy arising from the surface stress obtained in a recent study by McCarty *et al.* [38]. In addition, we find that non-monotonic variations in the thickness-dependent surface/interfacial energy may give rise to a metastable behavior of the film at certain thicknesses.

This work has provided an impetus for developing a more detailed, atomistic, yet long-time-scale simulation approach as described below.

1.2 The Second Contribution: Numerical Techniques to Improve the Phase-Field Crystal Method and Classical Density Functional Theory

Our analysis above gives an insight into a thermodynamic driving force for an early stage of morphological evolution of a flat internal-defect-free thin film. However, at this point, the result should be interpreted only qualitatively due to several simplifying assumptions made in the misfit-dislocation model; these assumptions enable a semi-analytical form of the solution to the model, which is computationally inexpensive. For example, we have assumed that the material is elastically isotropic whereas a single crystal film should be described with elastic anisotropy. We have also assumed that the misfit dislocations form only a rectangular network whereas the experimentally observed misfit-dislocation structures form more complex structures such as a hexagonal structure [46]. Therefore, in order to predict a more quantitative thermodynamic driving force, we need to consider a model that better represents material properties and allows more complex misfit-dislocation structures.

Furthermore, to properly model the SK growth, we need to not only accurately predict the thermodynamic driving force, but also take into account kinetic consid-

erations. The reason is that morphological evolution during SK growth can also be influenced by kinetic processes. For example, in a situation where the deposition rate is high, the kinetics of surface diffusion become an important factor for the morphological evolution of the growth species [48]; it has been shown that different nanostructures can be tailored in the kinetic-dominant regime (low temperature and high deposition rate) [49]. Therefore, we need to consider computational approaches that take into account both thermodynamics and kinetics of the growth processes.

Considering available computational modeling tools, we can loosely categorize them into atomistic models and mesoscale models. For the first class, a premier tool is molecular dynamics (MD), which is a simulation of physical movements of atoms or molecules using classical equations of motion. Given an appropriate interparticle potential, MD can give a very accurate description of a dynamic system, which is very appealing for the fact that no other input such as *a priori* knowledge of all possible transitions for the system is required (as in a kinetic Monte Carlo method [50]). However, a serious drawback of MD is that it requires a time step small enough to resolve atomic vibrations ($\sim 10^{-15}$ s), which limits MD simulations to very short time scales, typically around microseconds [50]). Thus, it is not suitable for simulations of physical processes of interest (such as surface diffusion) which occur over a much longer time scales.[1]

For the class of mesoscale models, one of the well-established models is the phase-field method. The phase-field method can be considered as a temporally and spatially coarse-grained representation of the atomistic approach. Therefore, the inherent time scales bypass atomic vibration time scales, enabling the phase-field method to capture

[1]In this aspect, the kinetic Monte Carlo (KMC) method can be a preferred method because of its longer time scales. The KMC simulations do not follow the system's dynamics through full atomic trajectories within atomic hops, but rather consider the probability of atomic transitions from one position to another and the corresponding rates, allowing simulations of dynamics over a longer time-scale. However, the KMC method requires *a priori* knowledge of all possible transitions and their rates. Missing transitions can preclude some evolutionary pathways and therefore can potentially lead to incorrect predictions of the evolution of the system [50].

material phenomena over the time scales that are physically meaningful. However, the phase-field method lacks descriptions of atomistic phenomena, which limits the predictive capability of the models without additional auxiliary field variables such as those that describe grain orientations [51, 52, 53, 54, 55, 56] and dislocations [57, 58, 59, 60]. Furthermore, when the physical problem involves multiple phenomena, it becomes challenging to incorporate many auxiliary field variables in a thermodynamically self-consistent manner.

Two approaches that address these issues are classical density functional theory (CDFT) [61, 62, 63] and the phase-field crystal (PFC) method [64, 65, 66] (See also a footnote[2]). A common feature of these approaches is the description of the system via a free energy functional of an atomic density field that is minimized not only by a uniform field (representing liquid) but also by a periodic field (representing solid). The periodic field represents atomic arrangements, and thus it allows for an atomic-scale description of materials [64, 65, 67, 68]. The evolution of the density field can be described by dissipative dynamics [64, 69, 70, 71], which bypasses the lattice-vibration time scale and enables consideration of diffusive times scales while retaining atomistic resolution.

Despite the similarities, the origins of these two methods are different. CDFT is derived from statistical mechanics and involves the description of material properties through a correlation function that contains structural information at the atomistic scale. On the other hand, the original form of the PFC method is derived from the

[2]We note two developments to MD that address the time-scale issue: hyper molecular dynamics (HMD) [72, 73] and diffusive molecular dynamics (DMD) [74]. The HMD is based on the transition state theory where a biased potential is added to the true potential in order to enhance the system's escape rate from the potential minima. As a result, the time scales of the simulations are increased. The DMD is based on the variational gaussian (VG) method where the occupation probabilities for each lattice site are introduced to characterize the system. The occupation probabilities are ensemble average fields and evolve on the diffusive time scale. In comparison with CDFT and the PFC method, both HMD and DMD are developed from the crystal theories and, therefore, are appropriate for simulating solid-state processes. On the other hand, CDFT and the PFC method are developed from the liquid theories [75, 76] and are appropriate for simulating high-temperature processes.

Swift-Hohenberg model of pattern formation [77] and is intended to provide phenomenological descriptions of material behavior. Nevertheless, the link between the CDFT and PFC method was established by Elder and co-workers [76], and the PFC method can thus be considered a simplified form of the CDFT of freezing [67], with a computational efficiency afforded by a lower spatial-resolution requirement than that of CDFT.

While the approximation to obtain the PFC method alleviates the high computational cost of CDFT, it affects predictive capabilities of the formulation. Therefore, the goal of the second contribution is to develop numerical techniques that increase the computational efficiency of CDFT as well as improve the accuracy of the PFC method without increasing the numerical stiffness of the evolution equation. In particular, we propose a rational function fit, a ratio of polynomials, to approximate the Fourier-space two-body direct correlation function (DCF) that is typically used in the CDFT of freezing. We henceforth refer to this approach as the rational function fit (RFF) method. Additionally, the RFF method allows a real-space reformulation of the governing equations when the rational function is expressed as a summation of partial fractions, enabling the use of non-uniform/adaptive grids and descriptions of nonperiodic systems.

We use the RFF method to examine the importance of short-wavelength contributions in the two-body DCF that is used in CDFT. Our studies on iron (Fe) show that the short-wavelength contributions influence the thermodynamic properties not only quantitatively, but also qualitatively. For example, the phase stability of the face-centered-cubic (FCC) structure has a strong dependence on the short-wavelength contributions in the DCF, which is typically not accurately accounted for in PFC studies. We also show that, within the framework of the RFF method, it is possible to empirically parameterize the two-body DCF to increase computational efficiency of CDFT while retaining the accuracy of most predictions of the thermodynamic

properties in comparison to those of CDFT with the full two-body DCF. Finally, we demonstrate that the RFF can be used to improve the representation of the two-body DCF in the PFC model.

1.3 The Third Contribution: Calculations of Isothermal Elastic Constants in the Phase-Field Crystal Method

The benefits of the PFC method mentioned in the previous section suggest that the PFC method can potentially be used to predict non-equilibrium behavior of a material system over experimentally relevant time and length scales. However, before the PFC method can provide robust predictions, it must be parameterized with known equilibrium properties of the materials of interest and be verified that the model accurately predicts thermodynamic properties of the system at equilibrium beyond those used in parameterization. Therefore, we now focus on how equilibrium properties should be calculated within the PFC framework.

The equilibrium properties considered in this work are isothermal elastic constants, which were calculated from the PFC approach in Refs. [64, 65, 78]. These elastic constants, which will be referred to as the PFC elastic constants,[3] are calculated from variations in the free energy density (total free energy per actual volume) associated with various types of quasi-static deformation at a constant average number density. However, we have found that this procedure is inconsistent with the definitions from a theory of thermoelasticity of stressed materials [79, 80, 81]. These definitions are thermodynamically derived and are widely adopted. Therefore, we propose an alternative procedure for calculating the elastic constants as defined by the thermoelasticity theory, which will be referred to as the TE elastic constants. The TE elastic constants are instead calculated from variations in the total free energy per undeformed volume associated with quasi-static deformations at a constant num-

ber of particles in the system. To give numerical examples, we use an existing PFC model for iron (Fe) to show that the PFC and TE elastic constants can be significantly different from one another. Therefore, we conclude that the conventional and the proposed procedures are not interchangeable and, more importantly, one should calculate the elastic constants using the proposed procedure in order to make fair comparisons with values from other approaches such as classical density functional theory [82, 83, 84], Monte Carlo [85], MD [86], and *ab initio* density functional theory [87, 88, 89].

Finally, we employ a thermodynamic theory of stressed solids [90, 91, 92] to systematically define the PFC and TE elastic constants in the same framework. This formulation allows us to obtain the relationships between the PFC and TE elastic constants. These relationships not only facilitate conversions between the PFC and TE elastic constants but also provide quantitative measures of the differences between the PFC and TE elastic constants in terms of thermodynamic quantities such as the pressure of the undeformed state.

[3]We use this term because the PFC elastic constants are not identical to standard elastic constants such as the closed-system elastic constants or the open-system elastic constants.

CHAPTER II

Background

2.1 Overview

This chapter contains the background information on the models that provide the mathematical framework for the work in this thesis. In Section 2.2, we consider the continuum mechanical model of the dislocations and misfit dislocations, which are relevant to our work in Chapter III. Specifically, we review Volterra's model of dislocations [93] in Section 2.2.1 and the Peierls and Nabarro (PN) model [42, 43] in Section 2.2.2. We then consider the misfit-dislocation model by van der Merwe [94] and provide a discussion on the film-substrate interaction potentials in Sections 2.2.3 and 2.2.4, respectively. In section 2.3, we review the the development of the phase-field (PFC) model as well as the classical density functional theory (CDFT). This background information is intended for the work in Chapters IV and V.

2.2 Continuum Models of Dislocations and Misfit Dislocations

In this section, we review selected continuum models to describe dislocations and misfit dislocations; these models provide a mathematical framework for our study of misfit dislocations in the next chapter. Here, we describe the models of only edge

dislocations that are needed to represent the interfacial structures of the epitaxial systems presented in Chapter III. We first consider Volterra's model of dislocations [93], which is a model of a straight dislocation in an infinite homogeneous, isotropic medium. This model provides a description of the long-range stress fields outside the dislocation core region. We then consider a model of a dislocation by Peierls and Nabarro (PN) [42, 43]; the PN model addresses the limitation of the Volterra model in describing the dislocation core due to divergence of the stress fields by including a description of a lattice in a crystalline material. This description is achieved through the potential energy as a function of a displacement with a period related to the atomic spacing in the crystal. Furthermore, we consider a misfit-dislocation model by van der Merwe [95, 94]; this model describes the interface between different crystals with different lattice parameters by an array of PN dislocations. This model is developed for an interface between two infinitely thick crystals and an interface between an infinitely thick and a finite crystal. We will review the latter case because the corresponding geometry is appropriate for modeling an epitaxial system. Lastly, we discuss a development of the film-substrate potential used in misfit dislocation models.

2.2.1 The Volterra Model

Let us denote x, y, and z as the Cartesian coordinate system. Considering a cylindrical-shape material in Fig. 2.1, one can construct a dislocation by making a cut along the half plane $x = 0, y > 0$, inserting an extra material slab of thickness b, and welding the material together, which leaves the continuous body in a state of residual stress. The straight edge dislocation generates a plane strain condition of $u_z = 0$ and $\partial u_i/\partial z = 0$, where u_i is an i-component of a displacement vector and i denotes x, y, and z. As a result, the Airy stress function, χ, which applies to a

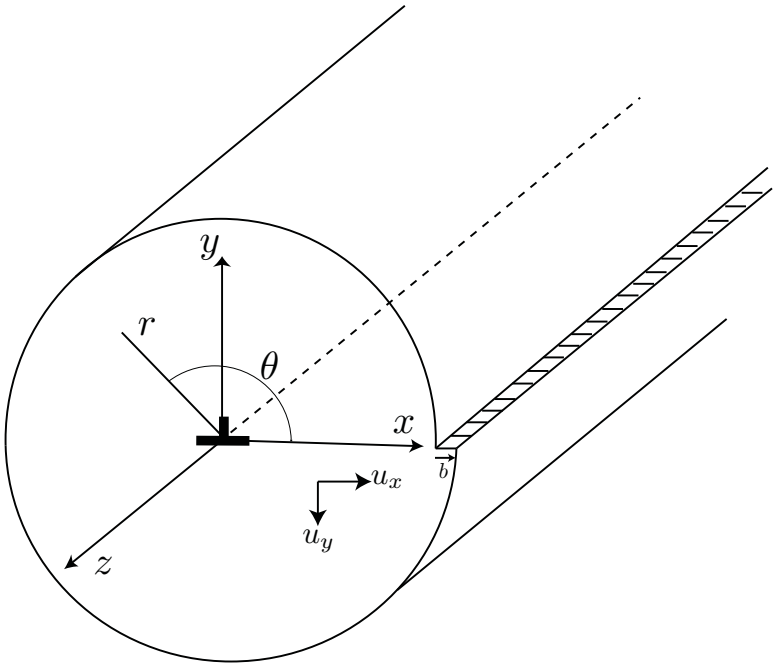

Figure 2.1: A single edge dislocation in a cylinder. This figure has been reproduced from Ref. [96].

two-dimensional system, can be used to represent the stress state of the body [96]:

$$\sigma_{xx} = \frac{\partial^2 \chi}{\partial y^2}, \quad \sigma_{yy} = \frac{\partial^2 \chi}{\partial x^2}, \quad \sigma_{xy} = -\frac{\partial^2 \chi}{\partial x \partial y}, \tag{2.1}$$

where σ_{ij} denote an element of a stress tensor and j also denotes x, y, and z. The equilibrium and the compatibility conditions require the Airy stress function to satisfy

$$\nabla^4 \psi = \left(\frac{\partial^2}{\partial r^2} + \frac{1}{r}\frac{\partial}{\partial r} + \frac{1}{r^2}\frac{\partial^2}{\partial \theta^2} \right)^2 \psi = 0, \tag{2.2}$$

where r and θ denote the polar coordinate system and can be obtained from the relationships $x = r\cos(\theta)$ and $y = r\sin(\theta)$. One can then define a function

$$\Phi \equiv \nabla^2 \chi = \sigma_{xx} + \sigma_{yy} \tag{2.3}$$

and express Eq. (2.2) as

$$\nabla^2\Phi = \left(\frac{\partial^2}{\partial r^2} + \frac{1}{r}\frac{\partial}{\partial r} + \frac{1}{r^2}\frac{\partial^2}{\partial \theta^2}\right)\Phi = 0. \tag{2.4}$$

Applying a separation of variables to the function Φ, one obtains

$$\Phi = \sum_n R_n(r)\Phi_n(\theta). \tag{2.5}$$

The general form of Φ can be found using the Michell's solution [97]. Omitting the terms that yield multi-valued solutions, the solution can be written as

$$\Phi = (\alpha_0 + \beta_0 \ln r) + \sum_{n=1}^{\infty}\left[(\alpha_n r^n + \beta_n r^{-n})\sin n\theta + (\gamma_n r^n + \delta_n r^{-n})\cos n\theta\right], \tag{2.6}$$

where α_n, β_n, γ_n, and δ_n are constants. In the case of dislocation modeling, the fact that the stress $\Phi = \sigma_{xx} + \sigma_{yy}$ should be symmetric with respect to y-axis and that Φ should decrease with increasing r (see Figure 2.1) leads to a very simple expression of Φ:

$$\Phi_{app} = \sum_{n=1}^{\infty}\beta_n r^{-n}\sin n\theta. \tag{2.7}$$

In particular, the lowest-order term can be identified as:

$$\Phi_{Vol} = \beta_1 r^{-1}\sin\theta. \tag{2.8}$$

This term is a characteristic of the long-range stress field of an edge dislocation. It has been noted that the omitted terms $r^n, n \geq 1$ correspond to the external applied surface force [96], which is assumed to be absent, and the term $\ln(r)$ involves a constant shear force on the surface [98]. Finally, the higher order terms $r^{-n}, n \geq 2$ pertain to types of singularities other than the point force of the dislocation. These terms are omitted because they describe particular structures of the core (see Ref.

[96] for a specific example) and are not related to the long-range properties of the dislocation.

With the Volterra approximation discussed above (noted by the subscript *vol*), the Airy stress function for a dislocation can now be determined from

$$\left(\frac{\partial^2}{\partial r^2}+\frac{1}{r}\frac{\partial}{\partial r}+\frac{1}{r^2}\frac{\partial^2}{\partial\theta^2}\right)\Phi_{vol}=\beta_1 r^{-1}\sin\theta. \tag{2.9}$$

The solution is given by

$$\chi_{vol}=\frac{\beta_1}{2}r\sin\theta\ln r. \tag{2.10}$$

Since the dislocation is produced by inserting a half-infinite slab of thickness b, the difference between the integral of elastic strain above and below the slip plane must also be equal to b; that is

$$b=-\int_{-\infty}^{\infty}[\epsilon_{xx}(x,\eta)-\epsilon_{xx}(x,-\eta)]dx,\quad \eta\to 0. \tag{2.11}$$

Using Hooke's law and the derivation of the stress from the Airy stress function, one finds that

$$\beta_1=\frac{-\mu b}{\pi(1-\nu)}, \tag{2.12}$$

where ν and μ are the Poisson's ratio and shear modulus, respectively. Therefore, the stress function becomes

$$\chi_{vol}=-\frac{\mu by}{4\pi(1-\nu)}\ln(x^2+y^2), \tag{2.13}$$

and the elements of the stress tensor can be obtained by using Eq. (2.1) to yield

$$\begin{aligned}
\sigma_{xx} &= -\frac{\mu b}{2\pi(1-\nu)}\frac{y(3x^2+y^2)}{(x^2+y^2)^2} \\
\sigma_{yy} &= \frac{\mu b}{2\pi(1-\nu)}\frac{y(x^2-y^2)}{(x^2+y^2)^2} \\
\sigma_{xy} &= \frac{\mu b}{2\pi(1-\nu)}\frac{x(x^2-y^2)}{(x^2+y^2)^2} \\
\sigma_{zz} &= \nu(\sigma_{xx}+\sigma_{yy}) = -\frac{\mu b\nu}{\pi(1-\nu)}\frac{y}{x^2+y^2} \\
\sigma_{xz} &= \sigma_{yz} = 0 \ . \qquad (2.14)
\end{aligned}$$

The energy per unit length along the z-direction of an edge dislocation can be estimated by integrating the linear-elastic strain energy density. The integration between two coaxial cylinders of radius r_0 and R is

$$\begin{aligned}
\frac{W}{L} &= \int_{r_0}^{R} r dr \int_0^{2\pi} d\theta \left[\frac{1}{2\mu}\sigma_{xy}^2 + \frac{1}{2E}(\sigma_{xx}^2+\sigma_{yy}^2-2\nu\sigma_{xx}\sigma_{yy}-\sigma_{zz}^2)\right] \\
&= \frac{\mu b^2}{4\pi(1-\nu)}\ln\frac{R}{r_0} \ , \qquad (2.15)
\end{aligned}$$

where $r = \sqrt{x^2+y^2}$, E is the Young's modulus, r_0 represents the dislocation core radius within which linear elasticity is invalid, and R is the distance to the outer boundary of the crystal. As will be discussed in the next section, the energy of the dislocation core (within $r < r_0$) must be treated separately by taking into account an effect from an atomic potential. The energy in the above equation represents the energy stored in the deformation caused by the presence of a dislocation, and can be considered as the dislocation energy with the given assumptions outlined above (as well as excluding the chemical energy of the broken bond). The energy of a dislocation diverges when $R = \infty$, meaning that the energy depends on the size of the medium; and $r_0 = 0$ which is attributed to the failure of linear elasticity to describe large lattice distortion near the core of the dislocation. It is generally considered that the

linear theory holds for $r_0 \approx b$.

2.2.2 The Peierls-Nabarro Model

The Peierls-Nabarro (PN) model integrates Volterra's treatment of dislocations with Frenkel's approach [99] of calculating the shear strength of a perfect crystal with a periodic function of a displacement. This results in a dislocation model that reflects the lattice periodicity. Here, we begin with formulating the model, and then obtain the displacement profile as well as the shear stress along the interface. This will be followed by the calculation of the energy of the dislocation.

2.2.2.1 Calculations of Displacement and Stress Fields

The PN model for an edge dislocation in a simple cubic structure is shown in Figure 2.2. In this section, the x-axis is along the Burgers vector of the dislocations, while the y-axis is taken to be normal to the glide plane. The two elastic semi-infinite half planes are separated by a non-Hookean slab of material of width b. An edge dislocation is formed by cutting the perfect crystal along the glide plane ($y = 0$) and displacing the upper half by a distance $b/2$ along x-direction and rejoining the crystal together. The displacement occurs in order to bring atoms into a perfect alignment far away from the dislocation core. In this section, the sign convention is taken such that the stress and displacement bear the sign consistent with the bottom half of the crystal, which is symmetrically related to the top half of the crystal.

The equilibrium configuration is the result of a balance between two forces at the interface. The first is the elastic force that opposes the matching of atoms across the interface $y = 0$. The second force is the interatomic force that tends to bring the atoms across the interface back to a perfect crystal. From Fig. 2.2, the initial disregistry (i.e., the total relative displacement that includes both plastic and elastic deformation) of the top half with respect to the bottom half of the crystal is $b/2$ for

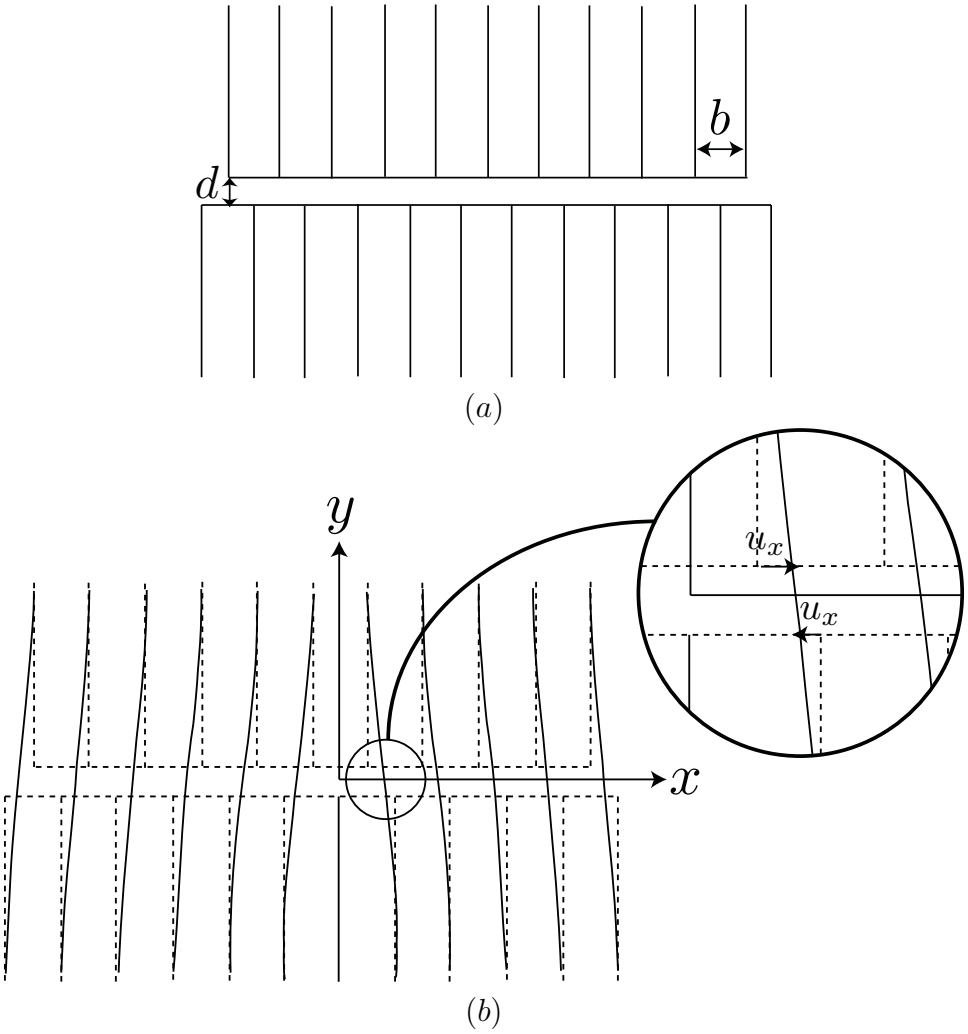

Figure 2.2: (a) Two semi-infinite cubic crystals with disregistry of $b/2$. (b) Distortion of the crystal after an introduction of the dislocation. The figures have been reproduced from Ref. [96].

$x > 0$ and $-b/2$ for $x < 0$. If the x-component of the displacement vectors, $u_x(x)$ and $-u_x(x)$, is imposed on the bottom and top sides of the glide plane, respectively, to form an edge dislocation, the disregistry becomes

$$\phi_x(x) = \begin{cases} 2u_x(x) + b/2, & x > 0 \\ 2u_x(x) - b/2, & x < 0. \end{cases} \tag{2.16}$$

Far away from the dislocation core, the atoms across the interface coincide, yielding the boundary condition:

$$u_x(\infty) = -u_x(-\infty) = -b/4 \ . \tag{2.17}$$

We now consider the top half of the crystal. The elastic response from the displacement is balanced by the restoring force from the bottom half. The atoms at the interface can be viewed as being displaced from the potential troughs originating from the bottom half of the crystal. As a first approximation, it is reasonable to assume that the potential follows a sinusoidal function of the disregistry. The stress caused by the restoring force resulting from this potential, σ^0, which tends to bring the atoms back to coincidence, is then given by the derivative of the potential with respect to the displacement along x-direction:

$$\begin{aligned} \sigma^0 &= A \sin\left(\frac{2\pi\phi_x}{b}\right) \\ &= \sigma_{xy}(x, 0), \end{aligned} \tag{2.18}$$

where $\sigma_{xy}(x, 0)$ is the elastic shear stress at the interface and A is a constant. For small strain, the above expression can be approximated as

$$\sigma^0 = A\left(\frac{2\pi\phi_x}{b}\right) \ . \tag{2.19}$$

The constant A can be determined by requiring that Eq. (2.19) converges to Hooke's law, yielding,

$$\begin{aligned} \sigma^0 &= 2\mu\epsilon_{xy} \\ &= \frac{\mu\phi_x}{d}, \end{aligned} \tag{2.20}$$

where d is the interplanar distance. From Eq. (2.19) and Eq. (2.20), one obtains

$$\begin{aligned} A\left(\frac{2\pi\phi_x}{b}\right) &\approx \frac{\mu\phi_x}{d} \\ A &\approx \frac{\mu b}{2\pi d}. \end{aligned} \tag{2.21}$$

Therefore, using Eq. (2.16) and Eq. (2.21), Eq. (2.18) can be written as

$$\sigma^0 = -\frac{\mu b}{2\pi d}\sin\left(\frac{4\pi u_x}{b}\right). \tag{2.22}$$

From the Volterra dislocation, the relevant stress at the interface, $\sigma_{xy}(x,0)$, due to an edge dislocation in the plane strain condition is (Eq. (2.14))

$$\sigma_{xy}(x,0) = -\frac{\mu}{2\pi(1-\nu)}\frac{b}{x}\ . \tag{2.23}$$

The equilibrium condition requires the stress from Eq. (2.18) and the stress from Eq. (2.23) to be equal. As suggested by Eshelby [100], a distribution of infinitesimal edge dislocations satisfies this condition. At a distance x' away from the dislocation core, $b'(x')dx'$ is defined as the x-component of the Burgers vector of an infinitesimal dislocation situated between x' and $x'+dx'$. The boundary condition of Eq. (2.17), requires that

$$b = \int_{-\infty}^{\infty} b'(x')dx' = -2\int_{-\infty}^{\infty} \frac{du_x}{dx}\Big|_{x=x'} dx'. \tag{2.24}$$

The shear stress at $(x, 0)$ can be expressed as

$$\begin{aligned} \sigma_{xy}(x,0) &= -\frac{\mu}{2\pi(1-\nu)} \int_{-\infty}^{\infty} \frac{b' dx'}{x - x'} \\ &= -\frac{\mu}{2\pi(1-\nu)} \int_{-\infty}^{\infty} \frac{(du_x/dx)|_{x=x'} dx'}{x - x'}. \end{aligned} \tag{2.25}$$

It is noted that the variable x in the denominator of Eq. (2.25) is an independent variable while the variable x in the numerator is evaluated at x'. In addition, the quantity $(x - x')$ denotes the distance from the dislocation core.

At equilibrium, the elastic stress must equal the restoring force stress, leading to an integro-differential equation for the displacement u_x.

$$\int_{-\infty}^{\infty} \frac{(du_x/dx)|_{x=x'} dx'}{x - x'} = \frac{b(1-\nu)}{2d} \sin\left(\frac{4\pi u_x}{b}\right). \tag{2.26}$$

The solution to Eq. (2.26) is given by

$$u_x = -\frac{b}{2\pi} \tan^{-1} \frac{x}{\xi}, \tag{2.27}$$

where $\xi = d/2(1-\nu)$. Therefore from Eq. (2.24), one can obtain the distribution of the Burgers vector component,

$$b'(x') = \frac{b}{\pi} \frac{\xi}{x'^2 + \xi^2}\ . \tag{2.28}$$

One can now obtain the stress function of this distribution from the solution of a

Volterra edge dislocation (Eq. (2.13)):

$$\begin{aligned}\psi &= \frac{\mu}{2\pi(1-\nu)}\int_{-\infty}^{\infty} b' y \ln[(x-x')^2+y^2]^{1/2}dx' \\ &= \frac{\mu b \xi y}{4\pi^2(1-\nu)}\int_{-\infty}^{\infty}\frac{\ln[(x-x')^2+y^2]}{x'^2+\xi^2}. \end{aligned} \tag{2.29}$$

With the evaluation of the integral, Eq. (2.29) becomes

$$\psi = \begin{cases} \frac{\mu b}{4\pi(1-\nu)} y \ln[x^2+(y+\xi)^2], & y>0 \\ \frac{\mu b}{4\pi(1-\nu)} y \ln[x^2+(y-\xi)^2], & y<0. \end{cases} \tag{2.30}$$

The complete stress distribution can be expressed as

$$\begin{aligned}\sigma_{xy} &= \frac{-\mu b}{2\pi(1-\nu)}\left\{\frac{x}{x^2+(y+\xi)^2}-\frac{2xy(y+\xi)}{[x^2+(y+\xi)^2]^2}\right\} \\ \sigma_{xx} &= \frac{\mu b}{2\pi(1-\nu)}\left\{\frac{3y+2\xi}{x^2+(y+\xi)^2}-\frac{2y(y+\xi)^2}{[x^2+(y+\xi)^2]^2}\right\} \\ \sigma_{yy} &= \frac{\mu b}{2\pi(1-\nu)}\left\{\frac{y}{x^2+(y+\xi)^2}-\frac{2x^2y}{[x^2+(y+\xi)^2]^2}\right\} \\ \sigma_{zz} &= \nu(\sigma_{xx}+\sigma_{yy}) = \frac{\mu b \nu}{\pi(1-\nu)}\frac{y+\xi}{x^2+(y+\xi)^2}\ . \end{aligned} \tag{2.31}$$

By comparing Eq. (2.31) with Eq. (2.14), it is clear that the Peierls-Nabarro dislocation converges to the Volterra dislocation when $r=\sqrt{x^2+y^2} \gg \xi$. It is important to note that the parameter ξ regularizes the singularity at the origin $r=0$ appearing in the Volterra dislocation. This parameter originates from the treatment of the underlying crystal lattice in the PN model, and thus the regularization stems from the discrete nature of a crystalline solid at the atomic scale.

2.2.2.2 Calculation of Dislocation Energy

With the expressions of the displacement and stress, the energy associating with the PN dislocation can be calculated. The energy is divided into two parts. The first energetic contribution is the elastic strain energy stored outside the dislocation core, which is related to the strain energy calculated from the Volterra formulation. The second energetic contribution stems from the distortion of bonds across the interface, which is important in calculating the dislocation-core energy.

For the first energy contribution, the elastic strain energy stored in the crystal equals the work done by the surface force to generate the displacement u_x. The work per area δx and per unit length in the z-direction (out of the paper on Fig. 2.2) is

$$\delta W = \int_0^{u_x} \sigma_{xy} \delta x du = \frac{1}{2} \sigma_{xy}(x,0) u_x \delta x. \tag{2.32}$$

By integrating this along x from $-a$ to a, the energy stored in the crystal is

$$W = \frac{\mu b^2}{4\pi(1-\nu)} \ln \frac{a}{2\xi}, \tag{2.33}$$

which is similar to Eq. (2.15). As discussed later, a will be set by the dislocation spacing in the case of a dislocation array.

The second contribution is the dislocation-core energy (energy resulting from lattice deformation) arising from the shear strain on the slip surface, expressed as

$$\epsilon_{xy}(x,0) = -\frac{\phi_x}{2d} = -\frac{2u_x + (b/2)}{2d}. \tag{2.34}$$

The total contribution to the dislocation-core energy is $\sigma^0 d\epsilon_{xy} + \sigma^0 d\epsilon_{yx} = 2\sigma^0 d\epsilon_{xy}$. The dislocation-core energy in a block of height d, width δx and a unit length in the

z-direction is given by:

$$\begin{aligned}
\delta W &= -2\int \delta x \sigma^0 d\epsilon_{xy} = 2\int_{u_x(-\infty)}^{u_x} \delta x \sigma^0 du'_x \\
&= -\frac{\mu b \delta x}{\pi d}\int_{b/4}^{u_x} \sin\frac{4\pi u'_x}{b} du'_x \\
&= \frac{\mu b^2 \delta x}{4\pi^2 d}\left(1+\cos\frac{4\pi u_x}{b}\right). \qquad (2.35)
\end{aligned}$$

The total dislocation-core energy in the glide plane can now be obtained by integrating this along the glide plane:

$$\begin{aligned}
W_{core} &= \frac{\mu b^2 \delta x}{4\pi^2 d}\int_{-\infty}^{\infty}\left(1+\cos\frac{4\pi u_x}{b}\right)dx \\
&= \frac{\mu b^2}{4\pi(1-\nu)}. \qquad (2.36)
\end{aligned}$$

2.2.3 Van der Merwe Models

We now consider an interface between an epitaxial film and a substrate with different lattice spacings (often referred to as lattice mismatch or lattice misfit). This misfit causes the system to respond in order to accommodate the misfit strain. If the total misfit strain is accommodated by the homogeneous strain, the lattices of the film and the substrate are deformed to match, resulting in a coherent interface. On the other hand, the lattices can shear in a manner that introduces dislocations between the film and the substrate (or in some cases in an atomic layer near the interface). At some distances away from this local distortion, the lattices perfectly match. Such dislocations induced by the lattice mismatch are referred to as misfit dislocations. It is also possible for the misfit strain to be accommodated by both the interfacial dislocations and homogeneous strain simultaneously.

The mathematical descriptions of misfit dislocations was pioneered by van der

Merwe, who modeled an array of dislocations using both discrete [101] and continuum approaches [95, 94, 102]. For the discrete approach, van der Merwe [103] modeled an epitaxy using a chain of balls connected through springs subjected to the sinusoidal potential. The energy calculation shows that there are cases when the chain of atoms preferred to match the substrate, and other cases when the chain of atoms remained mismatched. For the latter circumstance, the preferred configuration consists of a periodic arrangement of regions with near lattice match separated by regions with large lattice mismatch; the latter regions can be considered as the localized core regions of the misfit dislocations.

Subsequently, van der Merwe proposed continuum models of misfit dislocations based on the PN model introduced in the previous subsection. For a case of an interface between two infinitely thick crystals, van der Merwe obtained the exact analytical solutions for the interfacial energy of the misfit dislocations between both elastically similar [102] and elastically dissimilar materials [95]. Both results show that the strain energy due to the misfit dislocation is localized, which is consistent with the result from the discrete model. In addition, both works showed that the infinite film can be a good estimation for cases when the thickness of the film is larger than half the dislocation spacing.

The model that will be described below is an extension to the continuum model described above. This model describes an interface between an infinitely thick substrate and a finite-thickness film [94]. For simplicity, van der Merwe employed a parabolic potential instead of a sinusoidal potential as in the PN model and his earlier models [101, 95, 94]. The parabolic potential allows the stress fields and dislocation energy to be expressed analytically. In the next chapter, we will extend this model by using a sinusoidal potential, which is a more accurate representation of a film-substrate interaction in a material system.

2.2.3.1 Calculations of Displacement and Stress Fields

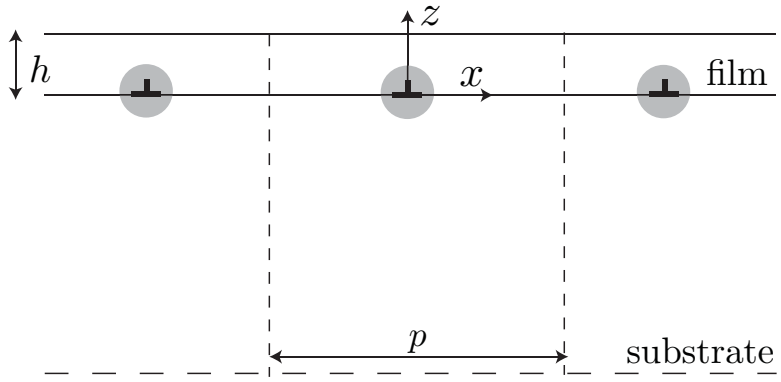

Figure 2.3: Misfit dislocation at an interface between an infinitely-thick substrate and a finite-thickness film

Let us consider a system of two crystals separated by an interface, as shown in Fig. 2.3. The finite crystal will be referred to as a film and the infinite-thick crystal will be the substrate. For simplicity, the lattice parameters of the film and the substrate are assumed to be different only along the x-direction. The misfit dislocations can be represented by an array of PN edge dislocations along the x-direction with the spacing

$$p = Pa^s = (P+1)a^f = \left(P + \frac{1}{2}\right) c \tag{2.37}$$

where p is the dislocation spacing, c is the reference lattice spacing, P is an integer, a^f and a^s are the lattice parameters of the film and substrate, respectively. This plain-strain problem can be described by the Airy stress functions, χ^a, which are related to elements of the stress tensor by

$$\sigma^a_{xx} = \frac{\partial^2 \chi^a}{\partial z^2}, \quad \sigma^a_{zz} = \frac{\partial^2 \chi^a}{\partial x^2}, \quad \sigma^a_{zx} = -\frac{\partial^2 \chi^a}{\partial z \partial x}. \tag{2.38}$$

We use the superscript a to denote the quantities in the film ($a = f$) and the substrate ($a = s$) regions. Due to the assumed periodic arrangement of the dislocations, the stress is sinusoidal in x-direction over a period, p. The appropriate general expression

can be written as [94]

$$\begin{aligned}
\chi^s &= \sum_{n=1}^{\infty}(F_n + G_n z)e^{mz}\cos(mx) \\
\chi^f &= \sum_{n=1}^{\infty}\left[(A_n + C_n z)\cosh(mz) + (B_n + D_n z)\sinh(mz)\right]\cos(mx), \quad (2.39)
\end{aligned}$$

where $m = 2\pi n/p$ and the superscripts f and s denote the quantities of the film and the substrate, respectively. The constants $A_n, B_n, C_n, D_n, F_n,$ and G_n are Fourier coefficients which need to be determined. According to Eq. (2.38) and the plain-strain condition, the stresses in the film ($z > 0$) are given by

$$\begin{aligned}
\sigma^f_{xx} &= \sum_{n=1}^{\infty}\left[2\,C_n m + (B_n + D_n z)\,m^2\right]\sinh(mz)\cos(mx) \\
&\quad + \sum_{n=1}^{\infty}\left[(A_n + C_n z)\,m^2 + 2\,D_n m\right]\cosh(mz)\cos(mx) \\
\sigma^f_{zz} &= -\sum_{n=1}^{\infty}\left\{(B_n + D_n z)\sinh(mz) + (A_n + C_n z)\cosh(mz)\right\}m^2\cos(mx) \\
\sigma^f_{zx} &= \sum_{n=1}^{\infty}\left[(A_n + C_n z)\,m + D_n\right]m\sin(mx)\sinh(mz) \\
&\quad + \sum_{n=1}^{\infty}\left[C_n + (B_n + D_n z)\,m\right]m\sin(mx)\cosh(mz) \\
\sigma^f_{yy} &= \nu^f(\sigma^f_{xx} + \sigma^f_{zx}) \\
\sigma^f_{yx} &= \sigma^f_{yz} = 0, \quad (2.40)
\end{aligned}$$

where ν^f is the Poisson's ratio of the film material. The stresses in the substrate

$(z < 0)$ are

$$\begin{aligned}
\sigma^s_{xx} &= \sum_{n=1}^{\infty} \left(2\, G_n m + (F_n + G_n z)\, m^2\right) e^{mz} \cos(mx) \\
\sigma^s_{zz} &= -\sum_{n=1}^{\infty} (F_n + G_n z)\, m^2 e^{mz} \cos(mx) \\
\sigma^s_{zx} &= \sum_{n=1}^{\infty} \left(G_n m + (F_n + G_n z)\, m^2\right) e^{mz} \sin(mx) \\
\sigma^s_{yy} &= \nu^s(\sigma^s_{xx} + \sigma^s_{zx}) \\
\sigma^s_{yx} &= \sigma^s_{yz} = 0, \qquad (2.41)
\end{aligned}$$

where ν^f is the Poisson's ratio of the substrate material. The boundary conditions for the stresses are as follows:

$$\sigma^s_{xx} = \sigma^s_{zz} = \sigma^s_{zx} = 0 \qquad \text{at } z = -\infty \qquad (2.42)$$

$$\sigma^f_{zx} = \sigma^s_{zx} = 0 \qquad \text{at } x = 0, \pm p/2 \qquad (2.43)$$

$$\sigma^f_{zz} = \sigma^f_{zx} = 0 \qquad \text{at } z = h \qquad (2.44)$$

$$\sigma^f_{zx} = \sigma^s_{zx} \qquad \text{at } z = 0 \qquad (2.45)$$

$$\sigma^f_{zz} = \sigma^s_{zz} \qquad \text{at } z = 0. \qquad (2.46)$$

The first condition originates from the assumption that the substrate is infinitely thick; this is a reasonable assumption in the epitaxial thin film. The second condition implies that the shear stress is zero at the dislocations and halfway between them. The third condition states that the film surface is stress free. The remaining boundary conditions ensure the continuity of the normal and shear stresses across the interface.

The first two conditions are automatically satisfied by the functional forms of the

Airy stress functions and the remaining boundary conditions give the relations:

$$\begin{aligned} A_n &= F_n \\ C_n + mB_n &= G_n + mF_n \\ (B_n m + C_n + D_n mh)\cosh(mh) &= -(C_n mh + D_n + mA_n)\sinh(mh) \\ (A_n + C_n h)\, m\cosh(mh) &= -(B_n + D_n h)\, m\sinh(mh)\,. \end{aligned} \tag{2.47}$$

The remaining two expressions that will be used to solve for the Fourier coefficients will be obtained from the conditions that the forces (or stresses) from the elastic body is balanced with the forces (or stresses) arising from the atomic potential energies that account for the discrete nature of a crystal lattice; these conditions are analogous to Eq. 2.22 from the PN model and will be referred to as the PN conditions. The potential energies considered in this model are parabolic functions of the relative tangential displacement, U_x, and the relative normal displacement, W_x defined as [94]

$$\begin{aligned} U_x &= \frac{cx}{p} + u^f(x,0) - u^s(x,0), \\ W_x &= w^f(x,0) - w^s(x,0), \end{aligned} \tag{2.48}$$

where $u^a(x,0)$ and $w^a(x,0)$ are tangential and normal displacements at the interface, respectively, and the term cx/p refers to the relative displacement of the corresponding atoms across the interface without the elastic deformation. The PN conditions then give [94]

$$\sigma^a_{zz}(x,0) = \frac{2V_n}{d_z} W_x, \tag{2.49}$$

and

$$\sigma^a_{zx}(x,0) \;=\; \frac{V_t}{c}U_x, \tag{2.50}$$

where d_z is the interplanar spacing along the z-direction and V_n as well as V_t are related to the bond strength. The left-hand sides in Eqs. (2.49) and (2.50) are the stresses from the elastic body and the right-hand sides are the stresses from the atomic potentials (obtained from taking the first derivative of the potentials with respect to U_x or W_x). In Chapter III, we will use a sinusoidal potential, which yields sinusoidal shear stress as a function of U_x, instead of the parabolic form, which yield a linear functional form of the stress as in Eq. (2.50).

Next, one needs to obtain the expressions of $u^a(x,0)$ and $w^a(x,0)$ in terms of the Fourier coefficients. The plain-strain condition relates the stress to the elastic strain by the following expressions:

$$\begin{aligned}
e^a_{xx} &= \frac{1}{2\mu^a}\left[(1-\nu_a)\sigma^a_{xx} - \nu^a\sigma^a_{zz}\right] \\
e^a_{zz} &= \frac{1}{2\mu^a}\left[(1-\nu_a)\sigma^a_{zz} - \nu^a\sigma^a_{xx}\right] \\
e^a_{zx} &= \frac{\sigma^a_{zx}}{2\mu^a} \\
e^a_{yy} &= 0 = e^a_{yz} = e^a_{yx},
\end{aligned} \tag{2.51}$$

The elastic strain can be written in terms of u^a and w^a as follows:

$$\begin{aligned}
e^a_{xx} &= \frac{\partial u^a}{\partial x} \\
e^a_{zz} &= \frac{\partial w^a}{\partial z} \\
e^a_{zx} &= \frac{1}{2}\left(\frac{\partial u^a}{\partial z} + \frac{\partial w^a}{\partial x}\right),
\end{aligned} \tag{2.52}$$

The expression for the tangential and normal displacement at the interface $z = 0$ can

be obtained:

$$\begin{aligned} u^f(x,0) &= \sum_{n=1}^{\infty}\left(\frac{mA_n}{2\mu^f}+\frac{D_n}{\omega^f}\right)\sin(mx) \\ u^s(x,0) &= \sum_{n=1}^{\infty}\left(\frac{mF_n}{2\mu^s}+\frac{G_n}{\omega^s}\right)\sin(mx) \\ w^f(x,0) &= -\sum_{n=1}^{\infty}\left(\frac{mB_n}{2\mu^f}-\frac{C_n}{2\psi^f}\right)\cos(mx) \\ w^s(x,0) &= -\sum_{n=1}^{\infty}\left(\frac{mF_n}{2\mu^s}-\frac{G_n}{2\psi^s}\right)\cos(mx), \end{aligned} \tag{2.53}$$

where $\omega^a = \mu^a/(1-\nu^a)$, and $\psi^a = \mu^a/(1-2\nu^a)$. Using the above equations and Eqs. (2.49) and (2.50), one obtain the last two expressions that will be used to solve for the Fourier coefficients:

$$\frac{m^2 dA_n}{V_n} - \frac{mB_n}{\mu^f} + \frac{C_n}{\psi^f} + \frac{mF_n}{\mu^s} - \frac{G_n}{\psi^s} = 0, \tag{2.54}$$

and

$$m\left(\frac{mc}{V_t}-\frac{1}{\mu^f}\right)A_n + \frac{mc}{V_t}C_n - \frac{1}{\omega^f}D_n + \frac{m}{\mu^s}F_n + \frac{1}{\omega^s}G_n = -\frac{2c}{mp}(-1)^n \tag{2.55}$$

Equations (2.47), (2.54) and (2.55) provide a system of equations required to determine the Fourier coefficients, $A_n, B_n, C_n, D_n, F_n,$ and G_n. With all the coefficients determined, one can now evaluate the energetic contributions of the misfit dislocations to the total energy of heteroepitaxial thin films.

2.2.3.2 Calculation of Misfit Dislocation Energy

The nonzero contributions to the energy per unit area associating with the formation of the misfit dislocations are the long-range elastic energy, E^e, which can be

calculated from

$$E^e = -\frac{1}{2p}\int_{-p/2}^{p/2} \sigma_{zx}^a(x,0)\left(u^f(x,0)-u^s(x,0)\right)dx \tag{2.56}$$

and the plastic deformation energy, which can be obtained by

$$E^p = \frac{1}{p}\int_{-p/2}^{p/2}\int_{0}^{U_x} \sigma_{zx}^a(x,0)dU_x dx. \tag{2.57}$$

Using the expression of $\sigma_{zx}^a(x,0)$ from Eq. (2.40) and the relationships in Eqs. (2.48) and (2.50), we can express the total energy as

$$E^e + E^p = \frac{c}{2p}\sum_{n=1}^{\infty}\left(mB_n + C_n\right). \tag{2.58}$$

When the energy of the homogeneous strain was incorporated into the analysis, van der Merwe found that there was a critical misfit strain above which the misfit dislocations are spontaneously created and below which the film remains coherent with the substrate. The magnitude of the critical misfit depends on the film thickness, the ratio of the shear moduli of two materials, and the bond strength; the critical misfit is large when the film is relatively soft and the bonding is relatively strong.

2.2.4 Film-Substrate Potential

Following the Peierls-Nabarro and Frenkel-Kontorova models [104], van der Merwe first employed the following energy potential in the misfit-dislocation model to represent the film-substrate interaction across the interface [102]:

$$V = \frac{1}{2}V_0\left[1-\cos\left(\frac{2\pi U}{c}\right)\right], \tag{2.59}$$

where V_0 is the bonding strength across the interface, U is the disregistry of corresponding atoms across the interface and, c is the period of the misfit dislocation. The expression from Eq. (2.59) can be viewed as a Fourier series truncated at the first harmonic term. For a two-dimensional system, the interaction across the interface becomes [103]:

$$V = \frac{1}{2}V_x\left[1-\cos\left(\frac{2\pi U_x}{c}\right)\right]+\frac{1}{2}V_y\left[1-\cos\left(\frac{2\pi U_y}{c}\right)\right], \tag{2.60}$$

where the subscripts x and y denote the directions along the two axes.

Further attempts to refine the film-substrate interactions include the parametric modification of the force law by Foreman [105], which yields a different parameterization of the sinusoidal interaction potential. The modified potential allows the dislocation width to be adjusted so that the resulting stresses and strains agree with the experimental observations made on macroscopic systems (bubble rafts). In addition, Ball [106] and Foreman [107] included the second harmonic term of the Fourier series in order to flatten the steep maximum of the sinusoidal approximation and properly reflect the dissociation of dislocations in a cubic crystal.

As opposed to the empirical expressions of the sinusoidal potential, a more physical description of the potential can be obtain from the generalized stacking fault energy (GSFE) or the γ surface [108]. The GSFE is obtained by displacing one half of the crystal along the glide plane with respect to the other by a vector in the glide plane. The crystal is then rejoined and allowed to relax. The GSFE is given by the difference between the energy of the displaced crystal and that of the perfect crystal [109]. The earlier calculations of GSFE employ simplified interactomic interactions that take into account a few atomic neighbors [108]. Today, due to the advances in quantum mechanical calculations and computational power, the GSFEs are often calculated using *ab initio* atomistic simulations (e.g., Refs. [110], [111]) to provide

realistic film-substrate interaction potentials.

The work in Chapter III utilizes the GSFE of the Fe/Mo and Fe/W systems from the *ab initio* simulations. This GSFE will serve as an input to the misfit dislocation model in order to provide a more quantitative description of the misfit dislocations.

2.3 Overview of the Phase-Field Crystal Model

In this section, we review the development of the phase-field crystal (PFC) model; in the process, classical density functional theory (CDFT) will also be reviewed. Specifically, we consider two derivations of what is considered the "original" PFC equations [64, 76]. Hereafter, we refer to the two approaches as *Phenomenological Development* (as an extension of pattern-formation modeling) and *Theoretical Development* (based on the CDFT). In the phenomenological development, the PFC method is formulated from the concepts of the Ginzburg-Landau model [112], phase-field model [113], and the Swift-Hohenberg [77] equation, all of which are phenomenological approaches. In particular, the Swift-Hohenberg equation was originally developed to describe pattern formation arising from convective instability. In the theoretical development, the PFC method is considered an approximation of the CDFT [62], which is a reformulation of statistical mechanics. While both of them can be described as theory, we here distinguish them by how they are derived – the former was suggested based on the behavior of the solutions to the Swift-Hohenberg equation, while the latter begins with statistical mechanics, which leads to an identical equation after a number of approximations.

2.3.1 Phenomenological Development

The phenomenological development of the PFC model can be traced back to the Ginzburg-Landau formulation for order-disorder phase transformations [112]. The starting point of the formulation is the introduction of a field variable, referred to

as an order parameter, $\phi(\mathbf{r})$, to describe physically relevant field quantities such as crystalline order, concentration, or magnetization; the vector $\mathbf{r}$ denotes a position vector. The order parameter is typically a ratio or scaled quantity that defines the thermodynamic state of the system. For example, when the order parameter takes a value of zero, the system can be defined as being in a disordered state such as liquid or paramagnetic state. When the order parameter takes a finite value, the system can be considered as being in an ordered state such as solid or ferromagnetic state. Along with the order parameter to characterize the state, one also needs to formulate a free energy expression that governs the thermodynamics of the system. The simplest form of the free energy expression can be written in terms of (i) a bulk contribution that reflects thermodynamics of an infinite and uniform system and (ii) a gradient contribution that describes the energy associated with interfaces between different phases. Such free energy functionals can be written in the following form:

$$\mathcal{F}\big(\phi(\mathbf{r})\big) = \int f\big(\phi(\mathbf{r})\big) dV. \tag{2.61}$$

The functional, $f\big(\phi(\mathbf{r})\big)$, is a free energy density and is typically of the form

$$f\big(\phi(\mathbf{r})\big) = w\big(\phi(\mathbf{r})\big) + K|\nabla\phi(\mathbf{r})|^2, \tag{2.62}$$

where K is a positive constant related to interfacial energy. The function $w\big(\phi(\mathbf{r})\big)$, referred to as the Landau free energy, gives a bulk contribution and is written as a polynomial of the order parameter with temperature-dependent coefficients.

The free energy of the form given in Eqs. (2.61) and (2.62) provides the foundation for the phase-field model [113], which, as the name implies, is a conceptual predecessor of the PFC method. The free energy of the phase-field model can be obtained by (i) approximating $w\big(\phi(\mathbf{r})\big)$ with a double-well potential, i.e., only retaining even-order polynomial terms, and (ii) considering $\phi(\mathbf{r})$ as a concentration field. In the phase-

field model, the equilibrium profile of $\phi(\mathbf{r})$ is uniform in the bulk region and has a smoothly varying behavior at the interfaces. From this behavior, homogeneous regions, such as areas inside bulk regions or crystal grains, are described by a uniform order-parameter value. On the other hand, inhomogeneous regions, such as interfaces or grain boundaries, are described by a spatially varying order-parameter value.

Instead of formulating a free energy of which the equilibrium state of a bulk system is described by a uniform order parameter, one may desire to construct a free energy functional of which the equilibrium state is characterized by a non-uniform order parameter. The non-uniform behavior of the order parameter that is convenient in the context of phase transformation is one that is spatially periodic because one can consider an ordered phase as a periodic arrangement of its constituents. For example, we may consider a bulk solid as a collection of periodically arranged atoms, instead of a region that has a uniform concentration of species. In fact, a free energy functional of which the equilibrium state is characterized by a periodic field variable has been used in other areas of study such as order-disorder transformation of alloy phases [114, 115] and pattern formation [116]. However, it was not until the work by Elder et al. [64, 65] that the free energy developed for pattern formation was employed to describe atomic arrangements. They proposed the free energy density of the form

$$f\big(\phi(\mathbf{r})\big) = w\big(\phi(\mathbf{r})\big) + \frac{\phi(\mathbf{r})}{2} G\left(\nabla^2\right) \phi(\mathbf{r}), \tag{2.63}$$

where the operator $G\left(\nabla^2\right)$ is designed so that the gradient of the order parameter is favored, while a penalty is imposed on the magnitude of the Laplacian of the order parameter. This choice of $G\left(\nabla^2\right)$ is identical to that of the Swift-Hohenberg (SH) model for convective instabilities [77]:

$$G\left(\nabla^2\right) = \lambda(q_0^2 + \nabla^2)^2, \tag{2.64}$$

where λ is a fitting parameter and q_0 is a constant that sets the periodicity of the order-parameter variation. Along with the fourth-order polynomial form of $w\big(\phi(\mathbf{r})\big)$, the PFC free energy was proposed to be

$$\mathcal{F}_s(\phi(\mathbf{r})) = \int f_s\big(\phi(\mathbf{r})\big)d\mathbf{r} = \int d\mathbf{r}\left[g\frac{\phi(\mathbf{r})^4}{4} + \alpha\frac{\phi(\mathbf{r})^2}{2} + \frac{\phi(\mathbf{r})}{2}\lambda(q_0^2+\nabla^2)^2\phi(\mathbf{r})\right], \quad (2.65)$$

where g and α are analogous to the coefficients in the Landau free energy. The coefficient α is set to be proportional to a degree of undercooling, or $\alpha = a_s\Delta T$, where ΔT is the temperature difference from the melting point. We denote the form of Eq. (2.65) as the SH-PFC form and denote the corresponding free energy, $\mathcal{F}_s$, and free energy density, f_s, with the subscript s. The variable $\phi(\mathbf{r})$ is considered as an atomic number density in this formulation. Depending on the values of the fitting parameters, the free energy yields two classes of equilibrium profiles of $\phi(\mathbf{r})$. One is a uniform profile representing a liquid state, and the other is a periodically non-uniform profile representing a crystalline state, which may have multiple patterns corresponding to different atomic structures. The periodicity of $\phi(\mathbf{r})$ in the crystalline state gives rise to (i) anisotropic elasticity and interfacial energies that correspond to the symmetry of the crystal and (ii) defects in patterns that are representative of crystal defects such as dislocations and grain boundaries. These features are not present in the phase-field free energy without augmenting the free energy with auxiliary field variables.

The equation that governs the evolution of $\phi(\mathbf{r})$ is formulated by assuming dissipative dynamics with mass conservation [64, 65]:

$$\frac{\partial\phi(\mathbf{r})}{\partial t} = \Gamma\nabla^2\frac{\delta\mathcal{F}_s\big(\phi(\mathbf{r})\big)}{\delta\phi(\mathbf{r})} + \eta = \Gamma\nabla^2\mu + \eta, \quad (2.66)$$

where μ is the chemical potential and η is the stochastic thermal fluctuations. Equa-

tions (2.65) and (2.66) can be nondimensionalized [65, 78]:

$$\tilde{\mathcal{F}}_s = \frac{g}{\lambda^2 q_0^{8-d}} \mathcal{F}_s = \int \tilde{f}_s d\tilde{\mathbf{r}}, \tag{2.67}$$

where

$$\tilde{f}_s = \frac{g}{\lambda^2 q_0^8} f_s = \frac{\tilde{\phi}(\tilde{\mathbf{r}})}{2} \left[-\tilde{\epsilon} + \left(\tilde{\nabla}^2 + 1 \right)^2 \right] \tilde{\phi}(\tilde{\mathbf{r}}) + \frac{\tilde{\phi}(\tilde{\mathbf{r}})^4}{4}. \tag{2.68}$$

and the evolution equation becomes

$$\frac{\partial \tilde{\phi}(\tilde{\mathbf{r}})}{\partial \tilde{t}} = \tilde{\nabla}^2 \frac{\delta \tilde{\mathcal{F}}_s \left(\tilde{\phi}(\tilde{\mathbf{r}}) \right)}{\delta \tilde{\phi}(\tilde{\mathbf{r}})} + \tilde{\eta}, \tag{2.69}$$

where $\tilde{\eta}$ is the scaled thermal fluctuations. The scaled variables are defined as

$$\tilde{\mathbf{r}} = q_0 \mathbf{r}, \qquad \tilde{\epsilon} = -\frac{\alpha}{\lambda q_0^4}, \qquad \tilde{\phi}(\tilde{\mathbf{r}}) = \sqrt{\frac{g}{\lambda q_0^4}} \phi(\mathbf{r}), \qquad \tilde{t} = \Gamma \lambda q_0^{6-d} t. \tag{2.70}$$

where the tilde indicates a scaled quantity and d denotes the dimensionality of the problem.

The parameter ϵ in the scaled form of the free energy is related to undercooling. For small undercooling, the minimization of $\tilde{\mathcal{F}}_s$ with varying ϵ provides the phase diagram with the following stable phases [117]: a liquid state and three types of crystalline states that includes body-centered cubic (BCC), effectively two-dimensional hexagon (rods), and effectively one-dimensional stripe phases. For large undercooling, additional stable crystal phases emerge, such as face-centered cubic (FCC) and hexagonal close packed (HCP) phases [117]. Even though the phase diagram does not resemble that of a real material, a portion of the liquid-triangular coexistence region can be superimposed onto the liquid-solid coexistence region of the phase diagram of argon [65], thereby providing a link of the model to a real material system.

Using the PFC evolution equation, one can model a variety of complex phenomena that involve the interplay between crystal orientations, anisotropic interfacial energy, and plastic and elastic deformations. It should be emphasized that all of these effects are naturally included within one consistent formulation in the PFC model. In contrast, the phase-field model requires auxiliary field variables to incorporate these effects. This approach becomes increasingly challenging when multiple effects are simultaneously governing the evolution process.

Despite the success of the PFC method in tackling complex material phenomena, it is still challenging to model real material systems. First, due to the phenomenological origin of its free energy, it is not clear how each parameter affects the material properties, which makes the tunability of the model limited. Second, the number of fitting parameters in Eq. (2.65) is small, which means that the model can only describe a few material parameters correctly. Furthermore, an extension of the model on a phenomenological basis can be less convincing and unsystematic. Recently, Elder et al. [76] established a connection between the PFC method and classical density functional theory (CDFT), which provides the PFC framework with fundamental rigor and enables several consistent and systematic improvements to the model.

2.3.2 Theoretical Development

Subsequent to the phenomenological development of the PFC method, it was shown that, after several approximations, (i) the PFC-type free energy can be derived from the free energy from CDFT [62], and (ii) the evolution equation can be derived from dynamic density functional theory (DDFT) [69, 70, 71]. The connection between the free energies was first presented by Elder et al. [76] in 2007, and established the facts that (i) the PFC free energy is equivalent to the Helmholtz free energy, and (ii) the order parameter of the PFC free energy can be described as an atomic-probability density. These two facts justify the use of the PFC free energy to calculate various

thermodynamic quantities and enables one to consistently compare the predictions from the PFC method to those of other theories and models. This connection also motivates one to incorporate several extensions that have been made to CDFT into the PFC model. These extensions include formulations of the free energy to describe binary systems [76], anisotropic lattices [118], and liquid-crystalline systems [119]. Later, in 2009, a link to DDFT was proposed by Teeffelen et al. [120]. This link provides insight into the underlying assumptions that have been implicitly made in the dynamics of the standard PFC model. Together with the free-energy link, the connection between DDFT and the PFC model suggests an alternative form of the PFC equations based on CDFT and DDFT with fewer approximations.

2.3.2.1 Derivation of Free Energies of PFC from CDFT

Here, an alternative form of the PFC free energy functional will be derived from the free energy functional of CDFT; this free energy functional will be referred to as the CDFT-PFC free energy. We will first give a brief introduction of CDFT in order to formally define the atomic probability density and the Helmholtz free energy. The theory bears close resemblance to the density functional treatment used in quantum mechanics of which the energy can be expressed as a functional of the electron-density field. However, different from the density functional treatment used in quantum mechanics, CDFT considers the equilibrium one-body density $\rho_{eq}(\mathbf{r})$, which is the grand canonical average of the density operator, $\sum_i \delta(\mathbf{r}-\mathbf{r}_i)$ [62, 61]:

$$\rho_{eq}(\mathbf{r}) = \left\langle \sum_i \delta(\mathbf{r}-\mathbf{r}_i) \right\rangle_{GC}, \tag{2.71}$$

where $\mathbf{r}_i$ is the particle position, $\delta(\mathbf{r})$ is the Dirac delta function, and the subscript GC denotes the grand canonical ensemble. One important mathematical theorem to the CDFT formulation is that there is a one-to-one correspondence between $\rho_{eq}(\mathbf{r})$ and

an external potential $V_{ext}(\mathbf{r})$ at any given temperature T, and chemical potential μ. This theorem enables the formulation of an intrinsic free energy functional $\mathcal{F}\big(\rho(\mathbf{r})\big)$ that is a functional of atomic-probability density, $\rho(\mathbf{r})$, which is not necessarily an equilibrium quantity. When $\rho(\mathbf{r}) = \rho_{eq}(\mathbf{r})$, for a corresponding $V_{ext}(\mathbf{r})$, the quantity $\mathcal{F}\big(\rho(\mathbf{r})\big)$ becomes the Helmholtz free energy and satisfies [62, 63]

$$\left.\frac{\delta\mathcal{F}\big(\rho(\mathbf{r})\big)}{\delta\rho(\mathbf{r})}\right|_{\rho=\rho_{eq}} + V_{ext}(\mathbf{r}) - \mu = 0. \tag{2.72}$$

Following Ref. [62], we divide the free energy functional into the ideal and excess parts, i.e., $\mathcal{F}\big(\rho(\mathbf{r})\big) = \mathcal{F}_{id}\big(\rho(\mathbf{r})\big) + \mathcal{F}_{ex}\big(\rho(\mathbf{r})\big)$. The ideal contribution can be obtained exactly from the ideal gas system and is given by

$$\mathcal{F}_{id}\big(\rho(\mathbf{r})\big) = k_B T \int d\mathbf{r}\rho(\mathbf{r}) \left\{\ln[\rho(\mathbf{r})\lambda_T^3] - 1\right\}, \tag{2.73}$$

where λ_T is the de Broglie wavelength and k_B is the Boltzmann constant. The excess contribution yields a hierarchy of direct correlation functions (DCF) through the functional derivative

$$c^{(n)}(\mathbf{r}_1, ..., \mathbf{r}_n; [\rho]) = -\beta \frac{\delta^n \mathcal{F}_{ex}[\rho(\mathbf{r})]}{\delta\rho(\mathbf{r}_1)...\delta\rho(\mathbf{r}_n)}, \tag{2.74}$$

where $\beta = 1/k_B T$. The function $c^{(n)}(\mathbf{r}_1, ..., \mathbf{r}_n; [\rho])$ is the n-body DCF, which contains the information of the inter-particle interactions and determines structural properties of the system. In general there is no exact expression for $\mathcal{F}_{ex}\big(\rho(\mathbf{r})\big)$, and thus numerous techniques have been proposed to approximate this quantity [62]. In the context of freezing, the commonly used approach is to approximate $\mathcal{F}_{ex}\big(\rho(\mathbf{r})\big)$ by a functional Taylor expansion around a uniform density ρ_0 and truncate the expansion beyond the second-order term. By combining the approximate form of $\mathcal{F}_{ex}\big(\rho(\mathbf{r})\big)$ with $\mathcal{F}_{id}\big(\rho(\mathbf{r})\big)$,

the free energy can be expressed as follows [67]:

$$\begin{aligned}\beta\mathcal{F}\big(\rho(\mathbf{r})\big) &= \beta\mathcal{F}[\rho_0] + \beta\mu_0 \int d\mathbf{r}\Delta\rho(\mathbf{r}) + \int d\mathbf{r}\left\{\rho(\mathbf{r})\ln\left[\frac{\rho(\mathbf{r})}{\rho_0}\right] - \Delta\rho(\mathbf{r})\right\} \\ &\quad -\frac{1}{2}\int\int d\mathbf{r}_1 d\mathbf{r}_2 \Delta\rho(\mathbf{r}_1)c^{(2)}(\mathbf{r}_1,\mathbf{r}_2;[\rho_0])\Delta\rho(\mathbf{r}_2), \end{aligned} \tag{2.75}$$

where μ_0 is the chemical potential of the reference state, $\Delta\rho(\mathbf{r}) = \rho(\mathbf{r}) - \rho_0$, and the function $c^{(2)}(\mathbf{r}_1,\mathbf{r}_2;[\rho_0])$ is the two-body DCF of the reference uniform-density state. In order to obtain the CDFT-PFC form of the PFC free energy functional, we first write Eq. (2.75) in terms of a scaled density, $n(\mathbf{r}) = (\rho(\mathbf{r}) - \rho_0)/\rho_0$, and obtain

$$\begin{aligned}\frac{\beta\Delta\mathcal{F}}{\rho_0} &= \int d\mathbf{r}\Bigg\{[1+n(\mathbf{r})]\ln[1+n(\mathbf{r})] - n(\mathbf{r}) + \beta\mu_0 n(\mathbf{r}) \\ &\quad -\frac{\rho_0 n(\mathbf{r})}{2}\int d\mathbf{r}' c^{(2)}(|\mathbf{r}-\mathbf{r}'|)n(\mathbf{r}')\Bigg\}, \end{aligned} \tag{2.76}$$

where the two-body DCF is now assumed to be spherically symmetric. This assumption is valid for a system whose interaction potential is isotropic. Subsequently, two approximations are applied to Eq. (2.76), as proposed in Ref. [76]. The first approximation is the Taylor expansion of the first two terms of the integrand in Eq. (2.76) [76]:

$$[1+n(\mathbf{r})]\ln[1+n(\mathbf{r})] - n(\mathbf{r}) \approx \frac{1}{2}n(\mathbf{r})^2 - \frac{a_t}{6}n(\mathbf{r})^3 + \frac{b_t}{12}n(\mathbf{r})^4, \tag{2.77}$$

where the constants a_t and b_t are set to 1. The constants can be set to other values to account for contributions from the zeroth-mode of higher-order direct correlation functions, [121, 122, 123, 124, 125, 126]. The second approximation is the Taylor expansion of the Fourier transform of the two-body DCF:

$$\rho_0\hat{c}^{(2)}(k) \equiv \hat{C}^{(2)}(k) \approx -\mathcal{C}_0 + \mathcal{C}_2 k^2 - \mathcal{C}_4 k^4, \tag{2.78}$$

where $\mathcal{C}_0$, $\mathcal{C}_2$, and $\mathcal{C}_4$ are fitting constants, k is the magnitude of the reciprocal vector, and the hat denotes the Fourier transform of the corresponding quantity.

Substituting Eq. (2.77) and the inverse Fourier transform of Eq. (2.78) into Eq. (2.76), we arrive at

$$\begin{aligned}\frac{\beta\Delta\mathcal{F}_c\big(n(\mathbf{r})\big)}{\rho_0} &= \int d\mathbf{r}\Bigg[\beta\mu_0 n(\mathbf{r}) + n(\mathbf{r})\frac{1+\mathcal{C}_0+\mathcal{C}_2\nabla^2+\mathcal{C}_4\nabla^4}{2}n(\mathbf{r}) \\ &\quad -\frac{a_t}{6}n(\mathbf{r})^3+\frac{b_t}{12}n(\mathbf{r})^4\Bigg] \\ &\equiv \int f_c\big(n(\mathbf{r})\big)d\mathbf{r}, \end{aligned} \tag{2.79}$$

where $\Delta\mathcal{F}_c$ is the CDFT-PFC form of the PFC free energy functional and f_c is the CDFT-PFC form of the PFC free energy density. The connection between the CDFT and the PFC free energies enables one to identify the PFC free energy as the Helmholtz free energy when $n(\mathbf{r})$ takes the equilibrium profile for a given external potential. The connection also suggests several extensions to the PFC free energy. First, one could improve the approximations in Eq. (2.77) and Eq. (2.78) by including higher-order terms in the series expansions. Alternatively, one could choose different methods to approximate the two-body DCF. Finally, one could consider a different form of $\mathcal{F}_{ex}\big(\rho(\mathbf{r})\big)$ and apply appropriate approximations to arrive at a different variant of the PFC model.

To better understand the effects of the approximations made in Eq. (2.77) and (2.78), let us consider the equilibrium dimensionless one-body density, $n_{eq}(\mathbf{r})$, which can be expressed as a summation of density waves [78]:

$$n_{eq}(\mathbf{r}) = \bar{n}\left(1+\sum_i u_i e^{i\mathbf{G}_i\cdot\mathbf{r}}\right), \tag{2.80}$$

where $\bar{n}$ is an average of $n_{eq}(\mathbf{r})$, $\mathbf{G}_i$ is a reciprocal lattice vector, and u_i is a density wave amplitude. A typical two-body DCF, without the approximation of Eq. (2.78),

yields a density profile ($n_{eq}(\mathbf{r})$) of the crystal phase that is sharply peaked around crystal lattice positions. Thus, the summation in Eq. (2.80) contains a large number of required terms in order to account for high frequency modes associated with localized peaks, which leads to a large system of equations to be solved. When the approximation in Eq. (2.78) is applied, high-frequency components of $n_{eq}(\mathbf{r})$ becomes energetically unfavorable and subsequently leads to fewer summation terms needed to represent the profile. Additionally, when the approximation in Eq. (2.77) is applied, the amplitude of $n_{eq}(\mathbf{r})$ becomes smaller due to a larger energy penalty for large values of $n_{eq}(\mathbf{r})$. As a result of these two approximations, the profile of $n_{eq}(\mathbf{r})$ is significantly less localized, resulting in a density profile that needs less spatial resolution to resolve and ultimately leading to more computationally efficient calculations.

2.3.2.2 Derivation of PFC Evolution Equations from DDFT

We will now present the link between the evolution equation of the PFC method and that of CDFT, known as dynamic density functional theory (DDFT). We begin by providing a brief overview of DDFT. The evolution equation for CDFT can be formulated by introducing the time-dependent one-body density, $\rho(\mathbf{r}, t)$, as a noise-average of an instantaneous density operator [69, 70, 71]. By considering overdamped Brownian dynamics without hydrodynamic interactions, one can describe an evolution of a particle system by stochastic differential equations governing particle positions (Langevin equations), or a deterministic evolution equation of a probability density (Smoluchowski equation). Marconi and Tarazona [70, 71] employed the former equations while Archer and Evans [69] started with the latter equation to arrive at the equation of motion for $\rho(\mathbf{r}, t)$:

$$\frac{\partial \rho(\mathbf{r}, t)}{\partial t} = \gamma^{-1} \nabla \cdot \left[\rho(\mathbf{r}, t) \nabla \frac{\delta \mathcal{F}\big(\rho(\mathbf{r}, t)\big)}{\delta \rho(\mathbf{r}, t)} \right], \tag{2.81}$$

where γ is the friction coefficient. By writing $\rho(\mathbf{r},t) = \rho_0(n(\mathbf{r},t)+1)$, the evolution equation in Eq. (2.81), becomes

$$\frac{\partial n(\mathbf{r},\tau)}{\partial \tau} = \nabla \cdot \left\{ [n(\mathbf{r},\tau)+1] \nabla \frac{\delta \Delta \tilde{\mathcal{F}}\big(n(\mathbf{r},\tau)\big)}{\delta n(\mathbf{r},\tau)} \right\}, \tag{2.82}$$

where $\tau = \gamma^{-1} k_B T \rho_0 t$ is the rescaled time and $\Delta\tilde{\mathcal{F}} = \Delta\mathcal{F}/k_B T\rho_0$ is the dimensionless free energy.

As suggested by Teeffelen et al. [120], one can obtain the PFC evolution equation by replacing the spatially dependent factor in front of the gradient term with its average value. In this case, we let $n(\mathbf{r},\tau)+1 \approx \bar{n}+1$. With this approximation, we obtain

$$\frac{\partial n(\mathbf{r},\tau)}{\partial \tau} = (\bar{n}+1)\nabla^2 \frac{\delta \Delta \tilde{\mathcal{F}}\big(n(\mathbf{r},\tau)\big)}{\delta n(\mathbf{r},\tau)}, \tag{2.83}$$

which, aside from the noise term, has a similar form to the PFC evolution equation, Eq. (2.69). From the DDFT derivation, the noise term will not be present in the evolution equation because of the noise averaging procedure that is performed on the Langevin equations. Therefore, the presence of the noise term in Eq. (2.69) is not justified from fundamental considerations because one would overestimate the fluctuations [71]. However, the study by Archer and Rauscher [127] showed that the noise term is present in the evolution equation if one instead interprets the density field as a temporally coarse-grained density operator. Nevertheless, if one adopts this interpretation, the free energy functional in the evolution equation will no longer be the Helmholtz free energy and is generally unknown. Despite these different viewpoints, the noise term is usually included on the basis of necessity to model phenomena such as homogeneous nucleation that cannot be simulated without the noise term.

To evaluate whether or not a more rigorous evolution equation (Eq. (2.82)) would improve the predictive capability of the original PFC model, a variant PFC model

termed PFC1 was obtained by Teeffelen et al. by approximating the two-body DCF (Eq. (2.78)) of the PFC free energy while using the full DDFT evolution equation [120]. The PFC1 equations are more difficult to solve because of the nonconstant mobility. They compared the two models by measuring the velocity of the crystal-liquid interface during solidification. Their results showed that the velocities calculated for both models as a function of the form of the two-body DCF are similar; the results from the PFC1 model was slightly closer to those calculated from DDFT. This study shows that the dynamics of both the PFC1 and the original PFC models are consistent with that of DDFT. Nevertheless, if one seeks to obtain only qualitative consistency with DDFT, the original PFC model is more attractive because of its simpler free energy and evolution equations, which are computationally more efficient.

We have presented the two developments of the "original" PFC model, which emerged as a promising continuum approach with atomic spatial resolution at diffusive time scales. However, the model arising from these initial developments is limited in its predictive capability and numerical efficiency. To enable the model to quantitatively predict material phenomena and to do this efficiently, several research groups have extended the model from its initial development by incorporating more complicated free energies and evolution dynamics, and a formulation that "coarse-grains" the PFC order parameter for computational efficiency. These further developments are briefly summarized in the next section.

2.4 Further Development of the Phase-Field Crystal Model

Further extensions to the PFC model can be divided into three categories. The first category involves extensions of the PFC free energy to improve the capability of the model to quantitatively predict thermodynamic properties of materials, and to access different crystal structures or phases. The second category consists of adjustments to the PFC evolution equations to describe mechanisms that occur on multiple

time scales. The third category deals with coarse-graining of the model description so that the evolution equation of the amplitude of the density waves is solved in place of the dynamics of the density field. This approach increases numerical efficiency and provides a promising framework for larger-scale simulations.

2.4.1 Extension of Free Energy

The free energy of the PFC model has been modified in four different ways to improve the accuracy of the model when predicting material properties and its application to a wider range of material systems. In the first modification, Jaatinen et al. [121] was able to accurately predict multiple thermodynamic properties simultaneously by including additional fitting parameters into the PFC free-energy. This was achieved by using the ideal contribution of the free energy in Eq. (2.77) where the constants are not equal to one and approximating the two-body DCF to the eighth-order in k [121]. These two improvements allow the PFC method to predict multiple thermodynamic quantities of Fe in agreement with those from experiments and atomistic simulations. In a second modification, the free energy was extended to model binary (two-component) systems by including the density field of a second species [76, 123, 128, 129, 130]. The binary model was employed to study many phenomena such as phase segregation [76], eutectic solidification [76, 131], and the Kirkendall effect [132]. In a third modification, the gradient and nonlinear terms of the free energy were modified to systematically model polymorphism. Wu and Karma were able to stabilize an FCC structure over the BCC structure by extending the SH-PFC form of the PFC free energy with a higher-order gradient term [78]. Greenwood et al. were able to predict three-phase coexistence lines as well as peritectic points for both two- and three-dimensional systems by phenomenologically constructing the peaks of the two-body DCF in Fourier space using Gaussian kernels [122, 133]. And Wu et al., motivated by the techniques used to control stability of different patterns in the study

of pattern formation [134, 135, 136], showed that it is possible, in two-dimensions, to yield triangle-square and square-liquid coexistence regions as well as a stable square lattice by introducing terms of the form $\phi^2\nabla^{2n}\phi^2$ and $|\nabla\phi|^{2n}$ into the free energy functional [137]. In a fourth modification, an orientational field was added to the PFC free energy to account for orientationally anisotropic systems [119, 138, 139]. The anisotropic model of [119] was used by Achim et al. [140] to calculate a liquid-crystal phase diagram where the isotropic, stripe, nematic, smectic A, columnar, and plastic (nonliquid) crystalline phases were found to be stable.

2.4.2 Evolution Equation

One of the additions to the PFC dynamics is the inclusion of a fast time scale to accommodate processes that occur much faster than diffusion [141, 142]. For example, to model elasto-plastic deformation, one needs the elastic relaxation to operate on a shorter time scale than that of the diffusive time scale of mass transport. By including a second-order time derivative, the modified PFC (MPFC) equation is expressed in the form of the damped wave-equation:

$$\frac{\partial^2\phi}{\partial t^2} + \beta\frac{\partial\phi}{\partial t} = \alpha^2\nabla^2\frac{\delta\mathcal{F}}{\delta\phi}, \tag{2.84}$$

where α and β are phenomenological constants. This form of the evolution equation allows a transient mode of wave propagation to mimic elastic relaxation, and a long or diffusive mode of wave propagation for mass transport. From the linear stability analysis, the values of α and β are determined so that the effective elastic interaction length is larger than the system domain size and the effective elastic interaction time is well separated from the diffusion time, but still kept several orders of magnitude larger than the true phonon time scale to maintain computational efficiency. Together, this scheme yields the elastic relaxation that is effectively instantaneous compared to the

diffusive phenomena but still retains the efficiency of the PFC method over atomistic models. With this approach, simulations of nanocrystalline samples under uniaxial tensile load were performed, and the simulation results show multiple strain relaxation mechanisms such as dislocations annihilation at surfaces or grain boundaries, grain coalescence via grain rotation, and void formation at triple junctions and at high-angle grain boundaries [142]. These results are consistent with experimental observations [143, 144].

The MPFC has also been linked to a more general dynamic theory by Galenko et al. [145]. They proposed that the MPFC as well as PFC dynamics are instances of a more general evolution equation [146]:

$$\frac{\partial \phi}{\partial t} = \nabla \cdot \int_{\infty}^{t} M(t - t^*) \nabla \frac{\delta \mathcal{F}}{\delta \phi} dt^*, \tag{2.85}$$

where $M(t - t^*)$ is a memory function that controls how the past trajectory affects the current dynamics. By setting the memory function as a delta function, the standard diffusive dynamics is recovered. When the memory function is set to a constant value, dissipative (undamped) dynamics is obtained. Lastly, when the memory function is set to an exponential function, the damped wave equation, analogous to the MPFC arises. Furthermore, Majaniemi and Grant explored an alternative origin of the MPFC model from extended hydrodynamics of solids [147]. They derived the evolution equations that govern the displacement fields resulting from phonon interactions as well as the hydrodynamic variables of a liquid system in order to model non-equilibrium phenomena in crystalline solids. By assuming linear elastic coupling, the set of hydrodynamic equations can be combined to yield one transport equation governing the time variation of a number density. This transport equation exhibits three characteristic time scales: a fast propagating and two slow diffusive time scales [147]. In the limit where the diffusion current dominates, the MPFC can be obtained.

2.4.3 Coarse-graining of the PFC equations using Amplitude Formulations

Although the PFC model provides more numerical efficiency than CDFT and MD, the atomic length-scale fluctuations of the atomic-number density still limit the applicability of the PFC model to capture experimentally observable length scales. For example, to obtain an accurate representation of the the fluctuations, approximately nine grid points per period of fluctuation in one dimension is required. As one period of fluctuation is on the order of angstroms, a micron scale simulation will take about 10^5 grid points on a uniform mesh in each direction. This would make three-dimensional calculations beyond nanoscale difficult.

In order to circumvent these difficulties, an alternative description of the model can be used. One method is to replace the modes with the amplitude of the basis vectors of a given periodic structure. The motivation for this "coarse-graining" process can be illustrated by representing the 1-dimensional density field of a perfect crystalline phase with $\phi = A\sin(kx)$. To numerically resolve the sinusoidal variation of ϕ, a spatial grid with a sufficient resolution (~ 9 points) is necessary. On the other hand, ϕ can be equally represented by only keeping track of the amplitude A, which is constant in this case. In inhomogeneous regions such as interfaces, the amplitude will vary, but this variation is on a larger length-scale than the sinusoidal variation of ϕ. The behavior of the amplitude function is therefore ideal for adaptive mesh refinement (AMR) technique, which increases computational efficiency.

Once the amplitude functions of a crystal structure are chosen, the next step is to derive an evolution equation for the amplitudes. Several techniques have been developed for this purpose in pattern formation studies; we refer readers to a concise overview of these methods in Ref. [148] and the references therein. However, due to mathematical complexity of these methods, Goldenfeld, Athreya, and Dantzig (GAD) [148, 149, 150] instead employed a heuristic approach, which is referred to as "quick

and dirty" RG (QDRG) method. This method is less mathematically rigorous than the conventional methods but is appealing due to its simplicity.

The QDRG was employed to simulate grain nucleation and growth in two-dimensions. Their results show good agreement with those from full PFC simulations, while the simulation time is reduced by up to a factor of six [150]. In a later study, Athreya et al. [151] presented a hybrid algorithm that solves the amplitude equation in different regions using a cartesian or polar representation. Along with an approximation to the polar representation, which is referred to as frozen phase gradient approximation, the hybrid approach led to the acceleration of the simulation by three orders of magnitude compared to the amplitude-based simulation of growth of solid precipitates using a uniform grid in two-dimensions.

A further extension to the amplitude formulation was performed by Yeon et al. [152] to describe a system in which the local average of the density field varies in space. This extension enabled amplitude-based modeling of phase transformation processes in systems where the solid density differs from that of the liquid, which allowed simulations of coarsening in a system where the solid and liquid phases coexist. A three-dimensional simulation was performed and shown to be computationally inexpensive. The amplitude formulation was also applied to a binary system with varying degrees of approximation [123, 130].

Apart from the benefit in computational efficiency, the amplitude formulation, or coarse-graining techniques in general, provide a link between PFC-type or CDFT-type models and phase-field-type models [153, 154, 155, 156]. This connection enables one to relate the parameters calculated from PFC and CDFT models to those of the phase-field models, giving the phenomenological phase-field order parameters more physical basis. Furthermore, since the phase-field model can be related to the sharp-interface model, the coarse-grain technique allows a multi-scale connection from atomic-scale models such as CDFT to classical sharp-interface models.

CHAPTER III

Stability of Strained Thin Films with Interface Misfit Dislocations: A Multiscale Computational Study

3.1 Overview

In this chapter, we examine the contributions of the misfit strain, interfacial misfit dislocations, film surface and interface to the stability of a single-crystal, internal-defect-free, flat film. We use an equilibrium dislocation model based on the Peierls-Nabarro (PN) formulation [42, 43], which describes long-range elastic fields by continuum equations and takes into account a plastic deformation energy at the film/substrate interface in terms of a corrugation potential that can be obtained from first-principles calculations. In addition to the misfit dislocation/deformation energetics, we use a first-principles method based on electronic density functional theory to calculate the surface/interfacial energy as a function of film thickness and a surface strain. Specifically, we focus on Fe/Mo(110) and Fe/W(110) systems, which are well characterized through fundamental experimental studies that relate the growth, morphology and properties of magnetic thin films [44, 45, 46, 26, 47, 36]. However, the method presented can be applied to a broader range of metallic thin film material systems that form misfit dislocations. We find that, through the competition between

energetics of the misfit dislocations, misfit strain, film surface and interface, there is a significant driving force for a flat film to form thinner and thicker regions, leading to the dewetting process. This driving force is more than one order of magnitude larger than that caused by the film-thickness dependence of the energy arising from the surface stress considered in a recent study by McCarty *et al.* [38]. In addition, we find that non-monotonic variations in the thickness-dependent surface/interfacial energy may give rise to a metastable behavior of the film at certain thicknesses.

In Section 3.2, we discuss the energetic contributions to the total energy of the system. We consider the contributions to the energy from the misfit strain (Section 3.2.2), the misfit dislocations (Sections 3.2.3 and 3.2.4), and the surface/interface (Section 3.2.5). We then present the results and discussions in Section 3.3. Specifically, we discuss the prediction of the dislocation configuration from the model in Section 3.3.1, followed by the result of the energies from the misfit dislocations and the misfit strain in Section 3.3.2. The effect of the surface stress is discussed in Section 3.3.3 and the combined energy from all contributions is presented in 3.3.4. Furthermore, we discuss the applicability of our method to other epitaxial systems in Section 3.3.5. Finally, we conclude the chapter with the summary in Section 3.4.

3.2 Formulation

For a system with a cubic structure, we consider a film with a finite thickness, h, and a lattice mismatch from a semi-infinite substrate described by an intrinsic misfit strain $\eta^m_{kl} = \delta_{kl}(a^f - a^s)/a^s$. The superscript m refers to misfit. The symbol δ_{kl} is the Kronecker delta while a^f and a^s are lattice parameters of the film and the substrate, respectively. The subscripts k and l $(= 1, 2, 3)$ denote directions along an orthogonal basis, x_k, where x_1 and x_2 lie within the film/substrate interface plane and the x_3 axis is normal to the interface. The origin is located at the interface between the film and the substrate. In the Fe/Mo(110) and Fe/W(110) systems, $\eta^m_{kl} \approx 10\%$.

The misfit dislocations considered here are geometrically necessary defects that occur as a part of a semicoherent interface to reduce misfit strain [157]. On the body-centered-cubic (BCC) (110) plane, the dislocations are observed along the $[00\bar{1}]$ direction (dislocation array) and the $[1\bar{1}1]/[1\bar{1}\bar{1}]$ directions (dislocation network) [45, 46, 158]. To simplify the calculations, the relaxation directions are limited to the orthogonal $[00\bar{1}]$ and $[\bar{1}10]$ directions, corresponding to arrays of dislocations along $[\bar{1}10]$ and $[00\bar{1}]$, respectively. These two orthogonal dislocation arrays are assumed to form a dislocation network. Along the $[\bar{1}10]$ and $[00\bar{1}]$ directions, we consider a periodic insertion of planes (edge dislocations) at every P substrate lattice spacing; therefore, the dislocation spacing p_i is given by

$$p_i = Pa_i^s \equiv Pc_i = (P+1)(a_i^f - u_i^{res}), \tag{3.1}$$

where a_i^f (a_i^s) is the relaxed lattice spacing of the film (substrate) along the x_i-direction, and c_i is the reference lattice spacing that is taken to be the substrate lattice spacing. The subscript i ($= 1, 2$) denotes the orthogonal directions on the interface plane and in this model, $i = 1$ and $i = 2$ refer to the $[\bar{1}10]$ and $[00\bar{1}]$ directions, respectively. In addition to the subscript i, the subscript j, where $j = 1, 2$, and $j \neq i$, is used throughout the chapter, unless otherwise noted. The variable u_i^{res} is the displacement along the x_i-direction due to an average residual deformation that needs to be accommodated in the film to maintain coherency of an interface in regions between dislocations. It should be noted that for Fe/Mo and Fe/W parameters, u_i^{res} is minimized when $P = 10$.

Equation (3.1) assumes that there is one extra lattice of the film material in a dislocation period. For a simple-cubic lattice of which the lattice spacing is equal to the interplanar spacing, this is equivalent to inserting one extra plane per one dislocation period [159, 95]. On the BCC (110) plane, there are two planes per one

lattice spacing along the $[00\bar{1}]$ and $[\bar{1}10]$ directions. Therefore, Eq. (3.1) implies that two extra planes are inserted per one dislocation spacing instead, which is necessary to satisfy periodicity of the atomic structure.

3.2.1 Energy Considerations

Analogous to the work by Cammarata *et al.* [160], the energy of the system is partitioned into three parts.

(i) Homogeneous strain energy, E^h, which approximates an energy resulting from u_i^{res}. This is similar to volume elastic energy resulting from coherency strain in Cammarata's formulation [160].

(ii) Energy associated with the formation of misfit dislocations. Following the PN formulation [96] and the work by Willis *et al.* [161], this energy can be further divided into (a) dislocation elastic energy, E^e, associated with long-range, periodic elastic fields originating from the misfit dislocations and (b) plastic deformation energy (often termed "misfit" energy [96]), E^p, associated with an atomic disregistry across the glide plane.

(iii) Surface/interfacial energy, E^s, associated with the chemical contribution from missing bonds at the surface and dissimilar bonds at the film/substrate interface.

For brevity, we will also refer to the combination of $E^h + E^e + E^p$ as the dislocation/deformation energy hereafter.

3.2.2 Homogeneous Strain Energy

In the absence of misfit dislocations, the film is strained to coherently match the substrate lattice. Following Ref. [161], the displacement, u_k^m, is a function of x_3 only. Together with the conditions of a stress-free film surface, free expansion along the

x_3-direction and elastic isotropy,

$$u_1^m = u_2^m = 0, \quad u_3^m = \left[\frac{\nu}{1-\nu}(\eta_{11}^m + \eta_{22}^m) + \eta_{33}^m \right] x_3, \tag{3.2}$$

where ν is the Poisson's ratio. Throughout this chapter, the Voigt average elastic constants tabulated in Ref. [96] will be used for the Fe/Mo and Fe/W systems.

The square dislocation network results from the formation of two perpendicular dislocation arrays whose Burger's vectors are $(b_1, 0, 0)$ per period p_1 and $(0, b_2, 0)$ per period p_2. This dislocation network reduces the effect of η_{kl}^m through contributions from the displacements [161]:

$$\begin{aligned} u_1^n &= -\frac{b_1}{p_1} x_1, \quad u_2^n = -\frac{b_2}{p_2} x_2, \\ u_3^n &= \frac{\nu}{1-\nu} \left[\frac{b_1}{p_1} + \frac{b_2}{p_2} \right] x_3. \end{aligned} \tag{3.3}$$

This form of the displacement fields is chosen to yield a homogeneous stress state with the same boundary conditions as those corresponding to Eq. (3.2).

The resulting strain ($\bar{e}_{kl}$) and stress ($\bar{\sigma}_{kl}$) tensors originating from $u_k^m + u_k^n$ contribute to the homogeneous strain energy E^h. Using Hooke's law, $\bar{\sigma}_{kl}$ can be expressed as

$$\begin{aligned} \bar{\sigma}_{11} &= -\frac{2\mu}{1-\nu} \left[\frac{b_1}{p_1} + \eta_{11}^m + \nu \left(\frac{b_2}{p_2} + \eta_{22}^m \right) \right], \\ \bar{\sigma}_{22} &= -\frac{2\mu}{1-\nu} \left[\nu \left(\frac{b_1}{p_1} + \eta_{11}^m \right) + \frac{b_2}{p_2} + \eta_{22}^m \right], \end{aligned} \tag{3.4}$$

where μ is the shear modulus and all other elements of the stress tensor are zero. Here, the Burger's vectors are assumed to be equal to the lattice spacing of the film material, $b_i = a_i^f$. In this case, the quantity $b_i/p_i + \eta_{ii}^m$ (no summation) at the right-hand side of Eq. (3.4) can be written, using Eq. (3.1), as $[a_i^f - (a_i^f - u_i^{res})]/(a_i^f - u_i^{res})$, which is the

misfit strain between the bulk film (a lattice spacing of a_i^f) and the homogeneously deformed film with a lattice spacing of $a_i^f - u_i^{res}$.

The homogeneous strain energy per unit area can then be expressed as

$$E^h = \frac{h}{2}\bar{\sigma}_{kl}(\bar{e}_{kl} - \eta_{kl}^m). \tag{3.5}$$

Due to the boundary condition at the film surface, E^h is independent of η_{33}^m.

3.2.3 Dislocation Elastic Energy

In order to calculate E^e, we follow a formulation of the misfit dislocation model proposed by Merwe [94]. This method employs the Airy stress function, χ_i, represented by a Fourier series, to describe the stress fields associated with misfit dislocation arrays (along x_j-direction) in the form of

$$\begin{aligned}
\chi_i^s &= \sum_{n=1}^{\infty}(F_n + G_n z)e^{mx_3}\cos(mx_i), \\
\chi_i^f &= \sum_{n=1}^{\infty}\Big[(A_n + C_n x_3)\cosh(mx_3) \\
&\quad + (B_n + D_n x_3)\sinh(mx_3)\Big]\cos(mx_i),
\end{aligned} \tag{3.6}$$

where $m = 2\pi n/p_i$. The variables A_n, B_n, C_n, D_n, F_n, and G_n are Fourier coefficients which are to be determined. A plane strain condition is assumed throughout this analysis and the corresponding stress tensor, σ_{kl}, can be calculated from

$$\sigma_{ii} = \frac{\partial^2\chi_i}{\partial x_3^2}, \quad \sigma_{33} = \frac{\partial^2\chi_i}{\partial x_i^2}, \quad \sigma_{i3} = -\frac{\partial^2\chi_i}{\partial x_3 \partial x_i}, \tag{3.7}$$

where the superscripts s and f have been omitted and σ_{jj} can be calculated from the plane strain condition. There is no summation over the repeated indices. The stresses in Eq. (3.7) must satisfy the mechanical equilibrium condition as well as the boundary

conditions. In this model, the boundary conditions include (a) the vanishing stresses at $x_3 \to -\infty$, (b) the free surface at $x_3 = h$, (c) the continuity of shear and normal stresses at the interface ($x_3 = 0$), (d) the continuity of the normal displacement at the interface [162], and (e) the PN condition at the interface. The PN condition is the balance between the elastic interfacial stress and the restoring force stress from the atomic restoring force potential. For the BCC (110) plane, the restoring force stress can be obtained by taking a derivative of the generalized stacking fault energy, E_{gsfe}, also referred to as the γ surface, in the first-harmonic Fourier expansion of the form:

$$E_{gsfe} = E_0 + V\cos\left[\frac{3\pi}{r}\Big(\frac{U_1}{\sqrt{6}} + \frac{U_2}{\sqrt{3}}\Big)\right] + V\cos\left[\frac{3\pi}{r}\Big(\frac{U_1}{\sqrt{6}} - \frac{U_2}{\sqrt{3}}\Big)\right], \quad (3.8)$$

where U_i is the disregistry, or the relative displacement of the film atoms at the interface from their equilibrium positions (without dislocations) along the x_i-direction [163]. The contour plot of E_{gsfe} on the BCC (110) plane is shown in Fig. 3.1. The variable $r = \sqrt{3}a^s/2$ is the nearest-neighbor spacing of the reference lattice. The coefficient V parameterizes the resistance of the glide plane to shear and the details of the first-principles calculations are discussed below.

The generalized stacking fault energy[1] is calculated using the Vienna *ab-initio* simulation program (VASP) [164, 165, 166], which employs a plane-wave basis set for the electronic states with a cutoff energy of 400 eV. The calculations make use of the Projector Augmented Wave (PAW) method [167, 168], and the spin-polarized generalized gradient approximation (GGA) due to Perdew, Burke and Ernzerhof (PBE) [169].

To compute E_{gsfe}, we consider supercells consisting of 12 Mo(110) substrate layers, followed by 12 Fe(110) layers pseudomorphically strained to the lattice constant of

[1]The calculations of the generalized stacking fault energies were performed by our collaborators, Bo Yang, Dong-Hee Lim, and Mark Asta [170].

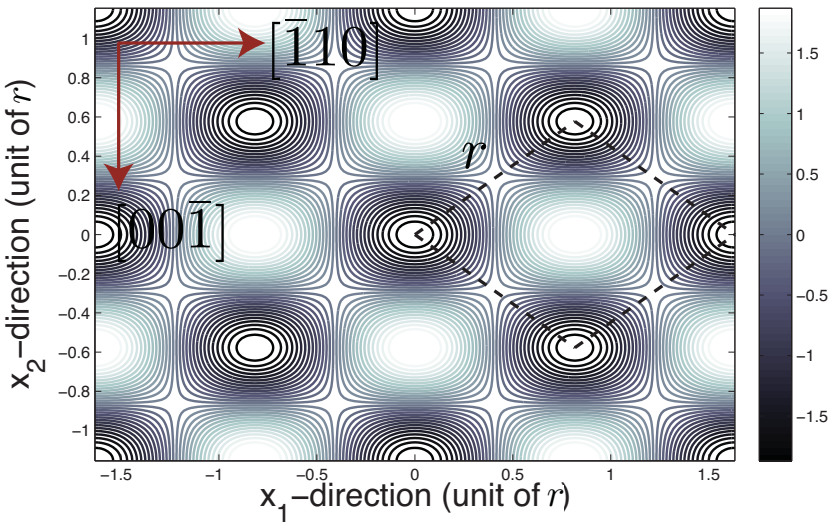

Figure 3.1: Contour plot of $(E_{gsfe} - E_0)/V$ showing the BCC(110) substrate potential. The constant r is the nearest-neighbor spacing. The dash lines enclose one unit cell.

the substrate. The 24 layers are periodically repeated in the direction normal to the substrate, giving rise to two interfaces in the cell, with a periodic length adjusted to give zero stress normal to the interface plane. The periodic directions for the supercell in the interface plane are taken to be along the BCC directions $[1/2, -1/2, 1/2]$ and $[1/2, -1/2, -1/2]$, giving one atom per layer. The electronic states are sampled by employing a k-point mesh with a density of $16 \times 16 \times 1$ in the Brillouin zone of the supercell. The energy is calculated as a function of relative displacements, U_1 and U_2, of the Fe layers relative to the substrate. For each value of U_1 and U_2 the positions of all of the atoms in the supercell are allowed to relax in the direction normal to the interface, under the constraint of fixed periodic length normal to the interface. The resulting energies as a function of U_1 and U_2 are then used to extract the parameters E_0 and V in Eq. (3.8).

For the Fe/Mo system, we calculate V for two cases, one for the glide plane between the substrate and the first layer of Fe ($V_{0/1}^{Fe/Mo}$), and another for the glide plane between the first and the second layer of Fe ($V_{1/2}^{Fe/Mo}$). For the former, $V_{0/1}^{Fe/Mo} =$

-0.220 eV (per area of an interface atom), and for the latter $V_{1/2}^{Fe/Mo} = -0.218$ eV. In this study, $V_{0/1}^{Fe}$ will be used in Eq. (3.8). As mentioned later, a small difference in these values do not alter the conclusions. For the Fe/W system, we find $V_{0/1}^{Fe/W} = -0.266$ eV.

By differentiating Eq. (3.8) with respect to U_i and dividing the resulting expression by an atomic area of $2\sqrt{2}r^2/3$, the restoring force stress along the i-direction is obtained and the PN condition at the interface can be expressed as

$$\frac{\tau_i}{2\pi} \sin\left[\frac{2\pi U_i}{c_i}\right] = \sigma_{i3}|_{x_3=0}, \tag{3.9}$$

where $\sigma_{i3}|_{x_3=0}$ is the shear stress at the interface from Eq. (3.7). The variable τ_i takes the value of $-3\sqrt{3}\pi^2 V/r^3$ for the dislocation along $[00\bar{1}]$ and $-3\sqrt{6}\pi^2 V/r^3$ for the dislocation along $[\bar{1}10]$.

The variable U_i can also be written as

$$U_i = -\frac{c_i}{2} - \frac{c_i}{p_i}x_i + u_i^f|_{x_3=0} - u_i^s|_{x_3=0}, \tag{3.10}$$

where $u_i^f|_{x_3=0}$ ($u_i^s|_{x_3=0}$) is the tangential displacement along the x_i-direction at the interface of the film (substrate). The term $-c_i/2 - c_i x_i/p_i$ corresponds to the relative displacement of atoms across the interface without a deformation from the misfit dislocations.

The boundary conditions (a)-(e) mentioned previously yield a system of equations to be solved for the unknown Fourier coefficients of the stress function. Here, we employ a publicly available subroutine which finds the zero of a system of nonlinear equations using the modified Powell hybrid method [171].

The dislocation elastic energy from the misfit dislocations per unit area can be

calculated as

$$E^e = -\frac{1}{2p_i} \int_{-p_i/2}^{p_i/2} \sigma_{i3}(u_i^f - u_i^s)|_{x_3=0}\ dx_i. \tag{3.11}$$

This equation gives an energy associated with a dislocation array along one direction. Note that since there is no interaction term when dislocation arrays are perpendicular to one another, the energy of the two perpendicular dislocation arrays is simply a sum of the energies associated with each individual dislocation array.

3.2.4 Plastic Deformation Energy

By integrating the left hand side of Eq. (3.9) with respect to U_i and then integrating over one dislocation spacing, the plastic deformation energy per unit area is obtained:

$$E^p = \frac{\tau_i c_i}{4\pi^2 p_i} \int_{-p_i/2}^{p_i/2} \left[1 - \cos\left(\frac{2\pi U_i}{c_i}\right)\right]\ dx_i. \tag{3.12}$$

For each dislocation direction, the dislocation elastic energy in Eq. (3.11) and the plastic deformation energy in Eq. (3.12) are summed, and subsequently added to the homogeneous strain energy in Eq. (5) to obtain the dislocation/deformation energy. It should be noted that in the results section, the dislocation/deformation energy will be expressed in terms of an energy per area of a surface atom (energy/surface atom) instead of per unit area.

3.2.5 Surface/Interfacial Energy

To obtain surface/interfacial energy, E^s for the Fe/Mo system, we first calculate the surface/interfacial energy of the pseudomorphic Fe film, E^s_{pseudo}, and then calculate the strain-dependent correction to E^s_{pseudo} by considering the effect of surface

stress.

3.2.5.1 Surface/Interfacial Energy of Pseudomorphic Film

The energy calculations are based on the framework of electronic density functional theory employing VASP, the PAW method, and the PBE-GGA approximation, as described above for the calculations of E_{gsfe}. Surface and corresponding bulk energies are computed for four systems: (i) pure Fe with a (110) surface, and an in-plane lattice constant strained to match that of bulk Mo, (ii) pure Fe with a (110) surface, and an unstrained in-plane lattice constant, (iii) pure Mo with a (110) surface and an unstrained in-plane lattice constant, and (iv) a Mo(110) substrate with a finite number (n) of Fe layers.

For the systems (i)-(iii), energy calculations are performed for Fe and Mo slabs containing variable numbers of layers within a supercell with a periodic length normal to the surface of 26 Mo interplanar spacings (5.7912 nm). Using this supercell geometry, the energy is computed for 4-18 layers bounded by vacuum, and the resulting energy as a function of thickness is used to compute the energy per atom (E_{Fe} and E_{Mo}) of the corresponding bulk system (from the slope of the total slab energy versus number of layers), and the associated surface energies (from the total energy of the slabs minus the number of layers times the corresponding bulk energies, divided by the total surface area).

For the system (iv), the total excess energy (surface plus Fe/Mo interfacial energies) is calculated using similar supercell geometries with 9 Mo layers, bounded on top and bottom by n Fe layers pseudomorphically strained to be epitaxial on the substrate. For n=1-4 the total excess energy of the thin film is computed as

$$\frac{1}{2A}\left(E_{slab} - 9E_{Mo} - 2nE_{Fe}\right), \tag{3.13}$$

where E_{slab} is the total energy of the Fe/Mo/Fe slab (system (iv)), E_{Mo} is the energy per atom of bulk Mo (system (iii)), E_{Fe} is the energy per atom of bulk Fe (system (i)) and A is the surface area on one side of the slab. This total excess energy per surface atom is the surface/interfacial energy of pseudomorphic film, E^s_{pseudo}.

The results for E^s_{pseudo} are extended to $n = 10$ layers by employing slabs containing 10 Mo layers bounded on one side by an n-layer Fe film. The results presented below are derived by employing a k-point mesh of $20 \times 20 \times 1$, and a choice of the supercell periodic length normal to the surface that ensures a minimum vacuum-layer spacing of 1.35 nm. Convergence checks are performed to examine the following effects: (i) slab and vacuum thickness, (ii) Fourier grid density for the representation of the charge density, (iii) plane-wave cutoff and (iv) k-point sampling. The values of E^s_{pseudo} are estimated to converge to a precision within 0.01 eV/surface atom, and differences in E^s_{pseudo} between films of differing thicknesses are estimated to converge to a higher precision on the order of 0.001 eV/surface atom.

3.2.5.2 Surface Stress

The quantity E^s_{pseudo} in the previous section includes the surface/interfacial energy of the pseudomorphic Fe on Mo(110) substrate. However, the formation of misfit dislocations reduces the strain on the surface significantly and changes the surface energy. The strain-dependent correction to E^s_{pseudo} can be calculated by taking into account the effect of the surface stress.

We denote γ as the excess free energy per surface area due to the presence of the surface and σ^s_{ij} as the surface stress in the Lagrangian coordinate. By definition [172]

$$\sigma^s_{ij} = \frac{\partial \gamma}{\partial e^s_{ij}}, \tag{3.14}$$

where e^s_{ij} is the surface strain and the subscripts i and j denote directions on the

surface plane ($i, j = 1, 2$). If the surface energy at a state of deformation $e^s_{ij}(a)$ is known, the surface energy at a state of deformation $e^s_{ij}(b)$ can be obtained by

$$\gamma_b \;=\; \gamma_a + \sum_{i,j=1}^{2} \int_a^b \sigma^s_{ij} de^s_{ij}, \tag{3.15}$$

where γ_a and γ_b are the surface energies at the states of deformation $e^s_{ij}(a)$ and $e^s_{ij}(b)$, respectively. As a first-order approximation, it is assumed that σ^s_{ij} is constant throughout the deformation process and independent of film thickness. With this approximation, the surface energy is a linear function of the surface strain or

$$\gamma_b - \gamma_a = \sum_{i,j=1}^{2} \sigma^s_{ij} \left[e^s_{ij}(b) - e^s_{ij}(a) \right]. \tag{3.16}$$

Since the misfit dislocations are restricted to form along x_1- and x_2-directions, the surface strain tensor contains no shear terms and Eq. (3.16) can be simplified to

$$\gamma_b - \gamma_a = \sum_{i=1}^{2} \sigma^s_{ii} \left[e^s_{ii}(b) - e^s_{ii}(a) \right]. \tag{3.17}$$

Values of the elements of the surface stress tensor are obtained from the first-principles calculations of the surface energies of strained (system (i)) and unstrained Fe (system (ii)) described in the previous section; we compute the trace of the surface stress as $\sigma_{22} + \sigma_{11} = 0.531$ eV/surface atom. Furthermore, we use a value for the ratio of the surface-stress components derived previously by Yang *et al.* [173]: $\sigma_{11}/\sigma_{22} = 1.6$. As a result, we obtain $\sigma^s_{11} = 0.327$ eV/surface atom and $\sigma^s_{22} = 0.204$ eV/surface atom.

The formation of misfit dislocations reduces the misfit strain in the film material from a bulk value of η^m_{ii} (no summation) by a^f_i/p_i. The misfit dislocations also introduce a sinusoidal variation in the strain on the surface but have no overall first-order effect on the surface energy due to the fact that the dislocation surface strain

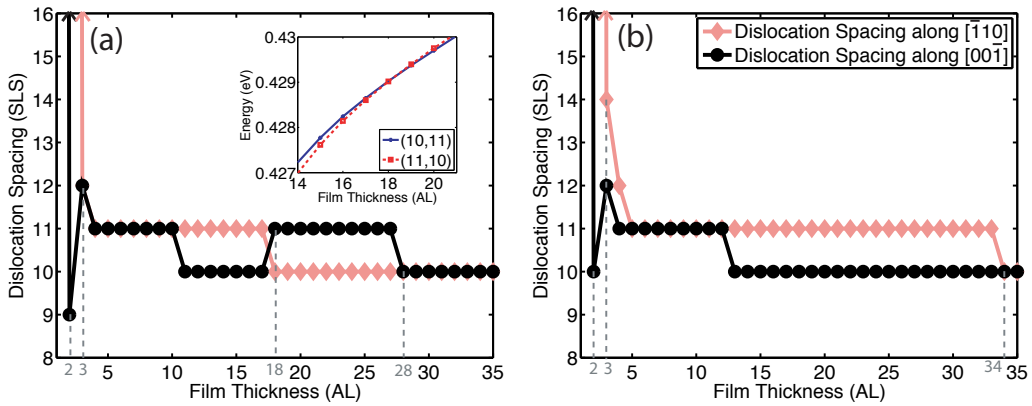

Figure 3.2: Minimum-energy dislocation spacing considering only the dislocation/deformation energy as a function of film thickness for the (a) Fe/Mo(110) and (b) Fe/W(110) systems. The dislocation spacing is normalized by the substrate lattice spacing (SLS). The film thickness is measured in atomic layers (AL). The arrow indicates that the dislocation spacing is infinitely large. The inset in (a) shows the dislocation/deformation energies of misfit dislocations with the spacings of 10 and 11 SLS versus 11 and 10 SLS along [$\bar{1}$10] and [00$\bar{1}$] directions, respectively, in the Fe/Mo system. The intersection between the two energy curves occurs between the film thickness of 17 and 18 AL.

averages to zero. If the energy at the reference deformation state is E^s_{pseudo}, the strain-dependent surface/interfacial energy as a function of film thickness, E^s, can be estimated as

$$E^s = E^s_{pseudo} - \sum_{i=1}^{2} \frac{\sigma^s_{ii} a^f_i}{p_i}. \tag{3.18}$$

It should be noted that the negative sign in front of the term $\sigma^s_{ii} a^f_i / p_i$ comes from the fact that for a given misfit strain, for example, η_{ii}, the film is subjected to a strain of $-\eta_{ii}$.

3.3 Results and Discussions

3.3.1 Dislocation Configuration

We perform the dislocation/deformation energy calculations for the Fe/Mo(110) and Fe/W(110) systems by taking a glide plane to be at the film/substrate interface. The energy is calculated as a function of the film thickness and dislocation spacing in both the $[00\bar{1}]$ and $[\bar{1}10]$ directions. For a given thickness, energies from different dislocation spacings in two directions, as well as the pseudomorphic configuration (no dislocation), are compared and the minimum-energy configurations of the misfit dislocations are shown in Fig. 3.2. For example, for the Fe/Mo system, the dislocation configuration of 10 substrate lattice spacing (SLS) along $[00\bar{1}]$ and 11 SLS along $[\bar{1}10]$ has the lowest energy for the film with the thickness of 11 atomic layer (AL). At the thickness of 1 AL for the Fe/Mo system and Fe/W system, the pseudomorphic configuration has the lowest energy as indicated by the dislocation spacings approaching infinity in all directions. Therefore, the results suggest that these thin films prefer to remain pseudomorphic; this is consistent with experimental observations [45, 46] and other theoretical calculations [161, 94].

For the film thickness of 2 AL for both systems, the lowest-energy configuration consists of a finite dislocation spacing along the $[00\bar{1}]$ direction (dislocation along the $[\bar{1}10]$ direction), while the spacing along the other direction remains at infinity. This type of dislocation array configuration relieves the misfit strain via plastic deformation along the $[00\bar{1}]$ direction and results in elastic relaxations in both $[\bar{1}10]$ and $[00\bar{1}]$ through the Poisson effect. Comparing the dislocation arrays in both $[\bar{1}10]$ and $[00\bar{1}]$ directions, the dislocation along the $[\bar{1}10]$ direction yields a relatively narrow dislocation core region, which results in a lower plastic deformation energy (E^p). Also by experimenting with different values of V (related to bond strength at the interface) and the shear modulus of the substrate material, μ^s, it is found that the disloca-

tion along the $[\bar{1}10]$ direction, associated with the relaxation along the shorter lattice spacing, is always energetically preferred. Experimentally such one-dimensional dislocation arrays are observed in both Fe/Mo and Fe/W systems, but they instead lie along the $[00\bar{1}]$ direction (finite spacing along the $[\bar{1}10]$ direction) [45, 46]. This discrepancy is likely due to other effects that are not accounted for in our model. For example, with the elastic anisotropy, if the lattice spacings are equal, the relaxation along the elastically soft direction would be preferred since the softer elastic response yields dislocations with narrower cores, reducing E_p.

For the film thickness of 3-27 AL for the Fe/Mo and 3-33 AL for the Fe/W systems, the dislocation spacing along both the $[\bar{1}10]$ and $[00\bar{1}]$ directions are finite, resulting in a dislocation network configuration. In this case, the homogeneous strain energy (E^h), which scales with volume, begins to dominate and the dislocation array formation in both directions is preferred. According to Eq. (3.1), the average residual strain is still not minimized at this stage, as the dislocation spacing in both directions are not 10 SLS. This is due to the contributions from E^e (dislocation elastic energy) and E^p (plastic deformation energy), which are reduced when the dislocations are further apart.

At the film thickness of 18 AL we observe a change of misfit configuration from 11 and 10 SLS to 10 and 11 SLS, along $[\bar{1}10]$ and $[00\bar{1}]$ directions, respectively, in the Fe/Mo system. The energies of these two dislocation configuration are shown in the inset in Fig. 3.2a where the intersection of two energy curves occurs between film thickness of 17 and 18 AL. The energy difference between these two configurations is less than 1% of the dislocation/deformation energy and therefore, either configuration may be observed experimentally. We do not, however, observe this change of dislocation configuration in the Fe/W system.

Lastly, beyond the film thickness of 28 AL for the Fe/Mo and 34 AL for the Fe/W systems, the contribution from E^h dominates and the dislocation spacings in both

directions are 10 SLS, which minimizes the average residual strain.

The difference in dislocation configurations of the two systems can be seen at the thickness of 2-5 AL, where the dislocation spacing in Fe/W system is larger. Also, the transition from a partially to fully relaxed dislocation network occurs at larger thicknesses in the Fe/W system than that in the Fe/Mo system. By comparing the energies with various combinations of V and μ^s values from the Fe/Mo and Fe/W systems, we found that these differences are mainly due of the higher shear resistance (proportional to τ_i) of the glide plane in the Fe/W system (or larger V value). This results in larger E^p and E^e relative to E^h. In addition, the larger shear modulus of the substrate also yields a larger sum of E^p and E^e compared with E^h, but to a lesser degree.

It should be noted that the assumption of the dislocation network formed by the $[\bar{1}10]$ and $[00\bar{1}]$ dislocation arrays would lead to an overestimation of the energies compared with that of the $[1\bar{1}1]/[11\bar{1}]$ network observed experimentally [45, 46, 158] since the effective restoring force that is exerted on the atom is overestimated. However, the transition of the dislocation configurations (from pseudomorphic film to the single dislocation array to the dislocation network) should be a general feature that is relatively insensitive to the exact value of τ_i.

3.3.2 Dislocation/Deformation Energy

Figure 3.3(a) shows the dislocation/deformation energy per area of a surface atom (= total dislocation/deformation energy divided by the total number of surface atoms) from the minimum-energy configurations shown in Fig. 3.2, plotted as a function of film thickness. The dislocation/deformation energies at the film thickness of 1 AL for both systems are equal because the 1 AL films in both systems remain pseudomorphic. Beyond the film thickness of 1 AL, the dislocation/deformation energies for both systems increase monotonically with the rate of increase becoming less as the film

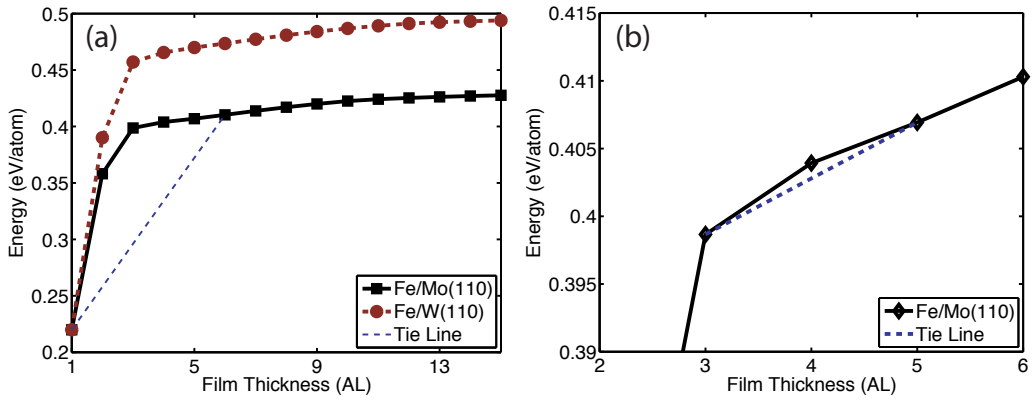

Figure 3.3: (a) Dislocation/deformation energy per surface atom (in eV) associated with the minimum-energy dislocation configurations as a function of film thickness. (b) Dislocation/deformation energy of the Fe/Mo system from the film thickness of 2-6 AL. The chord construction illustrates local instability of the film with the thickness of 4 AL.

becomes thicker. The magnitude of the energy of the Fe/W system is larger than that of the Fe/Mo system due to a larger value of V and a larger shear modulus of the substrate.

The figure shows that the dislocation/deformation energy exhibits a concave dependence on the film thickness, which indicates that the dislocation/deformation energetics favors the formation of thick regions and a monolayer. The driving force can also be identified by a chord construction. As an example, a chord is drawn from the value of the energy at the film thickness of 1 AL to 6 AL, which is indicated by the dash line in Fig. 3.3(a). Such a construction indicates that a flat film of, for instance, 3 AL thickness can lower its energy by forming regions of 1 AL and 6 AL, and the driving force can be quantified by the difference between the values on the energy curve and the value on the chord at 3 AL. Similarly, another chord can be constructed from the film thickness of 1 AL to other film thicknesses. Thus we find that dislocation/deformation energetics favors dewetting, i.e., the evolution of a thin film to a configuration involving thicker regions separated by a single-monolayer wetting layer.

Similar to the effect of the dislocation/deformation energetics, the contribution from the surface stress was proposed as the underlying energetics for the dewetting process [38]. By comparing the energetics of the dislocation/deformation from Fig. 3.3(a) with energetics of the surface stress from Ref. [38], we find that the driving force from the thickness dependence of the dislocation/deformation energy is more than one order of magnitude larger than that from the surface stress. Thus, the dislocation/deformation energetics should be expected to play a significant role in the dewetting process.

In this analysis, we ignore the energy penalty due to the presence of steps, which could play an important role when the thickness difference between regions is large. (This is typically the limiting factor against the growth of very tall islands.) In addition, we assume that the dislocation configuration is adjusted to its minimum-energy state for each thickness, which neglects the kinetic limitation as well as the dislocation interaction with the substrate step. Therefore, this analysis applies to conditions under which the annealing temperature and time is sufficient for the dislocation configuration to attain a minimum-energy state and under which the substrate terrace is wide enough to accommodate several periods of misfit dislocations.

3.3.3 Effect of Surface Stress

In this section, the effect of the surface stress is taken into account when determining the minimum-energy dislocation configuration. The resulting dislocation configuration is plotted in Fig. 3.4(a) for the Fe/Mo system. A pseudomorphic configuration for 1 AL film is preferred, similar to the result considering only the dislocation/deformation energy (Fig. 3.2(a)). However, the dislocation network forms with higher densities, or smaller dislocation spacings, than the dislocation configurations in Fig. 3.2(a). While the dislocation configuration is altered by the inclusion of the surface stress effect, we find that the overall dislocation/deformation energetics (not

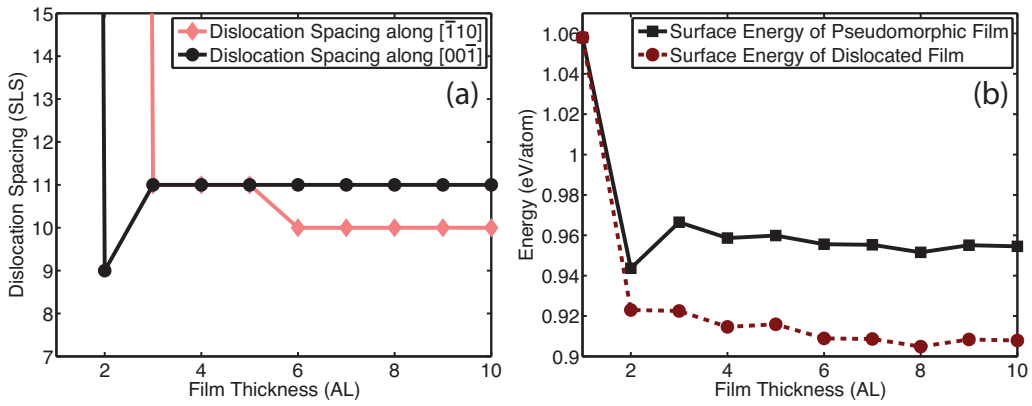

Figure 3.4: (a) Minimum-energy dislocation spacing, considering the surface stress effect for the Fe/Mo system. (b) Surface/interfacial energy (in eV/surface atom) of the Fe film on the Mo(110) substrate as a function of the film thickness. The solid line (square markers) denotes the surface/interfacial energy of the pseudomorphic film. The dash line (circular markers) denotes the strain-dependent surface/interfacial energy of the dislocated film.

shown) remains nearly the same as that shown in Fig. 3.3(a).

The effect of the surface stress on the dislocation spacing can be understood by considering the physical origin of the surface stress. The chemical bonds at the surface are different from the bonds inside the bulk region, which contributes to a different equilibrium spacing of the unconstrained surface atoms. To remain structurally coherent with the interior atoms, the surface atoms are strained by the bulk atoms. Typically, for metal surfaces, the equilibrium lattice constant of the surface atoms (i.e., the spacing that relaxes the surface atoms) is smaller than that of the bulk, and thus the surface atoms are in a tensile state [174]. Therefore, the compressive deformation on the surface will relax the surface atoms and thus reduce the surface energy. Since higher dislocation density introduces more compressive strain, E^s will favor higher dislocation density or lower dislocation spacings, in agreement with the lower dislocation spacings at the film thickness of 3 AL and 6-10 AL for the dislocation network.

For a Pt(111) film on Al(111) substrate, it has been found that misfit dislocations

form at a lower film thickness due to the surface stress [160]. While we observe denser dislocation configurations with surface stress, we do not observe a decrease in the critical thickness in the Fe/Mo system. This is likely due to a relatively high lattice mismatch in the Fe/Mo system, which controls overall behavior of misfit dislocations, and thus the surface stress does not play as important a role as that in the Pt(111)/Al(111) system.

Using the dislocation configuration from Fig. 3.4(a), we calculate the residual strain in the film and the correction to the surface/interfacial energy of the pseudomorphic film, E^s_{pseudo}, can be obtained. Figure 3.4(b) shows the strain-dependent surface/interfacial energy, E^s, plotted as a function of the film thickness from 1 to 10 AL. The value of E^s_{pseudo} is also plotted to demonstrate the difference between the two surface energies. At the film thickness of 1 AL, the strain-dependence correction to E^s_{pseudo} is zero since the film is pseudomorphic. Beyond the film thickness of 1 AL, the value of E^s is lower than the value of E^s_{pseudo} due to the formation of the misfit dislocations that reduce the homogeneous strain. Also, both surface energies reduce significantly between the film thickness of 1 AL and 2 AL, while at larger thicknesses they exhibit smaller variations with the film thickness.

It should be noted that the effect of the surface stress considered above depends on the amount of the average residual strain in the film, which is determined by the misfit dislocation configuration. This is different from the effect of the surface stress considered by McCarty *et al*[38], which depends on the thickness-dependent strain originating from a difference between the lattice spacing of the bulk layers and that of the "surface monolayer" of the film.

3.3.4 Dislocation/Deformation and Surface/Interfacial Energies

Figure 3.5(a) shows the combination of the strain-dependent surface/interfacial energy shown in Fig. 3.4(b) and the dislocation/deformation energy from the minimum-

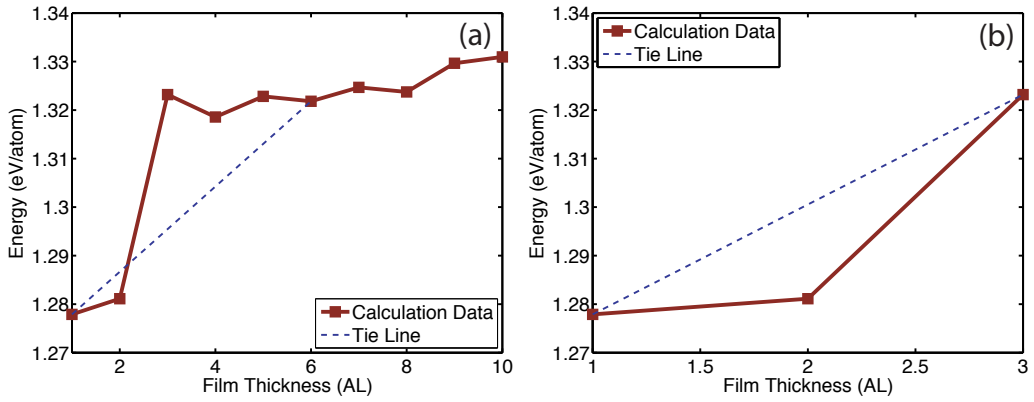

Figure 3.5: The combination of dislocation/deformation and surface/interfacial energies for the Fe/Mo system. (a) Film thickness from 1-10 AL. (b) Film thickness from 1-3 AL. The chord construction illustrates a metastability behavior of the thin film with the thickness of 2 AL.

energy dislocation configuration shown in Fig. 3.4(a) for the Fe/Mo system. The energy is plotted as a function of the film thickness up to 10 AL. The driving force for dewetting can be again identified by a chord construction, as shown in Fig. 3.5(a). Similar to the dislocation/deformation energy, at any given film thickness greater than 1 AL, a flat film can lower its energy by forming regions of 1 AL and a larger thickness. This concave dependence of the film thickness is inherited from the dislocation/deformation energy, not from the surface/interfacial energies, as seen in Fig. 3.3(a) and Fig. 3.4(b). In fact, by the same chord construction, the dependence of the surface/interfacial energy on film thickness is such that the separation of the film into a monolayer and a thicker region is not preferred. Therefore, the driving force from the combined dislocation/deformation and surface/interfacial energies (Fig. 3.5(a)) is a result of two competing effects in which the dislocation/deformation energy dominates.

3.3.4.1 Local Instability

In addition to the overall driving force for dewetting, local instability can be investigated to gain insight into the energetic pathway of the dewetting process. This

local instability refers to the instability of a flat film to small thickness perturbations. This can be examined by an instability criteria [38]. If $E(h_i)$ is the energy per area of a surface atom for the film thickness of i AL, the criteria for the film instability is

$$\begin{aligned} \frac{d^2E}{dh^2} &< 0 \quad \text{or} \\ E(h_{i+1}) + E(h_{i-1}) &< 2E(h_i). \end{aligned} \tag{3.19}$$

In other words, the instability occurs when the local shape of $E(h_i)$ is concave down. From Fig. 3.3(a), it is verified that the dislocation/deformation energy satisfies Eq. (3.19) for both Fe/Mo and Fe/W systems for the film thickness up to 5 AL. The driving force for local instability is larger for thinner films while beyond the film thickness of 5 AL, the dislocation/deformation energy is almost linear and $E(h_{i+1})$ + $E(h_{i-1})$ − $2E(h_i) \approx 0$. Figure 3.3(b) demonstrates that the shape of the plot of the dislocation/deformation energy is concave down locally, for example, at the film thickness of 4 AL by a chord construction. Therefore, we identify that, at least for the film of 1 - 5 AL, the energetics of the misfit dislocations and misfit strain favors instability of the surface to a small thickness perturbation. This is similar to the effect of the surface stress discussed in Ref. [38].

By applying the instability criteria in Eq. (3.19) to the energy curve in Fig. 3.5(a), we find that some thicknesses are unstable to thickness perturbations, while others exhibit local stability, or metastability. At the film thickness of 2 AL, there is a large driving force for local instability from the dislocation/deformation energy, which competes with a large driving force for metastability from the surface/interfacial energy. This results in a slight metastability at 2 AL. At a larger thickness, the driving force from the dislocation/deformation energy is reduced to a small value, and small variations in the surface/interfacial energy with the thickness can lead to a metastable behavior based on the combined energy. Due to the numerical errors inherent in

the first-principles calculations as well as the neglect of finite-temperature corrections and higher-order elastic effects (such as surface elastic constants), it is not possible to predict which of the thicker layers are most stable against thickness perturbations. However, the results do demonstrate local variations in the metastability of different film thicknesses, which arises purely from electronic effects associated with the thickness dependence of the surface/interfacial energy.

3.3.5 Applicability to Other Systems

Considering the dislocation/deformation energy, $E^h+E^e+E^p$, the thermodynamic driving force for dewetting should exist for other systems where misfit dislocation formation is a major strain-reduction mechanism. The dislocation/deformation energies of the pseudomorphic and fully relaxed film scale almost linearly with thickness because the dominating homogeneous strain energy (E^h) approximately scales with the volume. The slope of E^h also scales with the magnitude of the misfit strain. Since the formation of misfit dislocations reduces the misfit strain, the slope of the energy curve decreases with increasing film thickness, resulting in an overall concave-down dependence of the energy on thickness. The degree of the driving force depends largely on the lattice mismatch that determines the critical thickness as well as dislocation density. For systems with similar lattice mismatch, the difference in bond strength at the interface (proportional to τ_i and V) affects the magnitude of dislocation/deformation energy to a greater degree than the difference in elastic constants, as seen in comparison between Fe/Mo and Fe/W systems. The surface energy, on the other hand, depends on the specific electronic structure of each material systems and, as shown in these specific systems, changes the metastability of the film at small thicknesses.

3.4 Chapter Summary

We have developed a multiple-scale model for a thin film epitaxial system and investigated the stability of single-crystal, internal-defect-free Fe films on Mo(110) and W(110) by considering the energy contributions from the interfacial misfit dislocations, misfit strain, film surface and interface. The misfit dislocation model is based on the continuum-level Peierls-Nabarro formulation, combined with the corrugation potential calculated from first-principles electronic density-functional-theory calculations. The energetics was then examined along with the first-principles calculated surface/interfacial energy. Our model is able to capture the transition of the initially thin pseudomorphic (no dislocation) film to a partially relaxed film (dislocation array) and finally to a fully relaxed film (dislocation network), which is consistent with the experimental observations in both Fe/Mo and Fe/W systems. Combining the energetics of the misfit strain, misfit dislocations, film surface and interface, we have identified that there is a net driving force for solid-state dewetting of a single crystal, internal-defect-free film in which other dewetting mechanisms mediated by grain boundaries or impurities are absent. The results also demonstrate how non-monotonic dependencies of the surface/interfacial energy on film thickness from the electronic effects can give rise to the metastability of flat films with certain thicknesses.

CHAPTER IV

Modeling Classical Density Functional Theory and the Phase-Field Crystal Method using a Rational Function to Describe the Two-body Direct Correlation Function

4.1 Overview

In this chapter, we use the RFF method to examine the importance of short-wavelength contributions in the two-body DCF that is used in CDFT. Our studies on iron (Fe) show that the short-wavelength contributions influence the thermodynamic properties not only quantitatively, but also qualitatively. For example, the phase stability of the face-centered-cubic (FCC) structure has a strong dependence on the short-wavelength contributions in the DCF, which is typically not accurately accounted for in PFC studies. We also show that, within the framework of the RFF method, it is possible to empirically parameterize the two-body DCF to increase computational efficiency of CDFT while retaining the accuracy of most predictions of the thermodynamic properties in comparison to those of CDFT with the full two-body DCF. We also demonstrate that the RFF can be used to improve the representation of the two-body DCF in the PFC model.

In Section 4.2, we present the CDFT and PFC equations that will be used throughout this chapter and discuss the motivation for our numerical techniques. We then propose the RFF method in Section 4.3. The importance of the short-wavelength contributions is examined in Section 4.4, and the empirical parameterization of the DCF is discussed in Section 4.5. The RFF method is then applied to the PFC formulation in Section 4.6, followed by a discussion of the real-space reformulation of the RFF method in Section 4.7. In Section 4.8, we compare Fourier-space and real-space implementations. Lastly, we conclude the chapter with a summary.

4.2 Background and Motivation

4.2.1 Classical Density Function Theory of Freezing

As presented in Chapter II, the free energy of the CDFT of freezing can be expressed as [67]

$$\begin{aligned}\beta\mathcal{F}\big(\rho(\mathbf{r})\big) &= \beta\mathcal{F}(\rho_0) + \beta\mu_0 \int d\mathbf{r}\Delta\rho(\mathbf{r}) + \int d\mathbf{r}\left\{\rho(\mathbf{r})\ln\left[\frac{\rho(\mathbf{r})}{\rho_0}\right] - \Delta\rho(\mathbf{r})\right\} \\ &\quad -\frac{1}{2}\int\int d\mathbf{r}_1 d\mathbf{r}_2 \Delta\rho(\mathbf{r}_1)c^{(2)}(\mathbf{r}_1,\mathbf{r}_2;[\rho_0])\Delta\rho(\mathbf{r}_2), \qquad (4.1)\end{aligned}$$

where μ_0 is the chemical potential of the reference state, $\Delta\rho(\mathbf{r}) = \rho(\mathbf{r}) - \rho_0$, and the function $c^{(2)}(\mathbf{r}_1,\mathbf{r}_2;[\rho_0])$ is the two-body DCF of the reference uniform density state. We note that the formation of a solid phase occurs when the equilibrium density profile is a periodic non-uniform function with symmetry corresponding to a crystal lattice. By introducing a dimensionless one-body probability density,

$$n(\mathbf{r}) = \frac{\rho(\mathbf{r}) - \rho_0}{\rho_0}, \qquad (4.2)$$

we write the scaled dimensionless energy as

$$\Delta\tilde{\mathcal{F}}_{CDFT}\big(n(\mathbf{r})\big) = \frac{\mathcal{F}\big(\rho(\mathbf{r})\big) - \mathcal{F}(\rho_0)}{k_B T \rho_0} = \int d\mathbf{r}\,\{[1+n(\mathbf{r})]\ln[1+n(\mathbf{r})] - n(\mathbf{r})\} - \frac{\rho_0}{2}\int d\mathbf{r}\int d\mathbf{r}'\left\{n(\mathbf{r})c^{(2)}(|\mathbf{r}-\mathbf{r}'|)n(\mathbf{r}')\right\}, \quad (4.3)$$

where we set the chemical potential of the reference state to be zero. It is assumed that $c^{(2)}$ is isotropic.

The form of the two-body DCF plays an important role in determining the equilibrium density profile and, in turn, the numerical efficiency of the model. To illustrate, let us consider a two-body DCF in Fourier space, $\hat{c}^{(2)}(k)$, where k is the magnitude of the Fourier-space vector, $k = |\mathbf{k}|$. The equilibrium profile, $n(\mathbf{r})$, can be expressed as a summation of density waves:

$$n(\mathbf{r}) = \bar{n}\left(1 + \sum_j u_j e^{i\mathbf{G}_j\cdot\mathbf{r}}\right), \quad (4.4)$$

where $\bar{n}$ is the average density, $\mathbf{G}_j$ is a linear combination of the primitive reciprocal lattice vectors, and u_j is the corresponding density wave amplitude. The j^{th} term in the above expansion will decrease the excess contribution to the free energy if $\hat{c}^{(2)}(|\mathbf{G}_j|)$ is positive (indicating correlation); in such a case, the density wave mode with the wave vector $\mathbf{G}_j$ is favored. On the other hand, the j^{th} term in the expansion above will increase the excess contribution to the free energy if $\hat{c}^{(2)}(|\mathbf{G}_j|)$ is negative (indicating anti-correlation), which tends to suppress that density wave mode.

Typical two-body DCFs in Fourier space have oscillations that contain positive values even at large k, which imply the presence of short-wavelength correlations in these systems. While these effects decrease with increasing k, they are nevertheless important. These short-wavelength correlations give rise to sharp peaks in the atomic probability density, which require a large number of basis functions or a very fine

computational grid to attain a sufficiently accurate numerical representation. These computational limitations are alleviated in the PFC method, which is discussed below.

4.2.2 Phase-Field Crystal Method

As presented in Chapter II, the free energy functional of the PFC method can be obtained from approximating the CDFT free energy [76]. First, the ideal contribution in Eq. (4.3) is approximated by its Taylor expansion:

$$(1+n(\mathbf{r}))\ln(1+n(\mathbf{r}))-n(\mathbf{r}) \approx \frac{1}{2}n(\mathbf{r})^2 - \frac{a_t}{6}n(\mathbf{r})^3 + \frac{b_t}{12}n(\mathbf{r})^4 \ , \tag{4.5}$$

with $a_t = b_t = 1$ in the original formulation of the PFC method. However, in a later work [121], a_t and b_t have been used as empirical parameters to fit specific properties of liquid and solid. The second approximation constitutes a fourth-order fit (4P) of the two-body DCF in Fourier space as

$$\hat{C}^{(2)}_{4P}(k) \equiv \rho_0 \hat{c}^{(2)}_{4P}(k) = \mathcal{C}_0 + \mathcal{C}_2 k^2 + \mathcal{C}_4 k^4 \ , \tag{4.6}$$

where the constants $\mathcal{C}_0$, $\mathcal{C}_2$, and $\mathcal{C}_4$ are fitting coefficients. These approximations yield the PFC free energy functional of the form:

$$\Delta\tilde{\mathcal{F}}_{4P}\big(n(\mathbf{r})\big) = \int d\mathbf{r}\left[n(\mathbf{r})\frac{1-\mathcal{C}_0+\mathcal{C}_2\nabla^2-\mathcal{C}_4\nabla^4}{2}n(\mathbf{r}) - \frac{a_t}{6}n(\mathbf{r})^3 + \frac{b_t}{12}n(\mathbf{r})^4\right] \ . \tag{4.7}$$

Recently, an expansion up to the eighth order was proposed in order to better approximate the two-body DCF [121]:

$$\hat{C}^{(2)}_{8P}(k) \equiv \rho_0 \hat{c}^{(2)}_{8P}(k) \ = \ \mathcal{C}_m - \Gamma\left(\frac{k_m^2-k^2}{k_m^2}\right)^2 - E_B\left(\frac{k_m^2-k^2}{k_m^2}\right)^4 , \tag{4.8}$$

where

$$\Gamma = -\frac{k_m^2 \mathcal{C}_c}{8}, \quad E_B = \mathcal{C}_m - \mathcal{C}_0 - \Gamma, \tag{4.9}$$

and k_m, $\mathcal{C}_0$, $\mathcal{C}_m$, and $\mathcal{C}_c$ are fitting constants. We denote this approximation as the eighth-order fit (8P). The corresponding free energy is

$$\begin{aligned} \Delta\tilde{\mathcal{F}}_{8P}\big(n(\mathbf{r})\big) &= \int d\mathbf{r} \Bigg[\frac{n(\mathbf{r})}{2} \left(1 - \mathcal{C}_m + \Gamma \left(\frac{k_m^2 + \nabla^2}{k_m^2} \right)^2 + E_B \left(\frac{k_m^2 + \nabla^2}{k_m^2} \right)^4 \right) n(\mathbf{r}) \\ &\quad - \frac{a_t}{6} n(\mathbf{r})^3 + \frac{b_t}{12} n(\mathbf{r})^4 \Bigg]. \end{aligned} \tag{4.10}$$

The fitting parameters in Eqs. (4.6) and (4.8) are chosen so that these fits accurately describe the two-body DCF up to the first peak [153, 121], and are employed in the present work. Compared to the 4P, the 8P in Eq. (4.8) provides an additional fitting parameter to better fit the DCF. Beyond the first peak, the values of the fits for both 4P and 8P become increasingly negative as k increases. These large anti-correlations at short wavelengths results in the high-frequency density waves being energetically unfavorable, thus resulting in nonlocalized, smooth equilibrium density profiles and in turn improved computational efficiency.

The dynamics of the PFC method is given by:

$$\frac{\partial n(\mathbf{r}, \tau)}{\partial \tau} = \nabla^2 \frac{\delta \Delta\tilde{\mathcal{F}}_{PFC}[n(\mathbf{r}, \tau)]}{\delta n(\mathbf{r}, \tau)} \ , \tag{4.11}$$

where the subscript PFC denotes the free energy given in Eq. (4.7) or Eq. (4.10), and τ is time. This equation can be obtained from mass conservation where the flux is driven by the gradient of the chemical potential [64], which is a variational derivative of the free energy with respect to the atomic probability density.

A polynomial approximation of the two-body DCF is limited in the ability to

represent the DCF accurately beyond the first peak. In order to improve the predictive capability of the PFC method relative to CDFT, it may be important to consider the short-wavelength correlations beyond the first peak. To this end, we propose an alternative method for representing the two-body DCF using a ratio of polynomials in the next section. We subsequently demonstrate that such an approach addresses the limitation in the predictive capability of the PFC method and the computational demand of CDFT, as well as enables a real-space reformulation of these methods.

4.3 Rational Function Fit

In order to address the aforementioned issues, we introduce a new method in which a rational function—a ratio of polynomials—is used to fit the two-body DCF in Fourier space. The resulting rational function can be decomposed into a summation of partial fractions as

$$\hat{C}^{(2)}_{RFF}(k) \equiv \rho_0 \hat{c}^{(2)}_{RFF}(k) = \sum_j \left[\frac{A_j}{k^2 + \alpha_j} + \frac{A_j^*}{k^2 + \alpha_j^*} \right], \tag{4.12}$$

where A_j and α_j are fitting coefficients which are generally complex numbers and the asterisk denotes a complex conjugate. We refer to this approach as the rational function fit (RFF) method, and denote the rational function fit comprising m partial fraction terms as the mR. The above fit accurately captures the oscillatory behavior of the two-body DCF and satisfies the short-wavelength limit, i.e., $\hat{C}^{(2)}_{RFF}(k) = 0$ as $k \to \infty$. The coefficients A_j and α_j can be determined from curve fitting algorithms, and we use the Curve Fitting Toolbox (version 2.2) in the Matlab software (version 7.10.0.499) in the present work. We find that odd numbers of partial fractions, which results in one pair of coefficients, A_j and α_j, being real values, are better suited for the given problem. Therefore, we present only these cases.

In Sections 4.4, 4.5 and 4.6, we demonstrate how the RFF can be used to address

the issues of high computational cost in CDFT and limited predictive capability of the PFC method. To this end, we consider the two-body DCF of Fe, which is shown as a solid line in Fig. 4.1. This data, provided by Wu [175], was obtained from embedded-atom-method molecular dynamics (EAM-MD) simulations described in Ref. [154]. We will subsequently denote this data as $\hat{c}^{(2)}_{MD}(k)$, or $\hat{C}^{(2)}_{MD}(k) \equiv \rho_0 \hat{c}^{(2)}_{MD}(k)$. This data was obtained from a simulation at a temperature of $T = 1772$ K and a density of $\rho_0 = 0.0801$ Å^{-3}, which is used as the reference density for normalizing the governing equations. Since MD simulations cannot provide the long-wavelength limit of the two-body DCF due to the restricted size of simulation domains, this limit was approximated from experimental data to be $\hat{C}^{(2)}_{MD}(0) \approx -49$ [121].

4.4 Examining the Role of Short-Wavelength Contributions of the Two-Body Direct Correlation Function

In this section, we examine the importance of the short-wavelength contributions in the two-body DCF to the thermodynamic properties computed using the CDFT free energy. We employ the RFF method that enables us to systematically control the short-wavelength contributions. We first describe various fits of $\hat{C}^{(2)}_{MD}(k)$ employed in this work followed by the procedures used to calculate the relevant thermodynamic quantities. We subsequently present the results of the calculations and discuss our findings.

4.4.1 The Rational Function Fits of the Two-Body Direct Correlation Function of Fe

We show the various fits of $\hat{C}^{(2)}_{MD}(k)$ using the RFFs in Figs. 4.1(a) and 4.1(b). Figure 4.1(a) shows that all 4 RFFs satisfy the following two limits: $\hat{C}^{(2)}_{RFF}(0) = -49$ and $\hat{C}^{(2)}_{RFF}(\infty) \to 0$. The difference between these 4 RFFs is the number of the partial

fraction terms in the RFF, which determines the number of peaks of $\hat{C}^{(2)}_{MD}(k)$ that are captured (see Fig. 4.1(b)). The 3-term RFF (the RFF that can be decomposed into three partial fraction terms), denoted by 3R, captures $\hat{C}^{(2)}_{MD}(k)$ accurately up to the first peak, while the 5R captures up to the second peak. The 7R and the 9R capture up to the third and fourth peaks, respectively. In this manner, we systematically improve the accuracy of the representation of the short-wavelength contributions in the two-body DCF, making it possible to study their effect on the thermodynamic properties.

In Fig. 4.1(c), we show the plots of the 8P and the 4P, whose coefficients are chosen to describe $\hat{C}^{(2)}_{MD}(k)$ up to its first peak [153, 121]. Both fits become increasingly negative beyond the first peak, approaching negative infinity as $k \to \infty$. We further note that an additional fitting parameter in the 8P (compared with that of the 4P) allows the 8P to capture the desired long-wavelength limit, $\hat{C}^{(2)}_{8P}(0) = -49$, whereas the 4P does not. To make consistent comparisons with RFF results, we will only use the thermodynamic properties computed from using the 8P of $\hat{C}^{(2)}_{MD}(k)$.

4.4.2 Procedures to Calculate Solid-Liquid Properties

We consider the following thermodynamic properties: phase stability of body-centered-cubic (BCC) and face-centered-cubic (FCC) solids; BCC solid and liquid densities at solid-liquid coexistence; and solid-liquid interfacial free energies. These properties are obtained from analyzing equilibrium free energies of bulk solid, bulk liquid, and coexisting solid-liquid phase. The free energy of the bulk liquid can be calculated analytically due to the uniformity of the bulk liquid-density profile, while the free energies of the other systems are obtained from numerical calculations of the equilibrium density profiles.

We use two methods to determine the equilibrium density profile. The first method is a numerical relaxation based on globally conserved dynamics [176], also known as

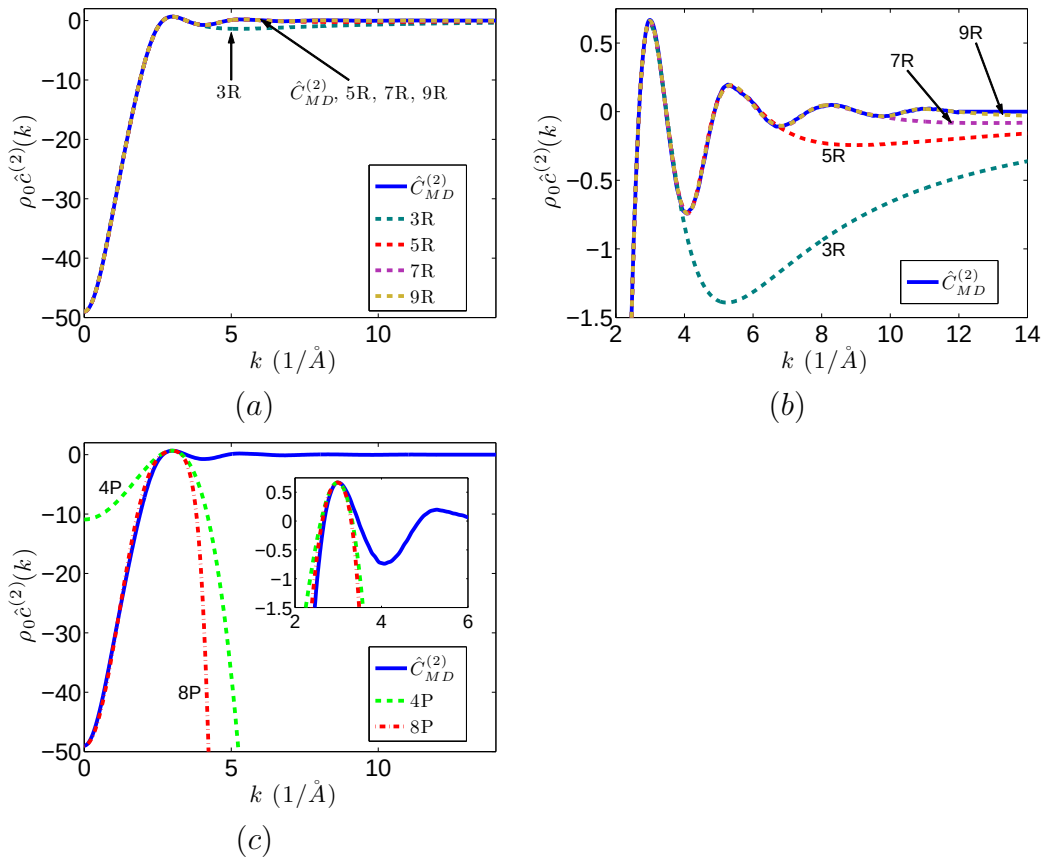

Figure 4.1: The different fits to the embedded-atom-method molecular dynamics (EAM-MD) data, $\hat{C}^{(2)}_{MD}$ [175]. (a) The rational function fits (RFFs) with different number of terms. (b) A magnified section of (a). (c) The fourth-order fit (4P) and the eighth-order fit (8P) [153, 121].

the conserved Allen-Cahn dynamics:

$$\frac{\partial n(\mathbf{r},\tau)}{\partial \tau} = -\frac{\delta \Delta\tilde{\mathcal{F}}_{CDFT}\big(n(\mathbf{r},\tau)\big)}{\delta n(\mathbf{r},\tau)} + \frac{1}{V}\int d\mathbf{r}\frac{\delta \Delta\tilde{\mathcal{F}}_{CDFT}\big(n(\mathbf{r},\tau)\big)}{\delta n(\mathbf{r},\tau)}, \tag{4.13}$$

where V is the volume of the system. This method is used in all cases except for the calculations of the phase stability of the FCC solid. The second method is a semi-analytical method where we approximate the equilibrium density profile constructed from non-overlapping Gaussian functions centered at the lattice sites [63]. We then minimize the free energy with respect to parameters that control the Gaussian peak height/width and unit-cell size. The details of the Gaussian approximation are dis-

cussed in Appendix A. This relaxation method is employed for the FCC solid as the density profiles are sharply peaked around the lattice sites, making full numerical relaxation too expensive.

Following the procedure in Ref. [121], we determine the solid-liquid coexistence regions from a common-tangent construction of the free energy density curves[1]. The solid-liquid interfacial free energy, γ, is evaluated by constructing a long slab whose size is one unit-cell in the plane of the interface and 64 unit-cell long in the direction perpendicular to the interface. One half of the slab is initialized as the bulk solid at the solid density at solid-liquid coexistence and the other half is initialized as the bulk liquid at the liquid density at the solid-liquid coexistence. The slab is then relaxed numerically using Eq. (4.13) with periodic boundary conditions, and γ is calculated by subtracting out free energies of the bulk phases.

4.4.3 Results and Discussions

The resulting thermodynamic properties from the CDFT simulations with the different fits to $\hat{C}^{(2)}_{MD}(k)$ are shown in Table 4.1. Figure 4.2 shows the free energy density curves of the liquid and the BCC solids, which are used to calculate the densities at the solid-liquid coexistence and volume expansion during melting. The integrated density profiles per unit area along the direction normal to (110) plane are shown in Fig. 4.3 and the density profiles on the (100) crystal plane of the BCC solids at the solid-liquid coexistence are shown in Fig. 4.4.

Table 4.1 also shows the stability of the FCC solids (bottom row) from the simu-

[1]In Ref. [121], the solid free energy curve is obtained by minimizing the free energy density with respect to the lattice spacing for a prescribed solid average-density. However, we find that the evaluation of the energy-minimizing lattice spacing for each prescribed density is not necessary because the energy-minimizing lattice spacing is only weakly dependent on the average density. In particular, we find that, by using $\hat{C}^{(2)}_{MD}(k)$, the energy-minimizing lattice spacing over the range of $(\rho-\rho_0)/\rho_0$ from 0.1 to 0.3 only varies by 0.01%. The error introduced to the energy density by using the same lattice spacing for the density range of interest is only on the order of 0.1%. Therefore, we only calculate the energy-minimizing lattice spacing once for each free energy curve, making the evaluation process significantly faster.

lations using the RFFs and the 8P. The stable behavior (denoted by "S" in Table 4.1) of the FCC solid is shown in Fig. 4.5(a) for the $\hat{C}^{(2)}_{MD}(k)$ CDFT simulation, where the FCC solid attains stability at large densities. This behavior is captured by the 7R and 9R CDFT simulations (see Figs. 4.5(c) and 4.5(b), respectively). However, the 5R CDFT simulation shows a metastable behavior (denoted by "MS" in Table 4.1) of the FCC phase, where the FCC phase has energy minima that are higher than the energy minima of the BCC phase. This metastable behavior can be seen from the free energy curves of the FCC and BCC solids shown in Fig. 4.5(d). We further note that the FCC phase is not stable (denoted by "NS" in Table 4.1) for the 3R and the 8P of the two-body DCF.

Comparing results from the 3R CDFT simulations with those of the 8P, we do not find a significant difference in the solid and liquid properties as well as in the density profiles. We note that these two fits capture the correlations accurately up to the first peak in the two-body DCF, but do not account for the shorter wavelength correlations. The more accurate asymptotic behavior of the 3R does not substantially improve the accuracy of the computed thermodynamic properties in comparison to the 8P. However, the 5R to 9R CDFT simulations show progressively improved accuracy in the predictions (see Table 4.1), with the most significant improvement between the 3R and the 5R. We note that the 5R accurately represents the correlations up to the second peak in the two-body DCF. Further, the 7R and the 9R accurately represent the correlations up to the third and fourth peaks, respectively. Although the accuracy of the thermodynamic properties improves between the 7R and the 9R, the extent of the improvement is not as significant as that seen between the 3R to the 5R, and the 5R to the 7R. We attribute this observation to the fact that the amplitude of the correlations in the two-body DCF asymptotically decays, and therefore the role of increasingly shorter wavelength correlations to the thermodynamic properties is progressively less significant. Nevertheless, the 5R does not predict the stability of

the FCC phase, suggesting that the correlations up to the third peak in the two-body DCF appear to be important for phase stability. Finally, by noting that the predictions of the 3R does not significantly differ from those of the 8P, we believe that the thermodynamic properties are relatively insensitive to the anti-correlations beyond the first peak.

In this section, the short-wavelength correlations are shown to be important even for a qualitative prediction of thermodynamic properties. Therefore, the computational demand of CDFT, arising from the sharp localized peaks in the density profiles, cannot be alleviated by simply suppressing the short-wavelength correlations (as done in most PFC methods) without sacrificing the predictive capability of the model considerably. We now propose an empirical parameterization of the two-body DCF as a RFF, which seeks to improve the predictive capability using fewer terms in the RFF.

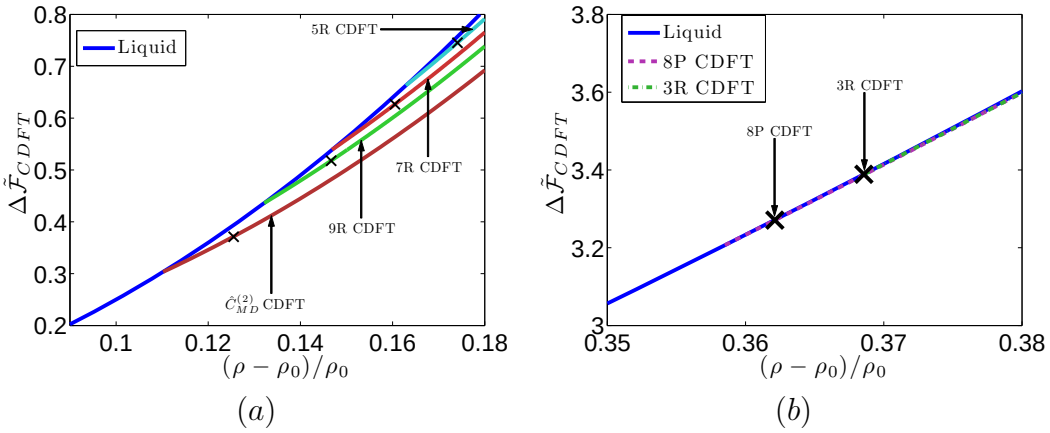

Figure 4.2: The normalized free energies per unit volume of the BCC solids corresponding to different fits of the EAM-MD data. The blue-solid line denotes the liquid free energy density curve whereas the other lines denote the solid free energy density curves. (a) Free energies of the BCC solids from the CDFT simulations using the EAM-MD data, the 9R, the 7R and the 5R. The cross signs at the solid curves denote the solid densities at the solid-liquid coexistence. (b) Free energies of the BCC solids from the CDFT simulations using the 8P and the 3R. The two cross signs show the solid densities at the solid-liquid coexistence.

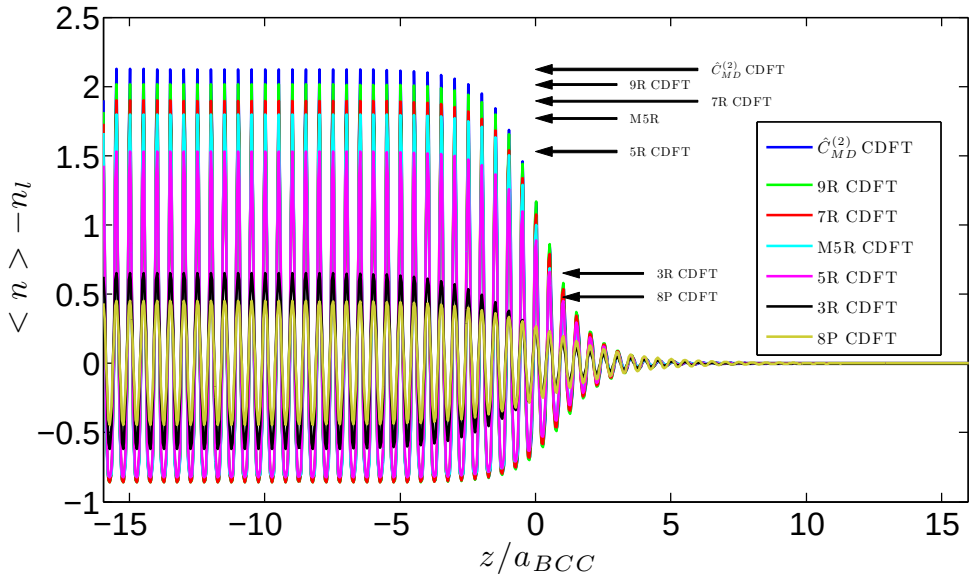

Figure 4.3: The BCC solid-liquid density profiles along the direction normal to the (110) plane (z-axis), where a_{BCC} is the lattice spacing. Here, $\langle n \rangle = A^{-1} \int \int n(x, y, z) dxdy$, where A is the surface area and n_l is the normalized liquid density at the solid-liquid coexistence. The arrows indicate the amplitude of the fluctuation in the bulk solid region of the density profiles.

Quantity	$\hat{C}^{(2)}_{MD}$ CDFT	9R CDFT	7R CDFT	5R CDFT	3R CDFT	8P CDFT
Liquid density (Å^{-3})	0.0877	0.0896	0.0909	0.0923	0.109	0.109
(% Difference from $\hat{C}^{(2)}_{MD}$ CDFT)		(2.1%)	(3.6%)	(5.2%)	(24%)	(24%)
Solid density (Å^{-3})	0.0902	0.0918	0.0930	0.0940	0.110	0.109
(% Difference from $\hat{C}^{(2)}_{MD}$ CDFT)		(1.9%)	(3.1%)	(4.3%)	(22%)	(21%)
Expansion in melting (Å^3/atom)	0.304	0.271	0.249	0.198	0.0373	0.0211
γ_{100} (erg/cm^2)	88.7	84.3	81.3	67.4	13.7	6.53
γ_{110} (erg/cm^2)	86.6	81.9	79.0	65.5	13.5	6.37
FCC crystal	S	S	S	MS	NS	NS

Table 4.1: The comparison of the liquid and solid properties computed from the CDFT simulations using different fits of the EAM-MD data, $\hat{C}^{(2)}_{MD}(k)$. The liquid and BCC-solid densities shown are at solid-liquid coexistence, and the expansion in melting is for the BCC solid. The abbreviations S, MS, and NS denote "stable," "metastable," and "not stable," respectively (see text). The data are rounded to three significant digits. The comparison between the predictions from the CDFT simulations using $\hat{C}^{(2)}_{MD}(k)$ and those from MD and experimental data can be found in Ref. [121] and therefore is not included.

4.5 Empirical Parametrization of the Two-Body Direct Correlation Function

As seen in the previous study, there is a significant improvement in the accuracy of the predicted thermodynamic properties upon resolving the second peak in the two-body DCF (as seen in the differences between the 3R and 5R CDFT results). Thus, we seek to construct a parameterization of the two-body DCF that yields the accurate thermodynamic properties of the liquid and solid phases, while providing smoother atomic density profiles, by using a RFF that represents the correlations up to the second peak. We begin with the 5R and systematically vary the value of the function at both peaks, keeping the curvature values and the locations of the peaks similar to those from $\hat{C}^{(2)}_{MD}(k)$. The locations of the peaks are fixed to maintain the

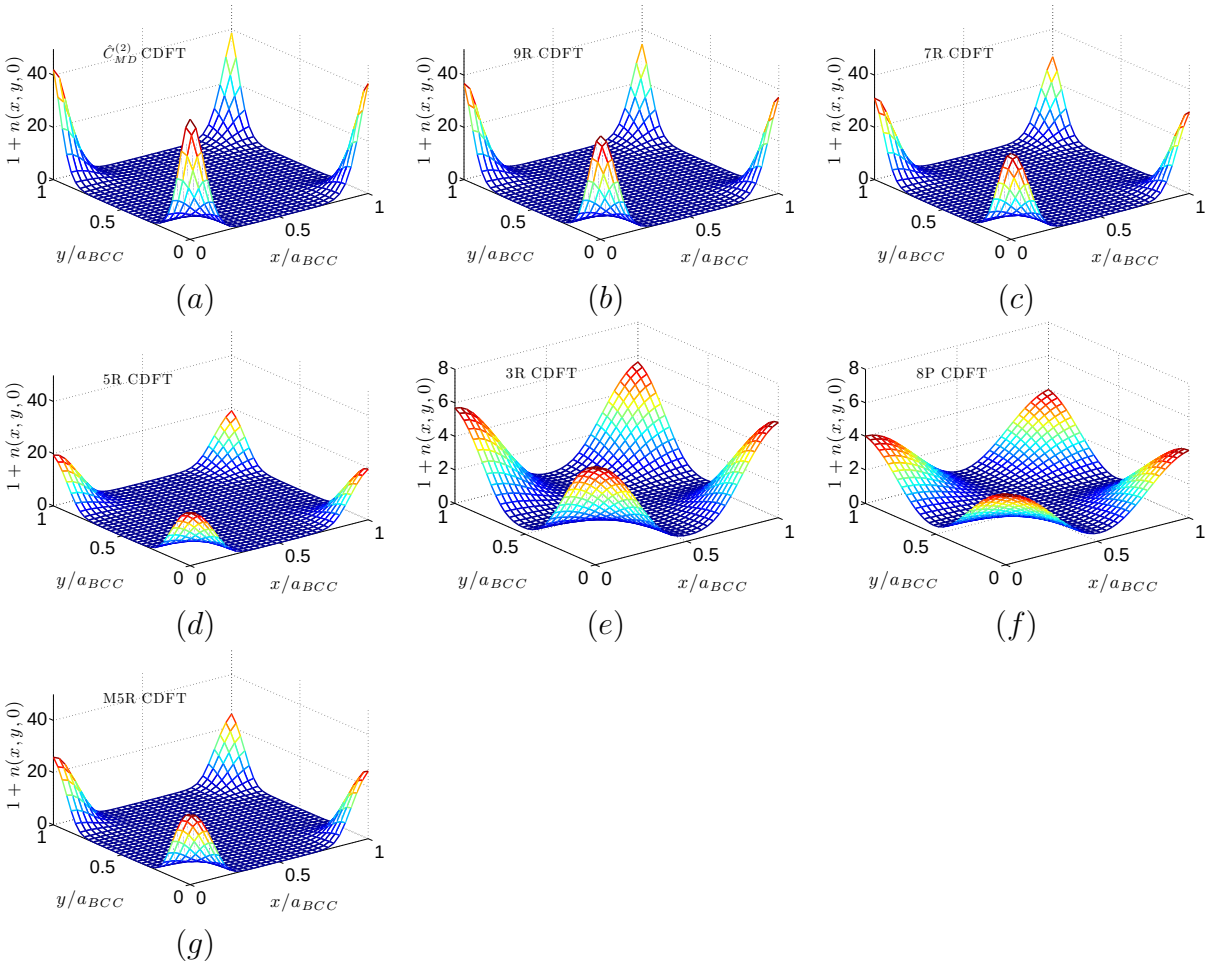

Figure 4.4: The density profiles on the (100) crystal plane of the BCC solids at the solid-liquid coexistence, where a_{BCC} is the lattice spacing. It should be noted that the vertical scales of (e) and (f) are different from the others.

lattice constants of the solid crystal, and the curvature values of the peaks are held constant to retain the interfacial properties of the liquid-solid interface, as suggested by Ref. [154].

In terms of implementation, an analytical expression of the modified 5R, M5R, is manually constructed from a spline interpolation of discrete data points. We then employ the semi-analytical method to determine the fit that yields similar solid free energies to the simulations using $\hat{C}^{(2)}_{MD}$ at the solid density at the solid-liquid coexistence; this procedure allows us to quickly experiment with a large number of fits.

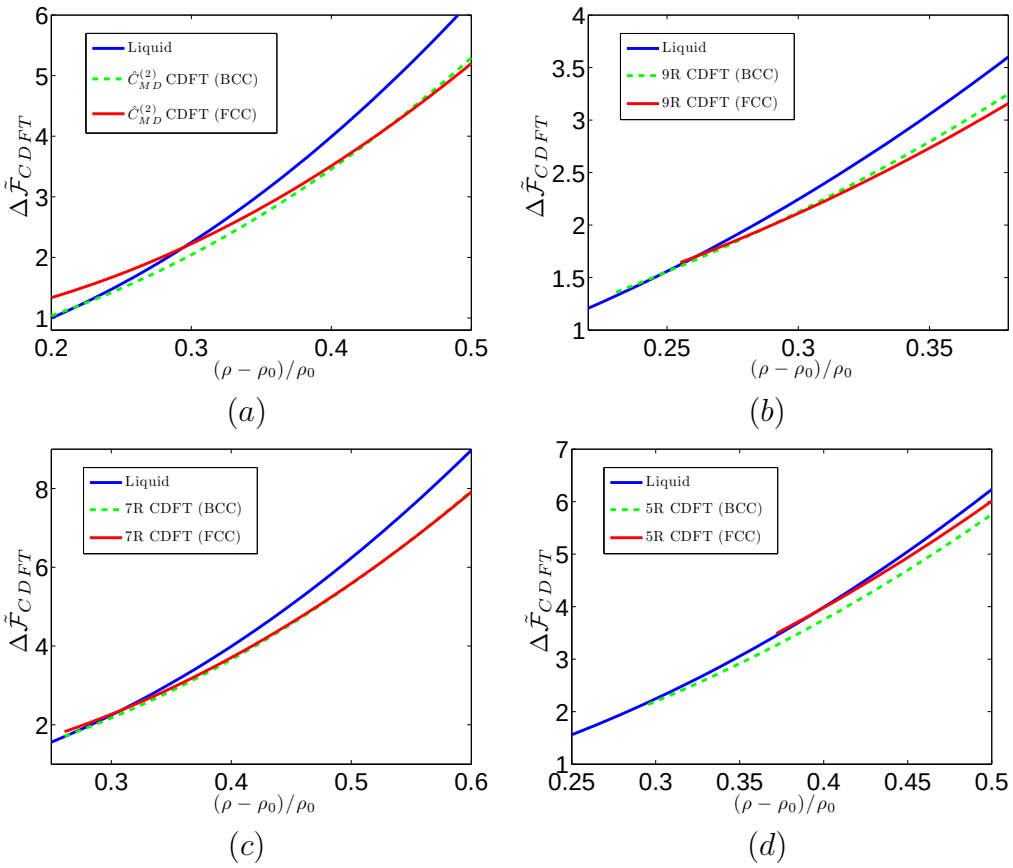

Figure 4.5: The normalized free energies per unit volume of the BCC and FCC solids from the CDFT simulations using the EAM-MD data, the 9R, the 7R, and the 5R. The 5R-BCC and 5R-FCC curves do not intersect. The solid free energies are evaluated from the semi-analytical method described in Section 4.4.2. The blue solid curves denote the liquid free energy.

Subsequently, we fit the data with the RFF and use the numerical method to verify the fit.

The M5R, shown in Fig. 4.6(a), is similar to the 5R except for a slightly higher value of the function at the second peak. The corresponding free energy of the BCC solid from the M5R CDFT simulations, shown in Fig. 4.6(b), is in good agreement with those of $\hat{C}^{(2)}_{MD}(k)$. The slightly higher value at the second peak results in the density profile from the M5R CDFT simulations being more localized than those from the 5R. This is apparent from the higher amplitudes of density peaks at the BCC lattice sites shown in Fig. 4.4, and from the integrated density profile per unit area

shown in Fig. 4.3. The liquid and solid properties of the BCC phase from the M5R CDFT simulations are tabulated in Table 4.2, and are in good agreement with the results from the CDFT simulations using $\hat{C}^{(2)}_{MD}(k)$. Further, we note that most of the thermodynamic properties computed from the M5R CDFT simulations are more accurate than those computed from the 9R. However, the stability of the FCC phase is not predicted by the M5R, further emphasizing the role of correlations corresponding to the third peak in determining the FCC phase stability of Fe (see also a footnote[2]).

As demonstrated from the results, the M5R predicts most thermodynamic properties with greater accuracy than the 9R. As seen in Fig. 4.4, the density profiles from the M5R CDFT simulations are considerably smoother than those of the 9R, which leads to the improved computational efficiency of the CDFT simulations.

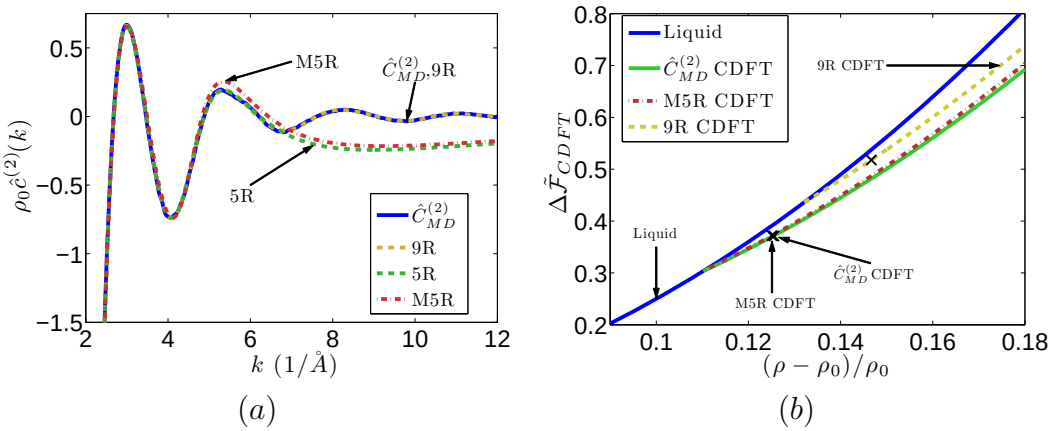

Figure 4.6: (a) The comparison between the 5R and the M5R. The two fits are similar except for the second peak of the M5R being slightly higher. The solid line denotes the EAM-MD data. (b) The comparison between the normalized BCC solid free energy densities from the CDFT simulations using the EAM-MD data, the 9R, and the M5R. The cross signs indicate the solid densities at solid-liquid coexistence. The cross signs on the M5R and EAM-MD free energy curves nearly coincide at the current graphical scale.

[2]We note that the MD simulation employing the EAM potential used to generate $\hat{C}^{(2)}_{MD}(k)$ does not predict stable FCC solid at zero pressure. This EAM potential is referred to as MH(SA)^2 in Ref. [177].

Quantity	$\hat{C}^{(2)}_{MD}$ CDFT	M5R CDFT	9R CDFT	5R CDFT
Liquid density (Å^{-3})	0.0877	0.0879	0.0896	0.0923
(% Difference from $\hat{C}^{(2)}_{MD}$ CDFT)		(0.19%)	(2.1%)	(5.2%)
Solid density (Å^{-3})	0.0902	0.0901	0.0918	0.0940
(% Difference from $\hat{C}^{(2)}_{MD}$ CDFT)		-- [1]	(1.9%)	(4.3%)
Expansion in melting (Å^3/atom)	0.304	0.279	0.271	0.198
γ_{100} (erg/cm^2)	88.7	86.5	84.3	67.4
γ_{110} (erg/cm^2)	86.6	83.9	81.9	65.5
FCC crystal	S	MS	S	MS

Table 4.2: The liquid and solid properties computed from the M5R CDFT simulations, along with the 5R and 9R CDFT simulation results from Table 4.1.

4.6 Application of RFF to the PFC Method

As discussed in Section 4.2.2, it has been shown that the PFC method can be derived from the CDFT of freezing by two approximations [76]: (i) a fourth-order polynomial approximation of the ideal contribution; (ii) a polynomial approximation to the two-body DCF in Fourier space. To date, the polynomial approximations of the two-body DCF in the PFC formulations have at most considered resolving the first two peaks [78]. It has been demonstrated in Sections 4.4 and 4.5 that the RFF method can be used to accurately describe the two-body DCF up to the fourth peak, and possibly beyond. Thus, we seek to apply the RFF to the PFC method to enhance its predictive capability.

It is important to note that the RFF cannot be directly used in the PFC free energy functional because the evolution equation can potentially yield a discontinuous density profile as shown in Fig. 4.7(b). The reason for this is demonstrated by considering the approximation of the ideal contribution in Eq. (4.5). For instance, by taking $a_t = 0.6917$ and $b_t = 0.0854$ from Ref. [121], the approximation of the ideal contribution yields a double-well function as opposed to a single-well function, as shown in Fig. 4.7(a). This double-well behavior energetically favors the value of $n(\mathbf{r})$ to be separated

into values corresponding to the densities associated with the minima, and potentially leads to a discontinuous profile. In the PFC formulations such as those using the 4P and the 8P, the large anti-correlations at short-wavelengths in these fits prevent such discontinuity from forming. The asymptotic behavior of the RFFs at large k, on the other hand, does not pose sufficient energy penalty to prevent such discontinuity from forming. To illustrate this, we use the approximation to the ideal contribution in Eq. (4.5) along with the 3R, and evolve the density profile using the equilibrium density from the 3R CDFT simulation as the initial condition. After a few iterations, the resulting density profile yields discontinuities as shown in Fig. 4.7(b). The values of $n(\mathbf{r})$ at the peaks and troughs are around 0 and 9, which are close to the densities corresponding to the minima of the double-well function in Fig. 4.7(a).

In order to circumvent this issue, we propose an approximation to the two-body DCF of the following form:

$$\hat{C}^{(2)}_{RP}(k) = \sum_{j=1} \left[\frac{A_j}{k^2 + \alpha_j} + \frac{A_j^*}{k^2 + \alpha_j^*} \right] + \sum_{l=0}^{p} \mathcal{C}_l k^{2l} \,, \tag{4.14}$$

where the subscript RP denotes the combined RFF and polynomial fit, and A_j, α_j and $\mathcal{C}_l$ are fitting coefficients. By setting $\mathcal{C}_p$ (the coefficient of the highest-order polynomial term) to be negative, we can control $\hat{C}^{(2)}_{RP}(k)$ to approach negative infinity as $k \to \infty$, thus increasing the energy penalty for short-wavelength density waves. Figure 4.8 shows the resulting fits using 3, 5, and 7 partial-fraction terms, respectively. For each number of partial-fraction terms, we consider $p = 1$ and $p = 2$, which corresponds to including polynomial terms up to second and fourth order, respectively.

Jaatinen and coworkers have shown that the PFC free energy can predict a stable BCC phase of Fe whose properties are in agreement with those from experiments and MD simulations [121]. This is achieved by fitting the 8P to $\hat{C}^{(2)}_{MD}(k)$ so that the fit matches the value of $\hat{C}^{(2)}_{MD}(0)$, the k-value of the first peak, k_m, and the curvature at

the first peak, $d^2/dk^2\left[\hat{C}^{(2)}_{MD}(k_m)\right]$, as shown in Fig. 4.1(c). We demonstrate that the combined RFF and polynomial fit can capture similar features of $\hat{C}^{(2)}_{MD}(k)$ by using three terms in RFF and including up to the second-order polynomial term ($p = 1$). The resulting fit is shown in Fig. 4.9(a) where our fit is termed 3R2P. The 3R2P is almost identical to the 8P up to the first peak and begins to deviate from the 8P for higher k. Nevertheless, we show in Table 4.3 that the 3R2P captures almost the same features of the $\hat{C}^{(2)}_{MD}(k)$ as the 8P does. By using $a_t = 0.6917$ and $b_t = 0.0854$ for the ideal contribution in PFC, the resulting equilibrium BCC density profile from the 3R2P at $\bar{n} = 0.1$ is shown in Fig. 4.9(b). This density profile is very similar to the equilibrium density profile from the 8P at the same average density (see Figs. 4.9(c) and 4.9(d)).

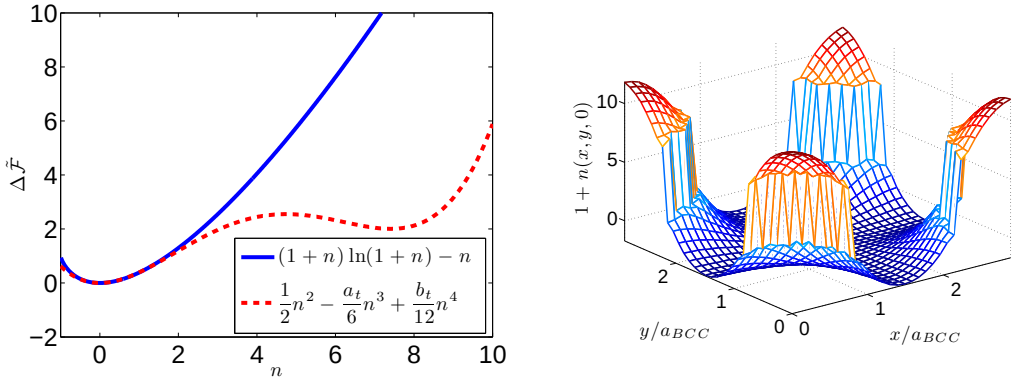

(a) (b)

Figure 4.7: The ideal contribution to the free energy as a function of the normalized density. The solid line denotes the ideal contribution from Eq. (4.3) while the dash line denotes the approximation from Eq. (4.5), where $a_t = 0.6917$ and $b_t = 0.0854$ [121]. (b) The density profile on the (100) crystal plane of the BCC solid from the simulation using the 3R and the ideal contribution represented by the dash line in (a).

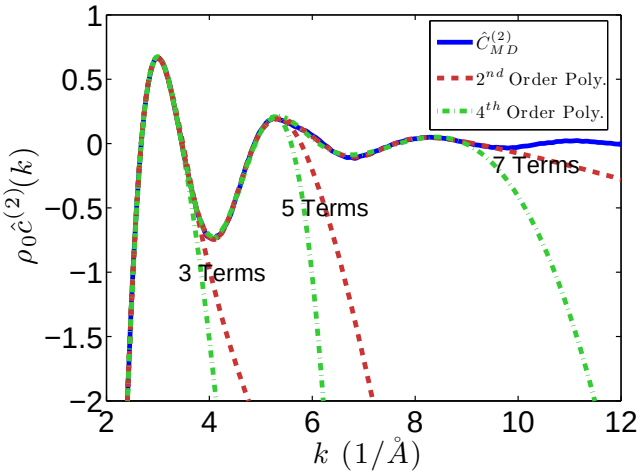

Figure 4.8: The different fits to the EAM-MD data (solid line) using the combined rational and polynomial functions. From the label, "2^{nd} Order Poly." denotes the fits that include up to k^2 in Fourier space and "4^{th} Order Poly." denotes those including k^2 and k^4 terms. The label "Terms" refers to the number of partial fraction terms in Eq. (4.14).

Quantity	8P	3R2P
$\hat{C}^{(2)}(0)$	-49.0	-49.0
k_m	2.99	2.98
$d^2/dk^2\left[\hat{C}^{(2)}(k_m)\right]$	-10.4	-10.4

Table 4.3: Comparison of the 8P and the 3R2P: the long-wavelength limit, $\hat{C}^{(2)}(0)$, the location of the first peak, k_m, and the curvature of the first peak, $d^2/dk^2\left[\hat{C}^{(2)}(k_m)\right]$.

4.7 Real-Space Implementation

In this section, we discuss numerical techniques for evaluating the convolution integral from Eq. (4.3) in real space. The partial fraction decomposition allows the convolution integral to be evaluated by solving a set of inhomogeneous Helmholtz equations. The convolution integral in consideration is in the following form:

$$\mathcal{I}_c(\mathbf{r}) = \int C^{(2)}(|\mathbf{r}-\mathbf{r}'|)n(\mathbf{r}')d\mathbf{r}'. \tag{4.15}$$

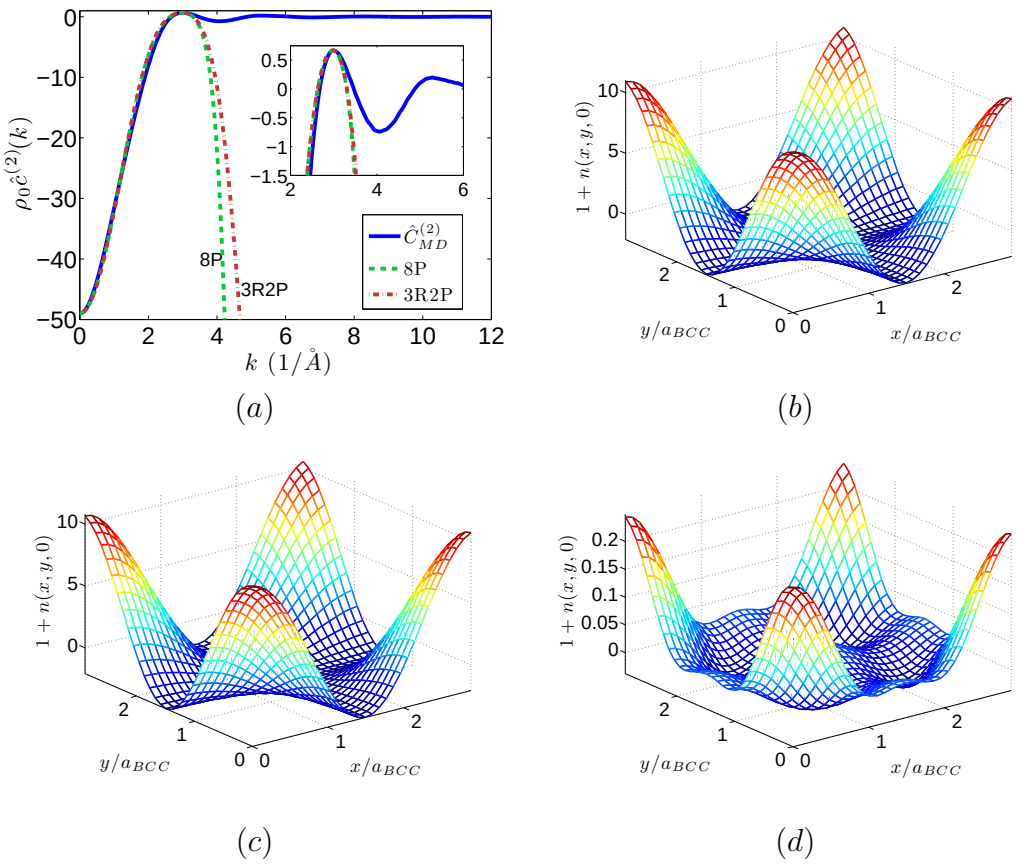

Figure 4.9: (a) The comparison between the 8P and the 3R2P. The solid line denotes the EAM-MD data. (b)-(c) The density profiles on the (100) crystal plane of the BCC solids at the solid-liquid coexistence from the PFC simulations using the 3R2P (b) and the 8P (c). (d) The difference between the density profiles of the 3R2P and 8P PFC simulations, where the profile of the 8P PFC is subtracted from that of the 3R2P PFC.

Using $C^{(2)}_{RFF}(|\mathbf{r}-\mathbf{r}'|)$, we can rewrite the convolution integral as

$$\mathcal{I}_c(\mathbf{r}) = \sum_j \left[L_j(\mathbf{r}) + L_j^*(\mathbf{r})\right] \ , \tag{4.16}$$

where L_j and L_j^* can be obtained from solving the inhomogeneous Helmholtz equations:

$$\begin{aligned} -\nabla^2 L_j(\mathbf{r}) + \alpha_j L_j(\mathbf{r}) &= A_j n(\mathbf{r}) \\ -\nabla^2 L_j^*(\mathbf{r}) + \alpha_j^* L_j^*(\mathbf{r}) &= A_j^* n(\mathbf{r}) \ . \end{aligned} \tag{4.17}$$

We note that $L_j(\mathbf{r})$ and $L_j^*(\mathbf{r})$ can also be computed from the following integral equations:

$$\begin{aligned} L_j(\mathbf{r}) &= A_j \int \left(\frac{e^{-\sqrt{\alpha_j}|\mathbf{r}-\mathbf{r}'|}}{4\pi|\mathbf{r}-\mathbf{r}'|} \right) n(\mathbf{r}')d\mathbf{r}' \\ L_j^*(\mathbf{r}) &= A_j^* \int \left(\frac{e^{-\sqrt{\alpha_j^*}|\mathbf{r}-\mathbf{r}'|}}{4\pi|\mathbf{r}-\mathbf{r}'|} \right) n(\mathbf{r}')d\mathbf{r}', \end{aligned} \tag{4.18}$$

where the kernels are the three-dimensional Green's functions of the Helmholtz equation. The free energy in Eq. (4.3) becomes

$$\begin{aligned} \Delta\tilde{\mathcal{F}}_{CDFT}\big(n(\mathbf{r})\big) &= \int d\mathbf{r}\,\{[1+n(\mathbf{r})]\ln[1+n(\mathbf{r})] - n(\mathbf{r})\} \\ &\quad -\frac{1}{2}\int d\mathbf{r}\left\{ n(\mathbf{r}) \sum_j \big[L_j(\mathbf{r}) + L_j^*(\mathbf{r})\big] \right\} \end{aligned} \tag{4.19}$$

and the same approach can be used to compute the PFC free energy that employs $C_{RP}^{(2)}(|\mathbf{r}-\mathbf{r}'|)$. The free energy in the above form provides a real-space formulation of the CDFT and PFC method, where the quantities $L_j(\mathbf{r})$ and $L_j^*(\mathbf{r})$ can be evaluated by direct methods such as LU factorization [178] or Krylov [179, 180] and classical pointwise iterative methods [181]. For direct solves, efficient parallel direct-solver libraries are widely available (MUMPS [182, 183], PARDISO [184, 185], SuperLU [186]) and are much faster than iterative methods when the factorization matrices of the discretization matrix can be stored and reused. However, the storage requirement rapidly increases with problem size, which becomes a limitation for large three-dimensional simulations. Iterative solvers, on the other hand, do not require the storage of the entire matrix and, therefore, are more suitable for large-scale simulations. However, we note that the discretization matrix of the Helmholtz equations in Eq. (4.17) are indefinite when the real part of α_j is negative. As a result, the computation of $L_j(\mathbf{r})$ and $L_j^*(\mathbf{r})$ using the iterative methods requires special treatments [187]. Many efforts over the past few decades have been devoted to the development of numerically ef-

ficient solvers for the Helmholtz equation that leads to an indefinite matrix, and we refer to a recent review article [188] and the references therein for a comprehensive overview of this field.

In this work, we use a point-wise iterative method to demonstrate our real-space formulation. We employ a two-step complex iterative Jacobi (CIJ) method [189] to solve the indefinite Helmholtz equation. When the discretization matrix of the Helmholtz equation is not indefinite[3], a standard iterative Jacobi (SIJ) method [181] is used. We note that the CIJ/SIJ method is chosen for its low memory requirement and simplicity in parallelization. Better convergence speeds are expected from more advanced methods such as the generalized minimal residual (GMRES) method [190] with appropriate preconditioners [187].

We compute the free energy densities of the BCC solid from the M5R CDFT simulations using the CIJ/SIJ method at different grid spacings: $\Delta h = a_{BCC}/16$, $a_{BCC}/32$, $a_{BCC}/64$, and $a_{BCC}/128$, where $a_{BCC}(= 2.95)$ is the normalized lattice spacing of the BCC solid. We then compare the results with the solid free energy density from the simulation using the Fourier spectral method at a smaller grid spacing of $\Delta h = a_{BCC}/256$, for which numerical convergence has been verified. The results are shown in Fig. 4.10(a) where the difference (as a measure of the numerical error) reduces as the grid spacing becomes smaller. In addition, we use the CIJ/SIJ method to simulate the interface between the liquid and BCC solid of the M5R CDFT simulation, as shown in Fig. 4.10(b).

[3]For a set of coefficients (α_i, A_j) where the real part of α_j is positive, the discretization matrix of the Helmholtz equation is not indefinite.

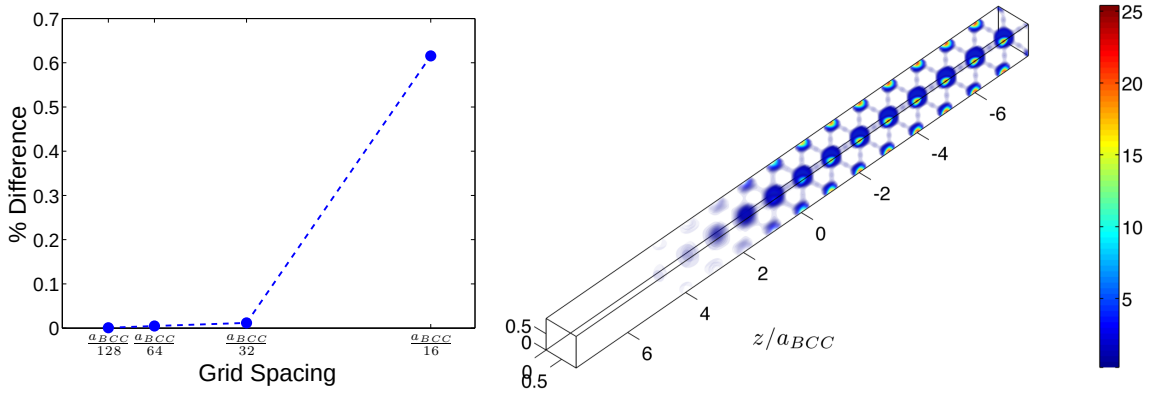

(a) (b)

Figure 4.10: (a) The difference between the solid free energy densities calculated from the M5R CDFT simulations using the CIJ/SIJ method and the numerically converged reference value. The reference value is calculated from the M5R CDFT simulation using the Fourier spectral method at a fine grid spacing of $\Delta h = a_{BCC}/256$. (b) The plot of $n(\mathbf{r})$ showing the interface between liquid and BCC solid from the M5R CDFT simulation using the CIJ/SIJ method.

4.8 Comparison of Fourier-Space and Real-Space Implementations

In this section, we compare the Fourier spectral method and real-space methods (CIJ/SIJ and LU factorization methods) for evaluating the convolution integral in Eq. (4.15). In a situation where the density profile is relatively uniform and the periodic boundary conditions are appropriate, the Fourier spectral method is a method of choice due to two advantages. First, the Fourier transform of the convolution integral in Eq. (4.15) can be written explicitly as

$$\hat{\mathcal{I}}_c(\mathbf{k}) = \hat{C}^{(2)}(|\mathbf{k}|)\hat{n}(\mathbf{k}), \tag{4.20}$$

where $\hat{n}(\mathbf{k})$ is the Fourier transforms of $n(\mathbf{r})$. Thus, the calculation of $\mathcal{I}_c(\mathbf{r})$ involves only simple pointwise operations (multiplication) and the Fourier transform operations, which can be efficiently performed by a fast Fourier transform (FFT). Examples

of open-source and commercial libraries/packages for FFT are FFTW [191] (employed in this work), IBM PESSL [192] and, more recently, P3DFFT [193]. To illustrate the advantage resulting from the expression in Eq. (4.20), we evaluate the convolution integral in Eq. (4.15) where the two-body DCF is the 5R and density profile is the equilibrium BCC-solid density profile from the 5R CDFT simulation with $\bar{n} = 0.18$ and the size of $32 \times 32 \times 32$ grid points. The calculation using the Fourier spectral method took 4.6×10^{-3} s whereas the calculations using the CIJ/SIJ and direct-solve methods using the MUMPS library took 2.9 s and 0.6 s, respectively (see also a footnote[4]), all of which are performed on two Quad-Core AMD Opteron 2356 Processors, with a total of eight processors.

The second advantage is that the Fourier spectral method allows for easy implementation of an implicit time stepping scheme in numerical integration. We note that there are other more sophisticated numerical algorithms developed for evolving PFC equations (see, for example, Refs. [194, 195, 196, 197, 198]). However, we consider the backward Euler time stepping scheme for simplicity. The backward Euler time stepping scheme can be written as

$$\hat{n}_{u+1}(\mathbf{k}) = \frac{1}{1 + \Delta\tau|\mathbf{k}|^2(1 - \hat{C}^{(2)}(|\mathbf{k}|))} \left[\hat{n}_u(\mathbf{k}) - \Delta\tau|\mathbf{k}|^2 \left(-\frac{a_t}{2}\mathcal{F}^T\left[n_u^2\right] + \frac{b_t}{3}\mathcal{F}^T\left[n_u^3\right]\right)\right], \tag{4.21}$$

where $\Delta\tau$ is the time step size, u and $u+1$ denote the current and next time steps, and $\mathcal{F}^T$ denotes the Fourier transform operation. Here, the nonlinear terms, n^2 and

[4]The reported time for the CIJ/SIJ method is obtained by using an initial condition that is slightly perturbed from the solution to the Helmholtz equation. The amount of perturbation is equivalent to time stepping Eq. (4.13) with a time step of 10^{-5}. The calculation time using the CIJ/SIJ method can be further reduced by choosing an initial condition that is perturbed even less from the solution. For example, using a perturbation equivalent to the time step of 10^{-8}, the calculation time reduces to 0.02 s. However, during evolution, the speedup factor per iteration ($3.4/0.02 = 170$) is much less than the factor of increase in the number of iterations ($10^{-5}/10^{-8} = 1000$). Therefore, to optimize the total simulation time, both calculation time per iteration and the number of iterations need to be considered.

n^3, are treated explicitly; i.e., they are evaluated at the time u, not $u+1$.

As an example, we calculate the maximum time step using the the backward Euler time stepping scheme for the 8P and the 3R2P. The maximum time step is determined by a convergence test where the convergence values, V_w and V_n, for the energy and the density profile, respectively, are defined by

$$V_w = \sqrt{\frac{\left\langle (\tilde{w}_s - \tilde{w}_r)^2 \right\rangle}{\left\langle (\tilde{w}_r - \langle \tilde{w}_r \rangle)^2 \right\rangle}} \times 100, \tag{4.22}$$

and

$$V_n = \sqrt{\frac{\left\langle (n_s - n_r)^2 \right\rangle}{\left\langle (n_r - \langle n_r \rangle)^2 \right\rangle}} \times 100, \tag{4.23}$$

where the subscript s denotes the quantity calculated from the simulation using $\Delta\tau = s$ and the subscript r denotes the reference quantity which is taken to be that calculated using $\Delta\tau = 10^{-7}$. The notation $\langle x \rangle$ denotes the arithmetic mean of x and the quantity $\tilde{w} \equiv \tilde{w}(\tilde{\mathbf{r}})$ is the position-dependent scaled energy density:

$$\tilde{w}(\tilde{\mathbf{r}}) = \frac{1}{2} n(\tilde{\mathbf{r}})^2 - \frac{a_t}{6} n(\tilde{\mathbf{r}})^3 + \frac{b_t}{12} n(\tilde{\mathbf{r}})^4 - \frac{n(\tilde{\mathbf{r}})}{2} \int C^{(2)}(|\tilde{\mathbf{r}} - \tilde{\mathbf{r}}'|) n(\tilde{\mathbf{r}}') d\tilde{\mathbf{r}}', \tag{4.24}$$

where $\tilde{\mathbf{r}}$ and $\tilde{\mathbf{r}}'$ denote the scaled spatial coordinates. The initial density profile is the equilibrium BCC-solid density profile from the 5R CDFT simulations (size of 32^3 grid points) as shown in Fig. 4.4(d) and the simulation parameters are given by $a_t = 0.6917$, $b_t = 0.0854$, and the grid spacing of 0.093. We calculate the convergence values at $\tau = 0.2$ and tabulate the results in Table 4.4. For the convergence values less than 0.01%, the largest time step sizes are on the order of 10^{-4}.

However, when the density profile is nonperiodic and/or highly non-uniform, a real-space implementation can be advantageous. First, the real-space formulation allows reduction of the degrees of freedom through the use of adaptive mesh refinement

(AMR) in finite element methods and finite difference methods. AMR can be useful in a situation where a portion of the domain is liquid, which is represented by a uniform density, as in the early stage of solidification, as well as in CDFT simulations in which the density is highly concentrated only near the lattice positions and is nearly uniform elsewhere. In such cases, a finely spaced mesh can be placed where the atomic density changes rapidly, while a coarser mesh can be used elsewhere. Therefore, we expect that the adaptivity of the mesh can play an important role in increasing numerical efficiency. Another potential advantage is the flexibility in implementing different basis functions. For example, for the CDFT case, a Gaussian basis may yield better convergence and further reduction in the degree of freedom. Such an approach has been applied to quantum density functional theory calculations [199]. Lastly, the real-space formulation also allows for the development of multi-scale techniques such as the quasicontinuum reduction of field theories [200, 201] (proposed originally in the context of electronic structure calculations [200]), which can potentially enable large-scale CDFT and PFC simulations.

	8P		3R2P	
$\Delta\tau$	V_w (%)	V_n (%)	V_w (%)	V_n (%)
10^{-1}	60	32	60	33
10^{-2}	3.2	3.7	3.2	3.8
10^{-3}	3.1×10^{-1}	3.6×10^{-1}	2.9×10^{-1}	3.4×10^{-1}
10^{-4}	2.9×10^{-2}	3.4×10^{-2}	2.5×10^{-2}	2.9×10^{-2}
10^{-5}	2.7×10^{-3}	3.0×10^{-3}	2.3×10^{-3}	2.7×10^{-3}
10^{-6}	7.4×10^{-4}	2.6×10^{-4}	2.1×10^{-4}	2.4×10^{-4}

Table 4.4: The comparison of the convergence values at different time step sizes using the backward Euler time stepping scheme. These values are evaluated at $\tau = 0.2$.

4.9 Chapter Summary and Discussions

We proposed a rational function fit (RFF) to describe the two-body DCF in Fourier space in order to alleviate the computational demand of the CDFT and enhance the predictive capability of the PFC method.

- We used the RFFs to show that the short-wavelength contributions of the two-body DCF play an important role in determining the thermodynamic properties of materials. Our studies demonstrate that an inaccurate representation of the correlations in the two-body DCF in favor of more computationally efficient density profiles may result in inaccurate predictions. In particular, we find that the correlations up to the third peak of the Fe DCF are important.

- We showed that it is possible to empirically parameterize the two-body DCF such that most of the predicted thermodynamic properties are in agreement with the CDFT simulation using the full two-body DCF without incurring significant computational costs.

- A combined RFF and polynomial fit was shown to provide an improved representation of the two-body DCF in the PFC method.

- The RFF method allows the convolution integral to be numerically evaluated in real space by solving a set of inhomogeneous Helmholtz equations. Such a real-space formulation enables descriptions of nonperiodic systems and the use of non-uniform/adaptive grids.

We note that another method of constructing the two-body DCF in Fourier space was recently proposed using Gaussian functions and was applied to the PFC method to study phase transformations [122, 133]. The use of Gaussian functions is a convenient choice for constructing a kernel corresponding to the DCF that results in various stable equilibrium crystal structures because it allows one to control the location

and the width of the peaks precisely. However, the RFF is an appropriate choice when the two-body DCF obtained from experiments or MD simulations needs to be accurately described; it is difficult to use the Gaussian function to describe the oscillatory behavior of two-body DCFs. Furthermore, the RFF allows for a real-space formulation via the solution of Helmholtz equations, and provides the framework for development of multiscale methods, which is a topic for future investigation.

CHAPTER V

Calculations of Isothermal Elastic Constants in the Phase-Field Crystal Model

5.1 Overview

In this chapter, we consider the isothermal elastic constants that were calculated from the PFC approach in Refs. [64, 65, 78]. These elastic constants, which will be referred to as the PFC elastic constants, are calculated from variations in the free energy density (total free energy per actual volume) associated with various types of quasi-static deformation at a constant average number density. However, we have found that this procedure is inconsistent with the definitions from a theory of thermoelasticity of stressed materials [79, 80, 81]. These definitions are thermodynamically derived and are widely adopted. Therefore, we propose an alternative procedure for calculating the elastic constants as defined by the thermoelasticity theory, which will be referred to as the TE elastic constants. The TE elastic constants are instead calculated from variations in the total free energy per undeformed volume associated with quasi-static deformations at a constant number of particles in the system. To give numerical examples, we use an existing PFC model for iron (Fe) to show that the PFC and TE elastic constants can be significantly different from one another. Therefore, we conclude that the conventional and the proposed procedures are not

interchangeable and, more importantly, one should calculate the elastic constants using the proposed procedure in order to make fair comparisons with values from other approaches such as classical density functional theory [82, 83, 84], Monte Carlo [85], MD [86], and *ab initio* density functional theory [87, 88, 89].

Furthermore, by comparing the conventional and the proposed procedures, we identify two differences in the calculation procedures that contribute to the discrepancies between the PFC and TE elastic constants. The first is due to the frame in which the free energy density is calculated; the PFC elastic constants are calculated from the free energy density measured with respect to the deformed frame of reference while the TE elastic constants are calculated from the free energy density measured with respect to the undeformed frame. The difference arises due to the different volumes in these two frames. The second difference is due to the constraint imposed on the quasi-static deformations; the constraint for the PFC elastic constants is a constant average number density, whereas the constraint for the TE elastic constant is a constant number of particles.

Finally, we employ a thermodynamic theory of stressed solids [90, 91, 92] to systematically define the PFC and TE elastic constants in the same framework. This formulation allows us to obtain the relationships between the PFC and TE elastic constants. These relationships not only facilitate conversions between the PFC and TE elastic constants but also provide quantitative measures of the differences between the PFC and TE elastic constants in terms of thermodynamic quantities such as the pressure of the undeformed state.

This chapter is organized as follows. In Section 5.2, we reintroduce the PFC equations that will be used throughout the chapter, and briefly review continuum mechanics and the theory of thermoelasticity of stressed materials. Next, we review the conventional procedure for calculating the PFC elastic constants in Section 5.3.1 and propose the alternative procedure for calculating the TE elastic constants using

the PFC method in Section 5.3.2. We then present numerical comparisons between the PFC and TE elastic constants, and present further discussions in Section 5.3.3. Furthermore, we present a more general procedure for calculating the PFC elastic constants and propose formal definitions of the PFC elastic constants in Section 5.4. We then derive the relationships between the PFC and TE elastic constants of a system with cubic symmetry using the thermodynamic theory of stressed solids in Section 5.5. Lastly, we conclude this chapter with a summary in Section 5.6.

5.2 Background

5.2.1 PFC Method

We consider the following free energy for the PFC method [65]:

$$\mathcal{F} = \int w(\phi)\, d\mathbf{R}, \qquad w(\phi) \equiv \frac{\phi}{2}\left[a_t + \lambda(q_0^2 + \nabla^2)^2\right]\phi + g_t\frac{\phi^4}{4}, \tag{5.1}$$

where, $w(\phi)$ is the free energy density, and a_t, g_t, λ, and q_0 are fitting parameters. The number density field, ϕ, can be expressed in a Fourier expansion of the form:

$$\phi(\mathbf{R}, \phi_{ave}) = \phi_{ave} + \sum_i A_i e^{i\mathbf{G}_i\cdot\mathbf{R}} + \text{c.c.}, \tag{5.2}$$

where A_i is the amplitude, ϕ_{ave} is the average number density, $\mathbf{R}$ is the real-space position vector ($\mathbf{R} = R_1\mathbf{i} + R_2\mathbf{j} + R_3\mathbf{k}$, where $\mathbf{i}$, $\mathbf{j}$ and $\mathbf{k}$ constitute an orthonormal Cartesian basis), $\mathbf{G}_i$ is the reciprocal lattice vector (RLV) that is constructed from the reciprocal basis of a periodic structure, and c.c. denotes the complex conjugate. We define the following dimensionless parameters [65]:

$$\begin{aligned} \tilde{\mathbf{R}} &\equiv q_0\mathbf{R}, \qquad \epsilon \equiv -\frac{a_t}{\lambda q_0^4}, \qquad \tilde{\phi} \equiv \sqrt{\frac{g_t}{\lambda q_0^4}}\phi, \\ \tilde{\mathcal{F}} &\equiv \frac{g_t}{\lambda^2 q_0^{8-d}}\mathcal{F}, \qquad \tilde{h} \equiv \frac{g_t}{\lambda^2 q_0^8}h, \end{aligned} \tag{5.3}$$

where d is the dimensionality of the problem. The PFC free energy can then be written in a simpler form:

$$\tilde{\mathcal{F}} = \int \tilde{w}\left(\tilde{\phi}\right)\ d\tilde{\mathbf{R}}, \qquad \tilde{w}\left(\tilde{\phi}\right) = \frac{\tilde{\phi}}{2}\left[-\epsilon + \left(1+\tilde{\nabla}^2\right)^2\right]\tilde{\phi} + \frac{\tilde{\phi}^4}{4}. \tag{5.4}$$

In this work, we will consider a body-centered-cubic (BCC) crystal, of which the set of smallest RLVs has the magnitude of $2\pi\sqrt{2}/L_a$, where L_a is the side length of a cubic unit cell. We will therefore set $q_0 = 2\pi\sqrt{2}/L_a$ in order to make the PFC free energy functional favor the BCC structure. The simplest analytical expression for the BCC structure, the so-called one-mode approximation, can be obtained by keeping only the terms with $|\mathbf{G}_i| = 2\pi\sqrt{2}/L_a$ in the expansion of Eq. (5.2):

$$\begin{aligned}\tilde{\phi}_{one}(\tilde{\mathbf{R}}, \tilde{\phi}_{ave}) &= \tilde{\phi}_{ave} + \tilde{A}_s\Bigg[\cos\left(q_1\tilde{R}_1\right)\cos\left(q_1\tilde{R}_3\right) \\ &\quad + \cos\left(q_1\tilde{R}_2\right)\cos\left(q_1\tilde{R}_3\right) + \cos\left(q_1\tilde{R}_1\right)\cos\left(q_1\tilde{R}_2\right)\Bigg],\end{aligned} \tag{5.5}$$

where $\tilde{A}_s$ is the nondimensionalized amplitude and $q_1 = 1/\sqrt{2}$. Henceforth, we will omit the tilde notation for the nondimensionalized quantities.

5.2.2 Measure of Deformation

We denote the undeformed state of a material as the state prior to the deformations of the material. In other words, the material is subjected to zero strain, but not necessarily zero stress. We use (R_1, R_2, R_3) to denote the undeformed coordinates of the position of a volume element in the material while using (r_1, r_2, r_3) to denote the deformed coordinates of the position. Since we assume that both coordinates share the same basis, the deformation gradient tensor, α_{ij}, and the displacement gradient tensor, u_{ij}, are written as

$$\alpha_{ij} = \frac{\partial r_i}{\partial R_j}, \tag{5.6}$$

and

$$u_{ij} = \frac{\partial(r_i - R_i)}{\partial R_j}, \tag{5.7}$$

where the subscripts i and j vary from 1 to 3, and it follows that $u_{ij} = \alpha_{ij} - \delta_{ij}$. The symbol δ_{ij} is the Kronecker delta and the Einstein summation notation is used throughout the chapter unless stated otherwise. The deformation considered in this work is the affine or homogeneous deformation, and thus we can write [202, 203]

$$r_i = \alpha_{ij} R_j = (u_{ij} + \delta_{ij}) R_j. \tag{5.8}$$

Conversely, we can write R_i in terms of r_j:

$$R_i = \alpha_{ij}^{-1} r_j, \tag{5.9}$$

where $\alpha_{ij}^{-1} = \partial R_i / \partial r_j$. For brevity, we write the above transformation in tensor notation: $\mathbf{R} = \boldsymbol{\alpha}^{-1} \cdot \mathbf{r}$, where $\mathbf{r} = r_1\mathbf{i} + r_2\mathbf{j} + r_3\mathbf{k}$. The Lagrangian strain tensor is expressed as

$$E_{ij} = \frac{1}{2}\left(\alpha_{ki}\alpha_{kj} - \delta_{ij}\right) = \frac{1}{2}\left(u_{ij} + u_{ji} + u_{ki}u_{kj}\right), \tag{5.10}$$

and is employed in a nonlinear elasticity theory. In a linear elasticity theory, one assumes infinitesimal deformations and defines the symmetric small-strain tensor,

$$\epsilon_{ij} = \frac{1}{2}\left(u_{ij} + u_{ji}\right), \tag{5.11}$$

and the antisymmetric small-strain tensor,

$$\omega_{ij} = \frac{1}{2}\left(u_{ij} - u_{ji}\right). \tag{5.12}$$

Equations (5.11) and (5.12) can be used to calculate u_{ij} from

$$u_{ij} = \frac{1}{2}(\epsilon_{ij} + \epsilon_{ji} + \omega_{ij} - \omega_{ji}). \tag{5.13}$$

5.2.3 Definitions of Isothermal Elastic Constants from the Thermoelasticity Theory

The definitions of the isothermal elastic constants from the theory of thermoelasticity of stressed materials [79, 80, 81] depend on the choice of the independent variables of the Helmholtz free energy, F (not necessarily identical to $\mathcal{F}$ introduced earlier). The Helmholtz free energy of a nonhydrostatically stressed system can be written in the form:

$$F(\theta, a_{ij}, N, R_i), \tag{5.14}$$

where θ is temperature, a_{ij} denotes either E_{ij} or ϵ_{ij}, N is the number of atoms or particles, and R_i is the reference or undeformed coordinates. Since we consider R_i as constant, we will omit this dependence subsequently.

The elastic constants, as well as other thermodynamic quantities, can be defined from the Taylor expansion of the free energy around the undeformed state and we refer to Appendix B for more details. The coefficients of the first-order terms with respect to the elements of the strain tensors give the following definitions [81, 202]:

$$T^u_{ij} = \frac{1}{\mathcal{V}} \frac{\partial F}{\partial E_{ij}}\bigg|^u_{\theta, E^*_{mn}, N} = \frac{1}{\mathcal{V}} \frac{\partial F}{\partial \epsilon_{ij}}\bigg|^u_{\theta, \epsilon^*_{mn}, N}, \tag{5.15}$$

where $\mathcal{V}$ is the volume of the system at the undeformed state and T^u_{ij} is an element of the symmetric second Piola-Kirchhoff stress tensor [202] evaluated at the undeformed state. The subscripts E^*_{mn} and ϵ^*_{mn} indicate that the elements of the strain tensors other than those involved in the partial derivative are held constant, and the super-

script u indicates that the partial derivatives are evaluated at the undeformed state.

The coefficients of the second-order terms with respect to the elements of the strain tensors yield the definitions of elastic constants [81, 202]:

$$C_{ijkl} = \frac{1}{\mathcal{V}} \frac{\partial^2 F}{\partial E_{ij} \partial E_{kl}} \bigg|^{u}_{\theta, E^*_{mn}, N}, \tag{5.16}$$

and

$$K_{ijkl} = \frac{1}{\mathcal{V}} \frac{\partial^2 F}{\partial \epsilon_{ij} \partial \epsilon_{kl}} \bigg|^{u}_{\theta, \epsilon^*_{mn}, N}, \tag{5.17}$$

in the nonlinear and linear elasticity theories, respectively. The elastic constants C_{ijkl} and K_{ijkl}, both referred to as the TE elastic constants, are fourth-order tensors with complete Voigt symmetry for the indices, i.e., $C_{ijkl} = C_{jikl}$, $C_{ijkl} = C_{ijlk}$, and $C_{ijkl} = C_{klij}$, and similarly for K_{ijkl}. For a cubic material, each set of C_{ijlk} and K_{ijkl} reduces to three independent values which are (no summation) $C_{11} = C_{iiii}$, $C_{12} = C_{iijj}$ and $C_{44} = C_{ijij} = C_{ijji}$ with the other elements being zero. Similar notation applies to the elastic constants K_{ijkl}.

For a cubic material under hydrostatic pressure, P_u, of the undeformed state, which is considered in this work, the relationships between $C_{\alpha\beta}$ and $K_{\alpha\beta}$ are [81]

$$C_{11} = K_{11} + P_u, \qquad C_{12} = K_{12}, \qquad C_{44} = K_{44} + \frac{P_u}{2}, \tag{5.18}$$

where the details of the derivation are shown in Appendix B.

The above relationships reveal the fact that the elastic constants defined by the linear and nonlinear elasticity theories are not in general equal to one another even at the limit of zero strain (undeformed state). Only when the pressure of the undeformed state is zero do these two set of elastic constants become identical. For simulations

of materials under ambient pressure, the magnitude of the pressure is typically much smaller than that of the elastic constants, and therefore, the two sets of elastic constants are approximately equal. However, for simulations of materials under high pressure [89, 204, 205], the two sets of the elastic constants can differ significantly. We find that, for the parameterized PFC model used in this work, the magnitude of the pressure is not negligible compared with that of the elastic constants.

5.2.4 Deformation Types

In this work, we will calculate both the PFC and TE elastic constants using the PFC approach. Since the PFC free energy is not an explicit function of the elements of a strain tensor, one cannot directly calculate the elastic constants by taking the second derivatives of the free energy with respect to the element of the strain tensors, as shown in Eqs. (5.16) and (5.17). Instead, one extracts the values of the elastic constants from variations in the free energy density with respect to various types of quasi-static deformations, as will be shown in Section 5.3. For the elastic constants of a cubic material, we need three deformation types in order to obtain a set of linearly independent equations to solve for three unknowns. We choose to consider the following types of deformation:

- isotropic deformation characterized by $u_{ij} = \delta_{ij}\xi$, where ξ is a parameter quantifying the amount of deformation (hereafter referred to as the "small deformation parameter"),
- biaxial deformation where the nonzero elements are $u_{11} = \xi$ and $u_{22} = -\xi$,
- simple-shear deformation where the nonzero element is $u_{12} = -\xi$.

These deformations are chosen because we are aiming to make a direct comparison with the previous PFC studies [65, 78]. We note that we could use any other type of affine deformation to extract the elastic constants as long as they give three linearly

independent equations. For example, we could use a volume-conserving biaxial deformation, where the nonzero elements are $u_{11} = 1+\xi$ and $u_{22} = 1/(1+\xi)$, instead of the biaxial deformation presented above. If the volume-conserving biaxial deformation were used along with the isotropic and simple-shear deformations, we would obtain a different set of three linearly independent equations; nevertheless, the solution to the system of equations would be the same, yielding the same values of the elastic constants.

(i) Deformation	(ii) $\phi\left(\boldsymbol{\alpha}^{-1}\cdot\mathbf{r}\right)$	(iii) $\int_{V_n(\xi)} d\mathbf{r}$	(iv) $V_n(\xi)$
Isotropic $(n=1)$	$\phi\left(\boldsymbol{\alpha}^{-1}\cdot\mathbf{r}\right)=\phi\left(\frac{r_1}{1+\xi},\frac{r_2}{1+\xi},\frac{r_3}{1+\xi}\right)$	$\int_0^{L_a(1+\xi)}\int_0^{L_a(1+\xi)}\int_0^{L_a(1+\xi)} dr_1dr_2dr_3$	$L_a^3(1+\xi)^3$
Biaxial $(n=2)$	$\phi\left(\boldsymbol{\alpha}^{-1}\cdot\mathbf{r}\right)=\phi\left(\frac{r_1}{1+\xi},\frac{r_2}{1-\xi},r_3\right)$	$\int_0^{L_a}\int_0^{L_a(1-\xi)}\int_0^{L_a(1+\xi)} dr_1dr_2dr_3$	$L_a^3(1-\xi^2)$
Simple Shear $(n=3)$	$\phi\left(\boldsymbol{\alpha}^{-1}\cdot\mathbf{r}\right)=\phi\left(r_1+\xi r_2,r_2,r_3\right)$	$\int_0^{L_a}\int_0^{L_a}\int_{-\xi r_2}^{L_a-\xi r_2} dr_1dr_2dr_3$	L_a^3

Table 5.1: A list of (i) types of deformation, (ii) functional forms of density profiles in terms of the deformed coordinates, $\phi\left(\boldsymbol{\alpha}^{-1}\cdot\mathbf{r}\right)$, (iii) expressions for the integration over the deformed unit cell, and (iv) the deformed volume of the unit cell, $V_n(\xi)$. The unit cell is cubic with a side length of L_a in the undeformed state.

5.3 Calculations of Isothermal Elastic Constants using PFC Free Energy

In this section, we review the conventional procedure for calculating the PFC elastic constants and propose the alternative procedure for calculating the TE elastic constants using the PFC free energy. We present numerical results from an existing PFC model for BCC Fe to show that the PFC and TE elastic constants can be significantly different, and then discuss the implications of the results.

5.3.1 PFC Elastic Constants

We describe the procedure for obtaining the PFC elastic constants of a BCC crystal using the PFC free energy and the one-mode approximation as a density profile [78]. We first write $\phi_{one}(\mathbf{R}, \phi_{ave})$ in terms of the deformed coordinates, or $\phi_{one}(\boldsymbol{\alpha}^{-1} \cdot \mathbf{r}, \phi_{ave})$, and then obtain the total energy by integrating $w(\phi_{one})$ over the deformed unit cell at a constant average density ϕ_{ave}:

$$\mathcal{F}_n(\xi, \phi_{ave}) = \int\limits_{V_n(\xi)} w\Big(\phi_{one}\left(\boldsymbol{\alpha}^{-1} \cdot \mathbf{r}, \phi_{ave}\right)\Big)\, d\mathbf{r}, \tag{5.19}$$

where the limit of the integration is shown in Table 5.1 and the variable $V_n(\xi)$ is the deformed volume. We have assumed an isothermal condition and thus omitted the dependence of the free energy on θ. The subscript $n(= 1, 2, 3)$ denotes the types of deformation shown in Table 5.1, and we evaluate the quantities with the subscript n separately for each deformation type. The PFC elastic constants are obtained from calculating the following quantities:

$$\begin{aligned} \Delta h_n(\xi, \phi_{ave}) &\equiv \frac{\mathcal{F}_n(\xi, \phi_{ave})}{V_n(\xi)} - \frac{\mathcal{F}_n(0, \phi_{ave})}{V_n(0)} \\ &= h_n(\xi, \phi_{ave}) - h_n(0, \phi_{ave}), \end{aligned} \tag{5.20}$$

where $h_n(\xi, \phi_{ave})$ can be interpreted as the "bulk" free energy density because it is spatially independent. The second-order coefficient of the Taylor expansion of $\Delta h_n(\xi, \phi_{ave})$ around $\xi = 0$ is related to the cubic elastic constants, $H_{\alpha\beta}$, as follows:

$$\begin{aligned}
\Delta h_1(\xi, \phi_{ave}) &= ... + \frac{1}{2}\left(3H_{11} + 6H_{12}\right)\xi^2 + ... \\
\Delta h_2(\xi, \phi_{ave}) &= ... + \frac{1}{2}\left(2H_{11} - 2H_{12}\right)\xi^2 + ... \\
\Delta h_3(\xi, \phi_{ave}) &= ... + \frac{1}{2}(H_{44})\xi^2 + ..., \qquad (5.21)
\end{aligned}$$

where we use the subscript $\alpha\beta$ to denote 11, 12, or 44. We note that $H_{\alpha\beta}$ are functions of ϕ_{ave}, which is not explicitly indicated for brevity. To put the above calculation in the same context as that in the next section, we note that the method in finding the elastic constants in Eq. (5.21) is equivalent to calculating the second-order partial derivative of the free energy density with respect to the small deformation parameter,

$$\mathcal{Q}_n^{PFC}(\phi_{ave}) \equiv \frac{\partial^2}{\partial \xi^2}\left(\frac{\mathcal{F}_n(\xi, \phi_{ave})}{V_n(\xi)}\right)\Bigg|_{\theta, \phi_{ave}}^{\xi=0}, \qquad (5.22)$$

and solving for the elastic constants from

$$\begin{aligned}
\mathcal{Q}_1^{PFC}(\phi_{ave}) &= 3H_{11} + 6H_{12} \\
\mathcal{Q}_2^{PFC}(\phi_{ave}) &= 2H_{11} - 2H_{12} \\
\mathcal{Q}_3^{PFC}(\phi_{ave}) &= H_{44}. \qquad (5.23)
\end{aligned}$$

We emphasize that the partial derivatives in Eq. (5.22) are performed at constant ϕ_{ave}, as indicated in the subscript at the vertical line. We also note that the two procedures described above are only valid for the density profiles that minimize (or maximize) the bulk free energy density with respect to deformations at a constant average number density. For these density profiles, the first derivative of the free

energy density with respect to a small deformation variable at a constant average number density is zero. In the context of this work where the density profiles are described by the one-mode approximation, the two procedures above are only valid for the density profiles that minimize $h_n(\xi, \phi_{ave})$ with respect to ξ at constant ϕ_{ave}. However, in Section 5.4, we will present a more general procedure to calculate the PFC elastic constants that applies to a density profile that does not necessarily minimize $h_n(\xi, \phi_{ave})$ with respect to ξ at constant ϕ_{ave}.

5.3.2 TE Elastic Constants

We now propose the alternative procedure for obtaining the TE elastic constants defined in Eqs. (5.16) and (5.17) from the PFC free energy. We evaluate the integral similar to that from Eq. (5.19), but with a condition that the total number of particles,

$$N_T = \int_{\mathcal{V}} \phi_{one}(\mathbf{R}, \phi_{ave}) d\mathbf{R}, \tag{5.24}$$

remains constant during the deformations. This means that the average density ϕ_{ave} will no longer remain constant and we write

$$\phi_{ave} \equiv \phi_{ave,n}(\xi) = \frac{N_T}{V_n(\xi)} = \frac{N_T/\mathcal{V}}{V_n(\xi)/\mathcal{V}} = \frac{\phi'_{ave}}{J_n(\xi)}, \tag{5.25}$$

where $J_n(\xi) = V_n(\xi)/\mathcal{V}$ and ϕ'_{ave} is the total number of particles per undeformed volume. Because the undeformed volume $\mathcal{V}$ is constant, holding ϕ'_{ave} constant during the deformations is equivalent to holding N_T constant. The integration of the PFC free energy with respect to the deformed coordinates is then

$$\mathcal{F}_n(\xi, \phi'_{ave}) = \int_{V_n(\xi)} w\left(\phi_{one}\left(\boldsymbol{\alpha}^{-1} \cdot \mathbf{r}, \frac{\phi'_{ave}}{J_n(\xi)}\right)\right) d\mathbf{r}, \tag{5.26}$$

where we have assumed that $\mathcal{F}_n$ is the total Helmholtz free energy. We then proceed to calculate

$$\mathcal{Q}_n^{TE}(\phi'_{ave}) \equiv \frac{\partial^2}{\partial \xi^2}\left(\frac{\mathcal{F}_n(\xi,\phi'_{ave})}{\mathcal{V}}\right)\Bigg|_{\theta,\phi'_{ave}}^{\xi=0}, \tag{5.27}$$

where we emphasize that $\mathcal{F}_n(\xi,\phi'_{ave})$ is obtained from the deformations with constant ϕ'_{ave}. We note that in the limit of $\xi = 0$, we have $V = \mathcal{V}$ and therefore, $\phi_{ave} = \phi'_{ave}$. Using the chain rule, one can write the second derivative with respect to ξ as

$$\frac{\partial^2}{\partial \xi^2} = \frac{\partial^2 E_{ij}}{\partial \xi^2}\frac{\partial}{\partial E_{ij}} + \frac{\partial E_{ij}}{\partial \xi}\frac{\partial E_{kl}}{\partial \xi}\frac{\partial^2}{\partial E_{ij}\partial E_{kl}}, \tag{5.28}$$

where the derivative is performed with constant θ and ϕ'_{ave}. Using the transformation in Eq. (5.28) with Eq. (5.27), one arrives at a system of equations to solve for the elastic constants $C_{\alpha\beta}$ (Refs. [82, 85]):

$$\begin{aligned}
\mathcal{Q}_1^{TE}(\phi'_{ave}) &= 3C_{11} + 6C_{12} - 3P_u, \\
\mathcal{Q}_2^{TE}(\phi'_{ave}) &= 2C_{11} - 2C_{12} - 2P_u, \\
\mathcal{Q}_3^{TE}(\phi'_{ave}) &= C_{44} - P_u,
\end{aligned} \tag{5.29}$$

where it is assumed that the material has cubic symmetry and is under the hydrostatic pressure, P_u, in the undeformed state.[1] The elastic constants $C_{\alpha\beta}$ are functions of ϕ'_{ave} or, equivalently, ϕ_{ave} because they are evaluated at the undeformed state. The pressure can be calculated from the isotropic deformation ($n = 1$):

$$P_u = -\frac{1}{3}\frac{\partial}{\partial \xi}\left(\frac{\mathcal{F}_1(\xi,\phi'_{ave})}{\mathcal{V}}\right)\Bigg|_{\theta,\phi'_{ave}}^{\xi=0}. \tag{5.30}$$

[1]The quantities $\mathcal{Q}_n^{TE}$ are related to the bulk modulus, B, and the shear moduli, μ and μ' (defined in Ref. [206]), through the following equations: $\mathcal{Q}_1^{TE}(\phi'_{ave}) = 9B - 6P_u$, $\mathcal{Q}_2^{TE}(\phi'_{ave}) = 4\mu'$, $\mathcal{Q}_3^{TE}(\phi'_{ave}) = \mu$. The relationships between the set of elastic constants B, μ, and μ', and the set of $C_{\alpha\beta}$ are reported in Eq. (3b) of Ref. [206], for example.

After obtaining $C_{\alpha\beta}$, we can simply calculate $K_{\alpha\beta}$ from Eq. (5.18). We emphasize that we do not calculate $K_{\alpha\beta}$ from the procedure similar to the one used to obtain $C_{\alpha\beta}$ because the procedure will yield values of $K_{\alpha\beta}$ that are inconsistent with the definition in Eq. (5.17). We discuss this issue in Appendix C.

5.3.3 Numerical Comparison Between PFC and TE Elastic Constants

To elucidate the implications of the above analysis, we proceed to numerically compare the PFC and TE elastic constants. We use a PFC model for BCC Fe since it has been more extensively studied. There have been two studies of BCC Fe using the PFC method; one study was performed by Jaatinen et al. [121] and the other study was conducted by Wu et al. [153] We do not examine the PFC model from the former study here because the corresponding free energy is the energy difference from that of the reference liquid state. As a result, we would need to consider the quantities pertaining to the reference liquid state, which is beyond the scope of the present work. On the other hand, the PFC free energy used by Wu et al. [153] (described in Section 5.2.1) is based on a phenomenological model [64] and can be considered as the total energy of the system. Therefore, we will use the parameterization of the PFC method presented in the study by Wu et al. [153] The values of the PFC fitting parameters used in this work are as follows [153]: $q_0 = 2.985$ Å^{-1}, $\lambda = 0.291$ eVÅ^7, $\epsilon = 0.0923$, and $g_t = 9.703$ eVÅ^9 (see also a footnote[2]).

Figure 5.1 shows the plots of the PFC elastic constants, the TE elastic constants, and the pressure at the undeformed state as functions of ϕ_{ave}; the values of these elastic constants at the liquid-solid coexistence density ($\phi_{ave} = -0.201$) are reported in Table 5.2 in Rows (i) to (iii). In Row (iv), we tabulate the PFC elastic constants calculated in Ref. [78] for comparison with those calculated in the present study (Row

[2]We compute a slightly different value of g_t from Eq. (45) in Ref. [153] (after a minor typographical error in Ref. [153] is corrected, as noted in Ref. [121]). We obtain the value of g_t to be 9.703 eVÅ^9 instead of 9.705 eVÅ^9 in Ref. [153] and the difference is due to the rounding-off of the input parameters that enter Eq. (45) in Ref. [153].

(i)). The small differences in values of the two sets of the elastic constants are due to the slight difference in the values of g_t. The values of the elastic constants calculated from MD simulations [78] are also tabulated in Row (v) of Table 5.2. The procedure for obtaining these MD results is similar to that used in Ref. [207] to obtain the elastic constants of Ni [208]. Lastly, we find that this parameterization of the PFC method yields the pressure at the solid-liquid coexistence of $P_u = 184.5$ GPa $= 1.821 \times 10^6$ atm.

We note that $H_{\alpha\beta}$ can be directly compared with *both* $C_{\alpha\beta}$ and $K_{\alpha\beta}$ only because the density profile used in this work is constructed so that $h_n(\xi, \phi_{ave})$ is minimized with respect to ξ at constant ϕ_{ave}. This construction makes the values of the PFC elastic constants, defined by the linear and nonlinear elasticity theories, identical; this justifies our comparisons between $H_{\alpha\beta}$ and $C_{\alpha\beta}$ and between $H_{\alpha\beta}$ and $K_{\alpha\beta}$. For a general form of a density profile, however, we can only directly compare the elastic constants that are defined from the same measure of deformation; in this work, the measure of deformation is either the Lagragian strain tensor or the small-strain tensor. Therefore, in the next section, we will propose a general procedure for calculating the two sets of PFC elastic constants: one defined by the linear elasticity theory and the other one defined by the nonlinear elasticity theory.

By comparing the PFC and TE elastic constants, we find that the PFC elastic constants, $H_{\alpha\beta}$, are equivalent to neither $C_{\alpha\beta}$ nor $K_{\alpha\beta}$; both sets of the TE elastic constants are significantly larger than $H_{\alpha\beta}$, especially for the 11-type constants. Therefore, we find that the PFC and TE elastic constants cannot be used interchangeably. Consequently, since the thermoelasticity theory is widely adopted, one should only use the TE elastic constants to make consistent comparisons of the elastic constants from the PFC method with those from other theories such as classical density functional theory [82, 83, 84], Monte Carlo [85], MD [86], and *ab initio* density functional theory [87, 88, 89].

The reasons for the discrepancies between the PFC and TE elastic constants can be understood by comparing Eqs. (5.22) and (5.27). The first difference is the frame in which the free energy density is measured. The difference leads to the different volume that divides the total free energy. The PFC elastic constants are derived from the free energy per unit deformed volume, while the TE elastic constants are obtained from the free energy per unit undeformed volume.

The second difference is whether or not ϕ_{ave} or ϕ'_{ave} is held constant when taking the second derivative of the free energy density with respect to the small deformation parameter. The constant-ϕ_{ave} condition, which is used to obtain the PFC elastic constants, causes the number of particles in the system to change when the volume of the system is changing during the quasi-static deformations. However, the constant-ϕ'_{ave} condition, which is used to obtain the TE elastic constants, is equivalent to keeping the total number of particles in the system constant during the deformations. Therefore, we find that the choices of the frame of reference and the different constraints imposed upon the quasi-static deformations contribute to the different values between the PFC and TE elastic constants.

Since $H_{\alpha\beta}$ cannot be compared with the elastic constants calculated using other theories, we will instead compare the TE elastic constants with those from the MD simulations [78]. We find that the values of 11- and 44-type constants for both $C_{\alpha\beta}$ and $K_{\alpha\beta}$ are significantly larger than those of the MD results. This discrepancy is not unexpected considering the fact that the model predicts a large pressure at the liquid-solid coexistence density $(1.821 \times 10^6 \text{ atm})^3$, while the potential in the MD simulations is constructed so that the predicted pressure is close to zero to model normal experimental conditions [209]. This indicates that the systems described by the PFC and MD simulations are in very different thermodynamic states. Therefore, a different set of PFC parameters that yields a reasonable value of pressure should

be obtained to improve the prediction of the elastic constants.

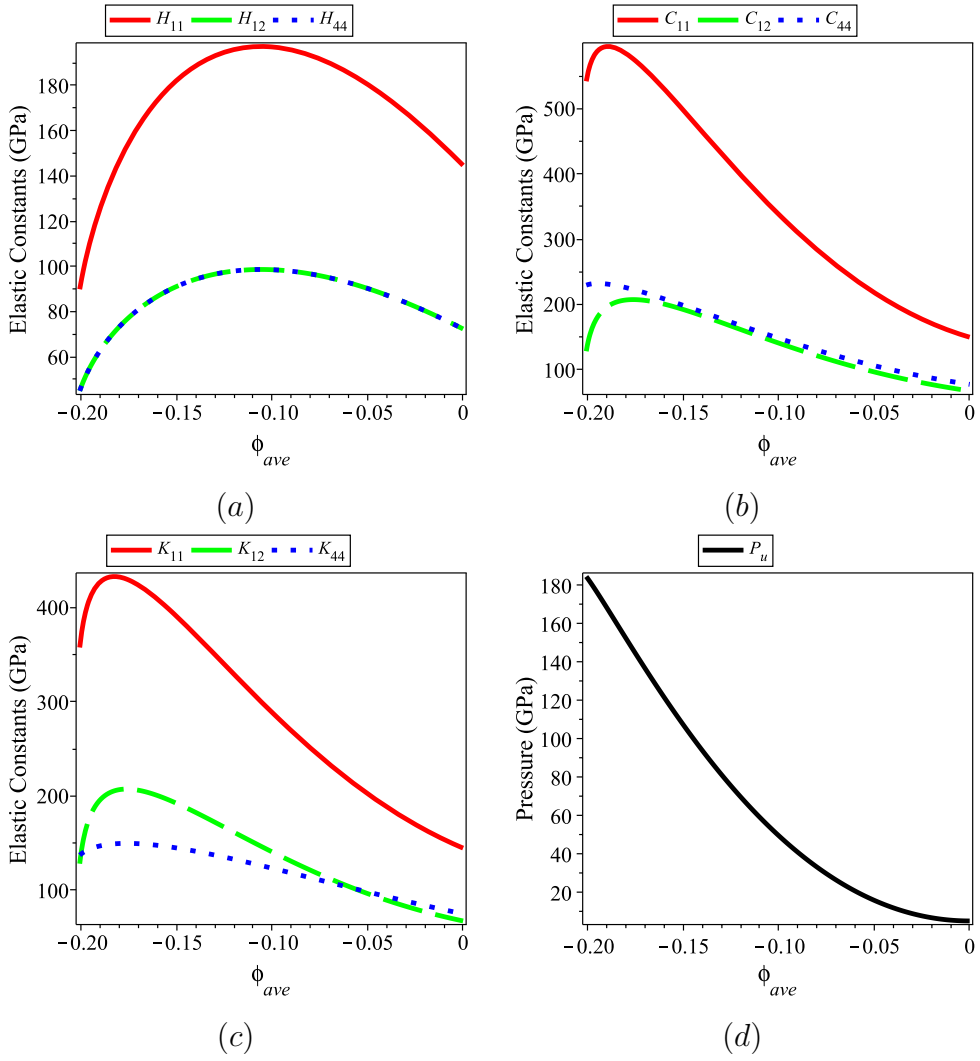

Figure 5.1: The plots of different sets of elastic constants and hydrostatic pressure as functions of ϕ_{ave}, or equivalently ϕ'_{ave}. (a) The PFC elastic constants. (b) The TE elastic constants in the nonlinear elasticity theory. (c) The TE elastic constant in the linear elasticity theory. (d) The hydrostatic pressure of the undeformed state.

[3]The BCC Fe at high pressure transforms to a hexagonal closed-pack (HCP) structure. Nevertheless, based on Fig. 2 in Ref. [210], the elastic constants of (metastable) BCC Fe under a pressure of 184.5 GPa are expected to be much higher than what we calculated ($C_{11} = 542.0$ GPa). From the figure, the value of C_{11} for a pressure of 40 GPa is approximately 450 GPa. Assuming a monotonic increase of the values of the elastic constants with increasing pressure, we expect the values of the elastic constants at a pressure of 184.5 GPa to be even higher than our calculated value.

	Elastic Constants	11-Type	12-Type	44-Type
(i)	$H_{\alpha\beta}$	89.8	44.9	44.9
(ii)	$C_{\alpha\beta}$	542.0	128.1	229.4
(iii)	$K_{\alpha\beta}$	357.5	128.1	137.2
(iv)	PFC-WAK	90.0	45.0	45.0
(v)	MD	128.0	103.4	63.9

Table 5.2: The elastic constants of BCC Fe at the melting point. The unit of the elastic constants is GPa. (i) The PFC elastic constants calculated in this work using slightly different parameters from those in Ref. [78] (see text). (ii) The TE elastic constants in the nonlinear elasticity theory. (iii) The TE elastic constants in the linear elasticity theory. (iv) The PFC elastic constants reported in Ref. [78]. (v) The elastic constants predicted by the MD simulations [78]. For (i) to (iv), the elastic constants are evaluated at $\phi_{ave} = -0.201$.

5.4 A General Procedure to Obtain the PFC Elastic Constants

Up to this point, we have introduced the TE elastic constants defined by the linear and nonlinear elasticity theories, which are K_{ijkl} and C_{ijkl}, respectively. However, we have not specified whether H_{ijkl} is defined by the linear or nonlinear elasticity theory. As we have mentioned in the previous section, this specification is not necessary for the particular form of the density profile used in this work because it minimizes $h_n(\xi, \phi_{ave})$ with respect to ξ at constant ϕ_{ave}. However, for a general form of a density profile, we need to be able to calculate the PFC elastic constants defined by both the linear and nonlinear elasticity theories. Therefore, a more general procedure than those presented in Section 5.3.1 is needed.

We first propose formal definitions of the PFC elastic constants from the second derivatives of the free energy density with respect to the elements of the strain tensors; these definitions are analogous to how the TE elastic constants are defined. By

considering the procedure in Section 5.3.1, the two possible choices are

$$\frac{\partial^2}{\partial E_{ij}\partial E_{kl}}\left(\frac{\mathcal{F}}{V}\right)\Bigg|_{\theta,\phi_{ave},E^*_{mn}} \equiv H^E_{ijkl} \tag{5.31}$$

and

$$\frac{\partial^2}{\partial \epsilon_{ij}\partial \epsilon_{kl}}\left(\frac{\mathcal{F}}{V}\right)\Bigg|_{\theta,\phi_{ave},\epsilon^*_{mn}} \equiv H^\epsilon_{ijkl}. \tag{5.32}$$

The elastic constants H^E_{ijkl} (H^ϵ_{ijkl}) are analogous to C_{ijkl} (K_{ijkl}) in the sense that they are defined by the nonlinear (linear) elasticity theory.

We then outline the procedure for calculating $H^E_{\alpha\beta}$ and $H^\epsilon_{\alpha\beta}$. Using a procedure similar to that used to obtain $C_{\alpha\beta}$, we can obtain $H^E_{\alpha\beta}$ from

$$\begin{aligned}
\mathcal{Q}^{PFC}_1 &= 3H^E_{11} + 6H^E_{12} - 3P^g_u \\
\mathcal{Q}^{PFC}_2 &= 2H^E_{11} - 2H^E_{12} - 2P^g_u \\
\mathcal{Q}^{PFC}_3 &= H^E_{44} - P^g_u,
\end{aligned} \tag{5.33}$$

where

$$P^g_u = -\frac{1}{3}\frac{\partial}{\partial \xi}\left(\frac{\mathcal{F}_1(\xi,\phi_{ave})}{V_1(\xi)}\right)\Bigg|^{\xi=0}_{\theta,\phi_{ave}}. \tag{5.34}$$

We emphasize that the partial derivative is performed with constant ϕ_{ave}. Finally, similar to how $K_{\alpha\beta}$ is related to $C_{\alpha\beta}$ from Eq. (5.18), we can relate $H^\epsilon_{\alpha\beta}$ to $H^E_{\alpha\beta}$ from the following relationships:

$$H^E_{11} = H^\epsilon_{11} + P^g_u, \qquad H^E_{12} = H^\epsilon_{12}, \qquad H^E_{44} = H^\epsilon_{44} + \frac{P^g_u}{2}. \tag{5.35}$$

When $P^g_u = 0$, $H^E_{\alpha\beta} = H^\epsilon_{\alpha\beta}$, which is the case for the choice of the density profile used

in this work. The term P_u^g is analogous to P_u in that it is proportional to the first derivative of the free energy density with respect to the deformation variable. However, the deformation process to obtain P_u^g is performed with constant ϕ_{ave} instead of ϕ'_{ave}. Furthermore, the free energy density to obtain P_u^g is measured with respect to the deformed frame instead of the undeformed frame. For the PFC free energy and the one-mode approximation given in Eq. (5.5), the value of P_u^g is equal to zero for all values of ϕ_{ave} because the form of the density profile minimizes $h_n(\xi, \phi_{ave})$ with respect to ξ at constant ϕ_{ave}. However, $P_u^g = 0$ does not correspond to $P_u = 0$ as we have shown in Fig. 5.1(d).

5.5 Thermodynamics of Stressed Solids

In this section, we use a thermodynamic formulation to define the PFC and TE elastic constants in a systematic manner. We then derive the relationships between the PFC and TE elastic constants, as well as those among other thermodynamic quantities resulting from Taylor expansions of thermodynamic energy functions. We discuss the implications of the relationships among the thermodynamic quantities and then present numerical verifications of the relationships between the PFC and TE elastic constants.

5.5.1 Formulation

In addition to the thermoelasticity theory [81, 79], we employ a thermodynamic theory of stressed solids by Larche and Cahn [90, 91] which considers the solid as a network of lattices and allows a description of vacancies. In this work, we consider only substitutional lattices which can be occupied by atomic species A and vacancies. The Helmholtz free energy of such a system can be written in the following form:

$$F_s = F_s(\theta, N_A, a_{ij}, R_i), \tag{5.36}$$

where N_A is the number of lattice sites occupied by atomic species A (not to be confused with the Avogadro's number), and the subscript s denotes that the material is a crystalline solid. The fact that F_s depends on only N_A and not the number of lattice sites occupied by vacancies comes from the assumption that the total number of lattice sites are conserved in all thermodynamic states. This assumption applies when there is no consideration of defects such as surfaces, grain boundaries, and dislocations that can alter the total number of lattice sites by acting as sources or sinks of vacancies [90]. Again, since we consider R_i as constant, we will omit this dependence subsequently.

From the form of F_s, we now redefine the stress and elastic constants in Eqs. (5.15), (5.16), and (5.17):

$$\begin{aligned} T^u_{ij} &= \frac{1}{\mathcal{V}}\frac{\partial F_s}{\partial E_{ij}}\bigg|^u_{\theta,E^*_{mn},N_A} = \frac{1}{\mathcal{V}}\frac{\partial F_s}{\partial \epsilon_{ij}}\bigg|^u_{\theta,\epsilon^*_{mn},N_A}, \\ C_{ijkl} &= \frac{1}{\mathcal{V}}\frac{\partial^2 F_s}{\partial E_{ij}\partial E_{kl}}\bigg|^u_{\theta,N_A,E^*_{mn}}, \\ K_{ijkl} &= \frac{1}{\mathcal{V}}\frac{\partial^2 F_s}{\partial \epsilon_{ij}\partial \epsilon_{kl}}\bigg|^u_{\theta,N_A,\epsilon^*_{mn}}, \end{aligned} \tag{5.37}$$

where the subscript N has been replaced by N_A and F has been replaced by F_s.

The next step is to formulate thermodynamic energy functions that allow different sets of elastic constants to be defined in a systematic manner. The energy function that can be used to define H^E_{ijkl} or H^ϵ_{ijkl} is

$$g_s \equiv \frac{F_s(\theta, a_{ij}, \rho_A)}{V}, \tag{5.38}$$

where $\rho_A = N_A/V$ is the number of the lattice sites occupied by atomic species A divided by the volume of the deformed system. On the other hand, the energy

function that can be used to calculate C_{ijkl} and K_{ijkl} is

$$f'_s \equiv \frac{F_s(\theta, a_{ij}, \rho'_A)}{\mathcal{V}}, \tag{5.39}$$

where $\rho'_A = N_A/\mathcal{V} = J\rho_A$ is the number of lattice sites occupied by atomic species A divided by the volume of the undeformed system. The reason for defining ρ'_A is that the condition of constant ρ'_A is the same as constant N_A because $\mathcal{V}$ is constant.

For completeness, one could define the other two energy functions:

$$\begin{aligned} g'_s &\equiv \frac{F_s(\theta, a_{ij}, \rho_A)}{\mathcal{V}}, \\ f_s &\equiv \frac{F_s(\theta, a_{ij}, \rho'_A)}{V}, \end{aligned} \tag{5.40}$$

which can be used to define the other two sets of elastic constants that are different from the PFC and TE elastic constants. We will not address these additional two sets of elastic constants in this work.

Regarding the notation, we use the letters g and f to indicate that the energy functions depend on ρ_A and ρ'_A, respectively. The use of a prime in f'_s, g'_s and ρ'_A indicates that the corresponding variables are quantities per unit volume of the undeformed system. Without the prime, f_s, g_s and ρ_A are quantities per unit volume of the deformed system.

Lastly, we define the quantities at the undeformed state as follows:

$$\begin{aligned} &\theta \to \theta_u, \qquad a_{ij} \to 0, \qquad \rho'_A \to \rho'_{Au}, \\ &\rho_A \to \rho'_{Au}, \qquad g_s \to g_{su}, \qquad f'_s \to f'_{su}, \end{aligned} \tag{5.41}$$

where $g_{su} = f'_{su}$.

5.5.2 Taylor Expansions of Energy Functions

We are now in the position to define the elastic constants as well as other thermodynamic quantities from the Taylor expansions of the energy functions. We expand the energy functions around the undeformed state with respect to a_{ij} and ρ_A or ρ'_A. For f'_s, we write the expansion as follows:

$$\begin{aligned} f'_s(\theta_u, a_{ij}, \rho'_{Au} + \Delta\rho'_A) &= f'_{su} + \mathcal{U}_s^{fp}\Delta\rho'_A + \mathcal{P}_{ij}^{fp}a_{ij} + \mathcal{D}_{ij}^{fp}\Delta\rho'_A a_{ij} \\ &\quad + \frac{1}{2}\mathcal{A}_s^{fp}(\Delta\rho'_A)^2 + \frac{1}{2}\mathcal{L}_{ijkl}^{fp}a_{ij}a_{kl}, \end{aligned} \tag{5.42}$$

where $\Delta\rho'_A = \rho'_A - \rho'_{Au}$, and

$$\begin{aligned} &f'_{su} = f'_s(\theta_u, 0, \rho'_{Au}), \qquad \mathcal{U}_s^{fp} = \left.\frac{\partial f'_s}{\partial \rho'_A}\right|_{\theta, a_{ij}}^{u}, \qquad \mathcal{P}_{ij}^{fp} = \left.\frac{\partial f'_s}{\partial a_{ij}}\right|_{\theta, a^*_{mn}, \rho'_A}^{u}, \\ &\mathcal{D}_{ij}^{fp} = \left.\frac{\partial}{\partial a_{ij}}\right|_{\theta, \rho'_A, a^*_{mn}}^{u} \left(\left.\frac{\partial f'_s}{\partial \rho'_A}\right|_{\theta, a_{kl}}\right), \qquad \mathcal{A}_s^{fp} = \left.\frac{\partial^2 f'_s}{\partial (\rho'_A)^2}\right|_{\theta, a_{ij}}^{u}, \qquad \mathcal{L}_{ijkl}^{fp} = \left.\frac{\partial^2 f'_s}{\partial a_{ij}\partial a_{kl}}\right|_{\theta, a^*_{mn}, \rho'_A}^{u}. \end{aligned} \tag{5.43}$$

The superscript u denotes that the partial derivatives are evaluated at the undeformed state, and the superscript fp denotes that the quantity is obtained from the Taylor expansion of f'_s. For the Taylor expansion of g_s, we write

$$\begin{aligned} g_s(\theta_u, a_{ij}, \rho'_{Au} + \Delta\rho_A) &= g_{su} + \mathcal{U}_s^{g}\Delta\rho_A + \mathcal{P}_{ij}^{g}a_{ij} + \mathcal{D}_{ij}^{g}\Delta\rho_A a_{ij} \\ &\quad + \frac{1}{2}\mathcal{A}_s^{g}(\Delta\rho_A)^2 + \frac{1}{2}\mathcal{L}_{ijkl}^{g}a_{ij}a_{kl}, \end{aligned} \tag{5.44}$$

where $\Delta\rho_A = \rho_A - \rho'_{Au}$, and

$$g_{su} = g_s(\theta_u, 0, \rho'_{Au}), \qquad \mathcal{U}^g_s = \left.\frac{\partial g_s}{\partial \rho_A}\right|^u_{\theta,a_{ij}}, \qquad \mathcal{P}^g_{ij} = \left.\frac{\partial g_s}{\partial a_{ij}}\right|^u_{\theta,a^*_{mn},\rho_A},$$
$$\mathcal{D}^g_{ij} = \left.\frac{\partial}{\partial a_{ij}}\right|^u_{\theta,\rho_A,a^*_{mn}} \left(\left.\frac{\partial g_s}{\partial \rho_A}\right|_{\theta,a_{kl}}\right), \qquad \mathcal{A}^g_s = \left.\frac{\partial^2 g_s}{\partial(\rho_A)^2}\right|^u_{\theta,a_{ij}}, \qquad \mathcal{L}^g_{ijkl} = \left.\frac{\partial^2 g_s}{\partial a_{ij}\partial a_{kl}}\right|^u_{\theta,a^*_{mn},\rho_A}. \tag{5.45}$$

The superscript g indicates that the corresponding quantity is from the Taylor expansion of g_s. Furthermore, whether a_{ij} refers to E_{ij} or ϵ_{ij} does not affect the values of $\mathcal{U}^x_s$, $\mathcal{P}^x_{ij}$, $\mathcal{A}^x_s$, and $\mathcal{D}^x_{ij}$, where the superscript x denotes either g or fp. However, the choice of E_{ij} or ϵ_{ij} affects the values of $\mathcal{L}^x_{ijkl}$, for a given x. Therefore, we define $\mathcal{C}^x_{ijkl} \equiv \mathcal{L}^x_{ijkl}$ for $a_{ij} = E_{ij}$, and $\mathcal{K}^x_{ijkl} \equiv \mathcal{L}^x_{ijkl}$ for $a_{ij} = \epsilon_{ij}$. As will be evident later, the quantities $\mathcal{L}^x_{ijkl}$ are the elastic constants.

We can relate the coefficients of the Taylor expansions to some of the quantities introduced previously. First, if we substitute $\phi_{ave} = \rho_A$ and $\mathcal{F} = F_s$ in Eqs. (5.31) and (5.32), it is clear from Eq. (5.45) and the definition of g_s in Eq. (5.38) that

$$\mathcal{C}^g_{ijkl} = H^E_{ijkl}, \quad \text{and} \quad \mathcal{K}^g_{ijkl} = H^\epsilon_{ijkl}. \tag{5.46}$$

In other words, the quantities $\mathcal{L}^g_{ijkl}$ (i.e., $\mathcal{C}^g_{ijkl}$ and $\mathcal{K}^g_{ijkl}$) are the PFC elastic constants.

Second, we show that $\mathcal{P}^{fp}_{ij}$ is equal to the stress tensor evaluated at the undeformed state by considering Eqs. (5.37) and (5.43):

$$\mathcal{P}^{fp}_{ij} = \left.\frac{\partial f'_s}{\partial a_{ij}}\right|^u_{\theta,a^*_{mn},\rho'_A} = \frac{1}{\mathcal{V}}\left.\frac{\partial F_s}{\partial a_{ij}}\right|^u_{\theta,a^*_{mn},N_A} = T^u_{ij}, \tag{5.47}$$

where we emphasize that constant ρ'_A is identical to constant N_A. However, $\mathcal{P}^g_{ij} \neq T^u_{ij}$ because the constant-ρ_A condition does not equal to the constant-N_A condition and because g_s is the free energy density measured with respect to the deformed frame

whereas f'_s is the free energy measured with respect to the undeformed frame. For isotropic pressure at the undeformed state, or $T^u_{ij} = -\delta_{ij} P_u$, the rotational invariance of the free energy requires the quantities $\mathcal{P}^x_{ij}$ and $\mathcal{D}^x_{ij}$ to be represented by scalar matrices (scalar multiples of the identity matrix) and we denote the value of their diagonal entries to be $\mathcal{P}^x_s$ and $\mathcal{D}^x_s$, respectively.

Third, from Eq. (5.43) and the definition of f'_s in Eq. (5.39), we can write

$$\mathcal{L}^{fp}_{ijkl} = \left.\frac{\partial^2 f'_s}{\partial a_{ij} \partial a_{kl}}\right|^u_{\theta, a^*_{mn}, \rho'_A} = \frac{1}{\mathcal{V}} \left.\frac{\partial^2 F_s}{\partial a_{ij} \partial a_{kl}}\right|^u_{\theta, a^*_{mn}, N_A}. \tag{5.48}$$

Comparing the above expression to that in Eq. (5.37), we obtain

$$\mathcal{C}^{fp}_{ijkl} = C_{ijkl}, \quad \text{and} \quad \mathcal{K}^{fp}_{ijkl} = K_{ijkl}, \tag{5.49}$$

which means that the quantities $\mathcal{L}^{fp}_{ijkl}$ (i.e., $\mathcal{C}^{fp}_{ijkl}$ and $\mathcal{K}^{fp}_{ijkl}$) are the TE elastic constants.

For a cubic material under isotropic pressure at the undeformed state, the relationships between $\mathcal{C}^x_{\alpha\beta}$ and $\mathcal{K}^x_{\alpha\beta}$ is analogous to those in Eq. (5.18):

$$\mathcal{C}^x_{11} = \mathcal{K}^x_{11} - \mathcal{P}^x_s, \qquad \mathcal{C}^x_{12} = \mathcal{K}^x_{12}, \qquad \mathcal{C}^x_{44} = \mathcal{K}^x_{44} - \frac{\mathcal{P}^x_s}{2}, \tag{5.50}$$

where we note that the sign of $\mathcal{P}^x_s$ is the opposite of the sign of P_u. These relationships are derived from the same procedure described from Eq. (B.1) to (B.6) in Appendix B.

5.5.3 Relationships Between the Coefficients of Taylor Expansions

We can now derive the relationships between the coefficients of the Taylor expansions. In particular, we are interested in the relationships between $H^E_{\alpha\beta}$ ($H^\epsilon_{\alpha\beta}$) and $C_{\alpha\beta}$ ($K_{\alpha\beta}$), which are essentially the relationships between $\mathcal{L}^{fp}_{\alpha\beta}$ and $\mathcal{L}^g_{\alpha\beta}$. This is obtained by substituting $\rho_A = \rho'_A / J$ and $g_s = f'_s / J$ into Eq. (5.44), using the following

expressions for J [92]:

$$J \to (1+\epsilon_{11})(1+\epsilon_{22})(1+\epsilon_{33}) \tag{5.51}$$

or

$$J \to \sqrt{(1+2E_{11})(1+2E_{22})(1+2E_{33})}, \tag{5.52}$$

depending on whether E_{ij} or ϵ_{ij} is considered. We then expand the resulting expression around the undeformed state and equate the coefficients of the Taylor expansion with those from Eq. (5.42). We obtain the following relationships:

$$\begin{aligned}
\mathcal{U}_s^{fp} &= \mathcal{U}_s^g \\
\mathcal{P}_s^{fp} &= \mathcal{P}_s^g - \mathcal{U}_s^g \rho'_{Au} + g_{su} \\
\mathcal{D}_s^{fp} &= \mathcal{D}_s^g - \mathcal{A}_s^g \rho'_{Au} \\
\mathcal{A}_s^{fp} &= \mathcal{A}_s^g.
\end{aligned} \tag{5.53}$$

When we consider $a_{ij} = E_{ij}$, we have

$$\begin{aligned}
\mathcal{C}_{11}^{fp} &= \mathcal{C}_{11}^g + \mathcal{A}_s^g (\rho'_{Au})^2 - 2\mathcal{D}_s^g \rho'_{Au} + 2\mathcal{P}_s^g + \mathcal{U}_s^g \rho'_{Au} - g_{su} \\
\mathcal{C}_{12}^{fp} &= \mathcal{C}_{12}^g + \mathcal{A}_s^g (\rho'_{Au})^2 - 2\mathcal{D}_s^g \rho'_{Au} + 2\mathcal{P}_s^g - \mathcal{U}_s^g \rho'_{Au} + g_{su}
\end{aligned} \tag{5.54}$$

and when $a_{ij} = \epsilon_{ij}$, we obtain

$$\begin{aligned}
\mathcal{K}_{11}^{fp} &= \mathcal{K}_{11}^g + \mathcal{A}_s^g (\rho'_{Au})^2 - 2\mathcal{D}_s^g \rho'_{Au} + 2\mathcal{P}_s^g \\
\mathcal{K}_{12}^{fp} &= \mathcal{K}_{12}^g + \mathcal{A}_s^g (\rho'_{Au})^2 - 2\mathcal{D}_s^g \rho'_{Au} + 2\mathcal{P}_s^g - \mathcal{U}_s^g \rho'_{Au} + g_{su}.
\end{aligned} \tag{5.55}$$

The relationships in Eqs. (5.54) and (5.55) above not only facilitate conversions

between the PFC and TE elastic constants, but also quantify the difference between the PFC and TE elastic constants in terms of thermodynamic quantities. These thermodynamic quantities are the coefficients of the Taylor expansion in Eq. (5.44), which can be related to the thermodynamic quantities from the Taylor expansion in Eq. (5.42) through the relationships in Eq. (5.53). For example, the quantity $\mathcal{P}_s^g$ in the above equation can be related to $\mathcal{P}_s^{fp}$, which is in turn equal to the negative of the pressure evaluated at the undeformed state ($-P_u$).

The thermodynamic quantities that quantify the difference between the PFC and TE elastic constants depend on the specific parameterization of the model and in general are nonzero. Furthermore, these quantities pertain to the undeformed state that is characterized by the limit of strain approaching zero (or the limit of ξ approaching zero). Therefore, we conclude that these quantities do not generally vanish at the zero-strain limit, which also implies that the PFC and TE elastic constants are not generally identical at this limit.

We now present verifications of Eqs. (5.54) and (5.55) from numerical calculations. Specifically, we compare the values of $\mathcal{C}_{\alpha\beta}^{fp}$ and $\mathcal{K}_{\alpha\beta}^{fp}$ calculated from two different procedures. The first procedure is described in Section 5.3.2, which is how we obtained the TE elastic constants. We denote the resulting quantities $\mathcal{C}_{\alpha\beta}^{fp1}$ and $\mathcal{K}_{\alpha\beta}^{fp1}$. The second procedure is to use Eqs. (5.54) and (5.55), and we denote the resulting values $\mathcal{C}_{\alpha\beta}^{fp2}$ and $\mathcal{K}_{\alpha\beta}^{fp2}$. To use the second procedure, we calculate $\mathcal{C}_{\alpha\beta}^{g}$ and $\mathcal{K}_{\alpha\beta}^{g}$ from the procedure in Section 5.4, which is the general procedure to calculate the PFC elastic constants. We also need to calculate the values of $\mathcal{P}_s^g$, $\mathcal{D}_s^g$, $\mathcal{U}_s^g$, $\mathcal{A}_s^g$, g_{su}, and ρ'_{Au} from the following equations:

$$\mathcal{P}_s^g = \frac{1}{3}\frac{\partial}{\partial \xi}\left(\frac{\mathcal{F}_1(\xi,\phi_{ave})}{V_1(\xi)}\right)\Bigg|_{\theta,\phi_{ave}}^{\xi=0}, \tag{5.56}$$

$$\mathcal{D}_s^g = \frac{1}{3}\frac{\partial}{\partial \xi}\bigg|_{\theta,\phi_{ave}}^{\xi=0} \left(\frac{\partial}{\partial \phi_{ave}} \left(\frac{\mathcal{F}_1(\xi,\phi_{ave})}{V_1(\xi)} \right) \bigg|_{\theta,\xi} \right), \tag{5.57}$$

$$\mathcal{U}_s^g = \frac{\partial}{\partial \phi_{ave}} \left(\frac{\mathcal{F}_n(\xi,\phi_{ave})}{V_n(\xi)} \right) \bigg|_{\theta,\xi}^{\xi=0}, \tag{5.58}$$

$$\mathcal{A}_s^g = \frac{\partial^2}{\partial \phi_{ave}^2} \left(\frac{\mathcal{F}_n(\xi,\phi_{ave})}{V_n(\xi)} \right) \bigg|_{\theta,\xi}^{\xi=0}, \tag{5.59}$$

$$g_{su} = \mathcal{F}_n(\xi,\phi_{ave})\big|^{\xi=0}, \tag{5.60}$$

$$\rho'_{Au} = \phi_{ave}\big|^{\xi=0} = \phi'_{ave}. \tag{5.61}$$

We note that since $\mathcal{C}_{\alpha\beta}^g$ and $\mathcal{K}_{\alpha\beta}^g$ and the quantities from Eqs. (5.56) to (5.60) are evaluated at the undeformed state, they can be equivalently expressed as functions of ϕ_{ave} or ϕ'_{ave}. Also, Eqs. (5.56) and (5.57) only apply to the isotropic deformation ($n = 1$) whereas Eqs. (5.58) to (5.61) is valid for all types of deformation. We verify that $\mathcal{C}_{11}^{fp1} = \mathcal{C}_{11}^{fp2}$ and $\mathcal{C}_{12}^{fp1} = \mathcal{C}_{12}^{fp2}$ from Figs. 5.2(a) and 5.2(b), respectively. We also show that $\mathcal{K}_{11}^{fp1} = \mathcal{K}_{11}^{fp2}$ and $\mathcal{K}_{12}^{fp1} = \mathcal{K}_{12}^{fp2}$ from Figs. 5.2(c) and 5.2(d), respectively. These results validate the relationships in Eqs. (5.54) and (5.55).

We do not report the relationship between $\mathcal{L}_{44}^{fp}$ and $\mathcal{L}_{44}^g$ from the method used to obtain Eqs. (5.54) and (5.55) because the method does not yield a correct result. The reason is that the definitions of J in Eqs. (5.51) and (5.52) only apply to the deformations where the angles of the cubic unit cell are not distorted [92], which is apparent from the fact that no off-diagonal elements of the strain tensors are present

in either Eq. (5.51) or (5.52). Unfortunately, there is no general form of J in terms of E_{ij} and ϵ_{ij} alone that would apply to all types of affine deformation.[4] Therefore, we can only obtain the correct relationships for the elastic constants that are defined from the second derivatives of the diagonal elements of the strain tensors. This issue is a topic for future investigation.

5.6 Chapter Summary

We have investigated the methods for calculating the isothermal elastic constants using the PFC method and found that the procedure outlined in Refs. [64, 65, 78] is not consistent with the definitions from the theory of thermoelasticity of stressed materials [79, 80, 81]. The PFC elastic constants (from the procedure outlined in Refs. [64, 65, 78]) are calculated from variations in the free energy density associated with various types of quasi-static deformations at a constant average number density. In this work, we proposed an alternative procedure for calculating the elastic constants (termed the TE elastic constants in this article) that are consistent with the definitions from the thermoelasticity theory. The TE elastic constants are calculated from variations in the total free energy per undeformed volume associated with quasi-static deformations at a constant number of particles in the system. Comparing the conventional and the proposed procedures, we found that the discrepancies between the PFC and TE elastic constants result from the choices of the frame of reference used to calculate the free energy density and the different constraints imposed upon the quasi-static deformations. The numerical results using an existing PFC model for BCC Fe show that the two procedures can yield significantly different values of the elastic constants. Therefore, the TE elastic constants should be used when parameterizing the PFC model.

[4] In order to obtain a general form of J, one can either express J in terms of u_{ij} or supplement ϵ_{ij} with ω_{ij}.

Furthermore, we derived the relationships between the PFC and the TE elastic constants using the energy functions formulated from the thermodynamic theory of stressed solids [90, 91, 92]. These relationships were obtained by performing Taylor expansions of and changes of variables to the energy functions. From the relationships, we have quantified the differences between the PFC and TE elastic constants in terms of thermodynamic quantities such as the pressure of the undeformed state.

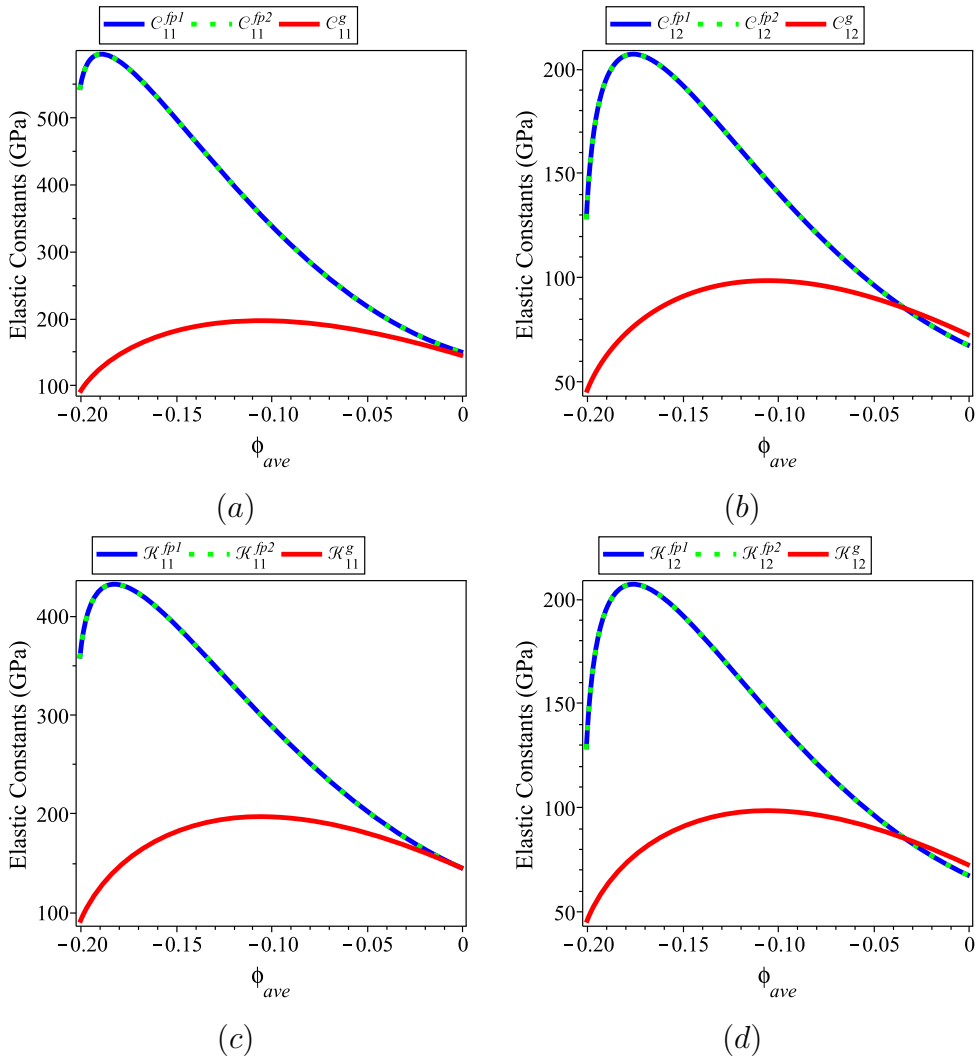

Figure 5.2: The plots of elastic constants as functions of ϕ_{ave}, or equivalently ϕ'_{ave}. The elastic constants $\mathcal{C}_{\alpha\beta}^{fp1}$ and $\mathcal{K}_{\alpha\beta}^{fp1}$ are calculated from the procedure described in Section 5.3.2, which is similar to how the TE elastic constants are obtained. The elastic constants $\mathcal{C}_{\alpha\beta}^{fp2}$ and $\mathcal{K}_{\alpha\beta}^{fp2}$ are obtained from Eqs. (5.54) and (5.55) which in turn employ the values of $\mathcal{C}_{\alpha\beta}^{g}$ and $\mathcal{K}_{\alpha\beta}^{g}$ calculated from the procedure in Section 5.4.

CHAPTER VI

Conclusion

In this thesis, we have performed computational studies of morphological evolution in metallic-nanostructure heteroepitaxy and associated model development. Through these studies, we have made three main contributions. The first contribution is an investigation of an energetic pathway from 2D to 3D morphologies of internal-defect-free magnetic thin films. Considering the energetics of the misfit strain, misfit dislocations, film surface and interface, we have identified the existence of a driving force for solid-state dewetting for a single crystal, internal-defect-free film in which other dewetting mechanisms mediated by grain boundaries or impurities are absent. We have also shown how non-monotonic dependencies of the surface/interfacial energy on film thickness, arising from the electronic effects, can give rise to the metastability of flat films with certain thicknesses. Thus, our discovery has furthered an understanding of thermodynamic driving force behind morphological evolution in magnetic-nanostructure heteroepitaxy, which is crucial to the development of techniques for fabricating nanostructures.

Our second contribution is the numerical techniques to improve the prediction capabilities of classical density functional theory (CDFT) and the phase-field crystal (PFC) method, both of which are promising tools for modeling material phenomena due to their atomic-scale resolutions and diffusive time scales. Specifically, we have

proposed a rational function fit (RFF) to describe the two-body direct correlation (DCF) in Fourier space. The DCF contains atomic-scale structural information and represents atomic interactions in the CDFT and PFC formulations. The RFF allows flexibility in capturing and altering specific features of the two-body DCF. This flexibility allows us to increase the numerical efficiency of the CDFT model through reduction of the short-wavelength contributions in the density profile while still retaining most of the model's accuracy. Also, the combination of the RFF with the conventional polynomial fit further provides flexibility in manipulating the DCF in the PFC model. Thus, our technique is a part of an ongoing effort to make CDFT and PFC method viable material modeling tools.

As our third contribution, we have investigated the methods for calculating isothermal elastic constants using the PFC method and found that the procedure outlined in Refs. [64, 65, 78] is not consistent with the definitions from the theory of thermoelasticity of stressed materials [79, 80, 81]. Since the PFC model often utilizes elastic properties to parameterize the model, it is important that they are computed in a manner that is consistent with experiments and other types of simulations. We have proposed an alternative procedure for calculating, using the PFC method, the elastic constants that are consistent with the definitions from the thermoelasticity theory. Furthermore, we have quantified the differences between the elastic constants calculated using the conventional method and the proposed method using the energy functions formulated from the thermodynamic theory of stressed solids [90, 91, 92]. This quantification not only facilitates conversions among the different sets of elastic constants but also provides quantitative measures of the differences among them. The impact of our work is that we have provided a thermodynamically consistent method to parameterize the PFC method in order to consistently predict material properties.

CHAPTER VII

Future Work

Building on our contributions, one can further an understanding of underlying mechanisms behind morphological evolution in magnetic-nanostructure heteroepitaxy by employing the CDFT or PFC model with appropriate parameterization to real material systems. Using these tools, one can study the thermodynamics of the morphological evolution, which is similar to our work based on continuum mechanics, but without restrictions on the structure of the misfit dislocations or the morphology of the film. This study will give insights into how the system's evolution will be thermodynamically driven when there are multiple strain-relaxation mechanisms (such as surface instability and misfit dislocation formation) occurring simultaneously.

The CDFT and PFC model not only allow one to perform thermodynamics studies, but also simulations of morphological evolution of an epitaxial system. In other words, the kinetics of the growth is taken into account; this consideration is important because the epitaxial growth can undergo a non-equilibrium process [48]. One can employ these modeling tools developed here to study morphological evolution in situations where kinetic processes are important such as those occuring at low temperature and/or with high deposition rate [49]. This study will be beneficial not only for fundamental understanding of the growth mechanisms, but also for designing and improving technology of fabricating nanostructures.

APPENDICES

APPENDIX A

Gaussian Approximation of Density Profiles

We present a method to construct an approximate density profile using a Gaussian function. We assume that the atomic probability density around each lattice site located at $\mathbf{R}_i$ is represented by a Gaussian function of the form:

$$G(\mathbf{r}, \mathbf{R}_i) = \left(\frac{\alpha_g}{\pi}\right)^{3/2} \exp\left(-\alpha_g |\mathbf{r} - \mathbf{R}_i|^2\right), \tag{A.1}$$

where the parameter α_g controls the peak width. We can construct the approximate scaled atomic probability density profile, $n_g(\mathbf{r})$, with an scaled average density of $\bar{n}$ from a summation of the individual Gaussian peaks:

$$n_g(\mathbf{r}) = \frac{\bar{n}}{G_{ave}} \sum_i G(\mathbf{r}, \mathbf{R}_i), \tag{A.2}$$

where

$$G_{ave} = \frac{1}{V} \int_V \sum_i G(\mathbf{r}, \mathbf{R}_i) d\mathbf{r}. \tag{A.3}$$

The semi-analytical method utilized in this work minimizes the free energy as a function of $\bar{n}$ with respect to α_g and the lattice spacing. We note that this method

does not enforce the integral of the density to be the number of atoms in the volume; this implies that there can be vacancies or interstitials in the system.

APPENDIX B

Taylor Expansion of the Helmholtz Free Energy

In this section, the Taylor expansion of the Helmholtz free energy in Eq. (5.14) is performed in order to derive the definitions shown in Eqs. (5.15), (5.16) and (5.17). The expansion of $F(\theta, E_{ij}, N)$ with respect to E_{ij} around the undeformed state gives [202]

$$F(\theta, E_{ij}, N) = F(\theta, 0, N) + \mathcal{V} T^u_{ij} E_{ij} + \frac{\mathcal{V}}{2} C_{ijkl} E_{ij} E_{kl} + ..., \tag{B.1}$$

where T^u_{ij} and C_{ijkl} are the coefficients of expansions written as

$$T^u_{ij} = \frac{1}{\mathcal{V}} \frac{\partial F}{\partial E_{ij}} \bigg|^u_{\theta, E^*_{mn}, N}, \tag{B.2}$$

and

$$C_{ijkl} = \frac{1}{\mathcal{V}} \frac{\partial^2 F}{\partial E_{ij} \partial E_{kl}} \bigg|^u_{\theta, E^*_{mn}, N}, \tag{B.3}$$

respectively. These are the definitions in Eqs. (5.15) and (5.16).

From the expansion in Eq. (B.1), one can change the variables from E_{ij} to u_{ij} using Eq. (5.10), and subsequently change the variables from u_{ij} to ϵ_{ij} and ω_{ij} by

using Eq. (5.13). The resulting expansion is

$$F(\theta,\epsilon_{ij},N) = F(\theta,0,N) + \mathcal{V}T^u_{ij}\left(\epsilon_{ij} + \frac{1}{2}(\epsilon_{mi}+\omega_{mi})(\epsilon_{mj}+\omega_{mj})\right) + \frac{\mathcal{V}}{2}C_{ijkl}\epsilon_{ij}\epsilon_{kl} + ..., \tag{B.4}$$

where we omit the higher-order terms in ϵ_{ij} and ω_{ij} for brevity, and we also use the symmetric property of ϵ_{ij} and antisymmetric property of ω_{ij} to simplify the above expression. Despite the fact that the above expression contains both ϵ_{ij} and ω_{ij}, the free energy must still be dependent on only ϵ_{ij} and not on ω_{ij} due to the requirement that the free energy be rotationally invariant [81]. By rearranging the above expression and omitting terms with ω_{ij}, we obtain

$$F(\theta,\epsilon_{ij},N) = F(\theta,0,N) + \mathcal{V}T^u_{ij}\epsilon_{ij} + \frac{\mathcal{V}}{2}K_{ijkl}\epsilon_{ij}\epsilon_{kl} + ..., \tag{B.5}$$

where

$$K_{ijkl} = C_{ijkl} + \frac{1}{4}(T^u_{ik}\delta_{jl} + T^u_{il}\delta_{jk} + T^u_{jk}\delta_{il} + T^u_{jl}\delta_{ik}). \tag{B.6}$$

For a cubic material under isotropic pressure, P_u, where $T^u_{ij} = -P_u\delta_{ij}$, Eq. (B.6) simplifies to Eq. (5.18).

From Eq. (B.5), we can write an alternative definition of T^u_{ij},

$$T^u_{ij} = \frac{1}{\mathcal{V}}\frac{\partial F}{\partial \epsilon_{ij}}\bigg|^u_{\theta,\epsilon^*_{mn},N}, \tag{B.7}$$

and define another set of elastic constants,

$$K_{ijkl} = \frac{1}{\mathcal{V}}\frac{\partial^2 F}{\partial \epsilon_{ij}\partial\epsilon_{kl}}\bigg|^u_{\theta,\epsilon^*_{mn},N}. \tag{B.8}$$

These are the definitions in Eqs. (5.15) and (5.17).

APPENDIX C

Calculations of $K_{\alpha\beta}$

In this section, we discuss two issues that arise when the elastic constants $K_{\alpha\beta}$ are calculated from the procedure similar to the one used to obtain $C_{\alpha\beta}$ in Section 5.3.2. We illustrate the first issue by using this procedure to calculate $K_{\alpha\beta}$. We first calculate $Q_n^{TE}(\phi'_{ave})$ from Eq. (5.27) and then use the chain rule to transform the partial derivative as follows:

$$\frac{\partial^2}{\partial\xi^2} = \frac{\partial^2\epsilon_{ij}}{\partial\xi^2}\frac{\partial}{\partial\epsilon_{ij}} + \frac{\partial\epsilon_{ij}}{\partial\xi}\frac{\partial\epsilon_{kl}}{\partial\xi}\frac{\partial^2}{\partial\epsilon_{ij}\partial\epsilon_{kl}}, \tag{C.1}$$

Using the above equation to transform the partial derivative in Eq. (5.27), we obtain

$$\begin{aligned} Q_1^{TE}(\phi'_{ave}) &= 3K_{11} + 6K_{12} = 3C_{11} + 6C_{12} - 3P_u, \\ Q_2^{TE}(\phi'_{ave}) &= 2K_{11} - 2K_{12} = 2C_{11} - 2C_{12} - 2P_{,u} \\ Q_3^{TE}(\phi'_{ave}) &= K_{44} \qquad\qquad\quad = C_{44} - P_u, \end{aligned} \tag{C.2}$$

where the second equality in each line is taken from Eq. (5.29) for comparison. From Eq. (C.2), we find that the relationship between K_{44} and C_{44} is different from that given in Eq. (5.18), which indicates that K_{44} calculated from the procedure above

is inconsistent with the definition given by the thermoelasticity theory in Eq. (5.17). The second issue when using the above procedure to calculate $K_{\alpha\beta}$ is that the resulting value of $K_{\alpha\beta}$ will depend on the choice of deformation, which contradicts the fact that elastic constants are material properties.

In order to understand the cause of these issues, we first consider why the procedure from Eqs. (5.26) to (5.29) can be used to calculate $C_{\alpha\beta}$. The reason is that the Taylor expansion of $\mathcal{F}_n(\xi, \phi'_{ave})$ from Eq. (5.26) with respect to ξ around the undeformed state,

$$\mathcal{F}_n(\xi, \phi'_{ave}) = \mathcal{F}_n(0, \phi'_{ave}) + \left.\frac{\partial \mathcal{F}_n(\xi, \phi'_{ave})}{\partial \xi}\right|_{\xi=0} \xi + \frac{\mathcal{V}}{2} Q_n^{TE}(\phi'_{ave})\xi^2 + ..., \tag{C.3}$$

is equivalent to the Taylor expansion,

$$\mathcal{F}_n(E_{ij}(\xi), \phi'_{ave}) = \mathcal{F}_n(0, \phi'_{ave}) + \mathcal{V} T_{ij} E_{ij}(\xi) + \frac{\mathcal{V}}{2} C_{ijkl} E_{ij}(\xi) E_{kl}(\xi) + ..., \tag{C.4}$$

for all deformation types up to the second-order terms in ξ. This equality is the underlying assumption in Eq. (5.29) and we confirm this equality by the fact that we obtain the same values of C_{ijkl} for all types of deformation.

However, we find that, due to the small-strain approximation, the expansion in Eq. (C.3) is not equivalent to the Taylor expansion,

$$\mathcal{F}_n(\epsilon_{ij}(\xi), \phi'_{ave}) = \mathcal{F}_n(0, \phi'_{ave}) + \mathcal{V} T_{ij} \epsilon_{ij}(\xi) + \frac{\mathcal{V}}{2} K_{ijkl} \epsilon_{ij}(\xi) \epsilon_{kl}(\xi) + ..., \tag{C.5}$$

for all deformation types up to the second-order terms in ξ. Therefore, the equality in Eq. (C.2) will not be valid in general, and we have to instead calculate $K_{\alpha\beta}$ from Eq. (5.18). With this alternative method, we confirm that the same values of $K_{\alpha\beta}$ are obtained regardless of the choice of deformation types.

BIBLIOGRAPHY

BIBLIOGRAPHY

[1] J. Drucker. Self-assembling Ge(Si)/Si(100) quantum dots. IEEE Journal of Quantum Electronics, 38(8):975, 2002.

[2] A. D. Yoffe. Low-dimensional systems: Quantum size effects and electronic properties of semiconductor microcrystallites (zero-dimensional systems) and some quasi-two-dimensional systems. Advances in Physics, 51(2):799, 2002.

[3] A. D. Yoffe. Semiconductor quantum dots and related systems: Electronic, optical, luminescence and related properties of low dimensional systems. Advances in Physics, 50(1):1, 2001.

[4] F. Ratto and F. Rosei. Order and disorder in the heteroepitaxy of semiconductor nanostructures. Materials Science and Engineering: R: Reports, 70(3-6):243, 2010.

[5] M. N. Baibich, J. M. Broto, A. Fert, F. N. Vandau, F. Petroff, P. Eitenne, G. Creuzet, A. Friederich, and J. Chazelas. Giant magnetoresistance of (001)Fe/(001)Cr magnetic superlattices. Physical Review Letters, 61(21):2472, 1988.

[6] G. Binasch, P. Grunberg, F. Saurenbach, and W. Zinn. Enhanced magnetoresistance in layered magnetic-structures with antiferromagnetic interlayer exchange. Physical Review B, 39(7):4828, 1989.

[7] J. Barnaś and I. Weymann. Spin effects in single-electron tunnelling. Journal of Physics: Condensed Matter, 20(42):423202, 2008.

[8] D. Brambley, B. Martin, and P. D. Prewett. Microlithography: An overview. Advanced Materials for Optics and Electronics, 4(2):55, 1994.

[9] G. Cao and Y. Wang. Nanostructures and Nanomaterials: Synthesis, Properties, and Applications. Imperial College Press, London, 2004.

[10] L. F. Thompson and M. J. Bowden. Introduction to Microlithography. The American Chemical Society, Washington, DC, 1983.

[11] G. R. Brewer. Electron-Beam Technology in Microelectronic Fabrication. Academic Press, New York, 1980.

[12] T. M. Hall, A. Wagner, and L. F. Thompson. Ion beam exposure characteristics of resists. Journal of Vacuum Science and Technology, 16(6):1889, 1979.

[13] D. M. Eigler and E. K. Schweizer. Positioning single atoms with a scanning tunnelling microscope. Nature, 344(6266):524, 1990.

[14] C. Baur, A. Bugacov, B. E. Koel, A. Madhukar, N. Montoya, T. R. Ramachandran, A. A. G. Requicha, R. Resch, and P. Will. Nanoparticle manipulation by mechanical pushing: underlying phenomena and real-time monitoring. Nanotechnology, 9(4):360, 1998.

[15] W. M. Moreau. Semiconductor Lithography: Principles and Materials. Plenum, New York, 1988.

[16] R. S. Wagner. Whisker Technology. Wiley, New York, 1970.

[17] M. Ohring. Materials Science of Thin Films. Academic Press, 2001.

[18] H. Brune, M. Giovannini, K. Bromann, and K. Kern. Self-organized growth of nanostructure arrays on strain-relief patterns. Nature, 394(6692):451, 1998.

[19] M. Volmer and A. Weber. Keimbildung in übersättigten gebilden. Zeitschrift für Physikalische Chemie, 119:277, 1926.

[20] J. de la Figuera, J. E. Prieto, C. Ocal, and R. Miranda. Scanning-tunneling-microscopy study of the growth of cobalt on Cu(111). Physical Review B, 47(19):13043, 1993.

[21] F. C. Frank and J. H. van der Merwe. One dimensional dislocations. I. Static theory. Proceedings of the Royal Society A, 198:205, 1949.

[22] F. C. Frank and J. H. van der Merwe. One-dimensional dislocations. II. Misfitting monolayers and oriented overgrowth. Proceedings of the Royal Society A, 198:216, 1949.

[23] F. C. Frank and J. H. van der Merwe. One-dimensional dislocations. III. Influence of the second harmonic term in the potential representation, on the properties of the model. Proceedings of the Royal Society A, 200:125, 1949.

[24] H. Jenniches, M. Klaua, H. Hoche, and J. Kirschner. Comparison of pulsed laser deposition and thermal deposition: Improved layer-by-layer growth of Fe/Cu(111). Applied Physics Letters, 69(22):3339, 1996.

[25] I. N. Stranski and L. Krastanov. Zur theorie der orientierten ausscheidung von ionenkristallen aufeinander. Sitzungsber. Akad. Wiss. Wien, Math.-naturwiss. Kl., 146:797, 1938.

[26] O. Fruchart, P. O. Jubert, M. Eleoui, F. Cheynis, B. Borca, P. David, V. Santonacci, A. Lienard, M. Hasegawa, and C. Meyer. Growth modes of Fe(110) revisited: a contribution of self-assembly to magnetic materials. Journal of Physics: Condensed Matter, 19(5):053001, 2007.

[27] D. Sander, A. Enders, C. Schmidthals, D. Reuter, and J. Kirschner. Mechanical stress and magnetism of ferromagnetic monolayers. Surface Science, 402–404(0):351–355, 1998.

[28] I. V. Markov. Crystal Growth for Beginners: Fundamentals of Nucleation, Crystal Growth, and Epitaxy. World Scientific, Singapore, 1995.

[29] Y. Pang and R. Huang. Nonlinear effect of stress and wetting on surface evolution of epitaxial thin films. Physical Review B, 74(7):075413, 2006.

[30] P. Sutter and M. Lagally. Nucleationless three-dimensional island formation in low-misfit heteroepitaxy. Physical Review Letters, 84(20):4637, 2000.

[31] R. Tromp, F. Ross, and M. Reuter. Instability-driven SiGe island growth. Physical Review Letters, 84(20):4641, 2000.

[32] R. J. Asaro and W. A. Tiller. Interface morphology development during stress corrosion cracking: Part I. Via surface diffusion. Metallurgical and Materials Transactions B, 3:1789, 1972.

[33] M. A. Grinfeld. Instability of the interface between a nonhydrostatically stressed elastic body and a melt. Akademiia Nauk SSSR Doklady, 290:1358, 1986.

[34] D. E. Jesson, K. M. Chen, S. J. Pennycook, T. Thundat, and R. J. Warmack. Morphological evolution of strained films by cooperative nucleation. Physical Review Letters, 77(7):1330, 1996.

[35] P. O. Jubert, O. Fruchart, and C. Meyer. Self-assembled growth of faceted epitaxial Fe(110) islands on Mo(110)/Al2O3(1110). Physical Review B, 64(11):115419, 2001.

[36] P. O. Jubert, O. Fruchart, and C. Meyer. Magnetic properties of step-decorated Fe nanostripes and dots grown on Mo(110). Journal of Magnetism and Magnetic Materials, 242:565, 2002.

[37] W. L. Ling, T. Giessel, K. Thurmer, R. Q. Hwang, N. C. Bartelt, and K. F. McCarty. Crucial role of substrate steps in de-wetting of crystalline thin films. Surface Science, 570(3):L297, 2004.

[38] K. F. McCarty, J. C. Hamilton, Y. Sato, A. Saa, R. Stumpf, J. de la Figuera, K. Thuermer, F. Jones, A. K. Schmid, A. A. Talin, and N. C. Bartelt. How metal films de-wet substrates-identifying the kinetic pathways and energetic driving forces. New Journal of Physics, 11:043001, 2009.

[39] D. J. Srolovitz and S. A. Safran. Capillary instabilities in thin-films .1. Energetics. Journal of Applied Physics, 60(1):247, Jan 1986.

[40] W. W. Mullins. Theory of thermal grooving. Journal of Applied Physics, 28(3):333, 1957.

[41] C. M. Kennefick and R. Raj. Copper on Sapphire - Stability of thin-films at 0.7-Tm. Acta Metallurgica, 37(11):2947, 1989.

[42] F. R. N. Nabarro. Dislocations in a simple cubic lattice. Proceedings of the Physical Society, 59(332):256, 1947.

[43] R. Peierls. The size of a dislocation. Proceedings of the Physical Society, 52:34, 1940.

[44] J. Malzbender, M. Przybylski, J. Giergiel, and J. Kirschner. Epitaxial growth of Fe on Mo(110) studied by scanning tunneling microscopy. Surface Science, 414(1-2):187, 1998.

[45] H. Bethge, D. Heuer, C. Jensen, K. Reshoft, and U. Kohler. Misfit-related effects in the epitaxial growth of Iron on W(110). Surface Science, 331-333:878, 1995.

[46] S. Murphy, D. M. Mathuna, G. Mariotto, and I. V. Shvets. Morphology and strain-induced defect structure of ultrathin epitaxial Fe films on Mo(110). Physical Review B, 66(19):195417, 2002.

[47] I. V. Shvets, S. Murphy, and V. Kalinin. Nanowedge island formation on Mo(110). Surface Science, 601(15):3169, 2007.

[48] A. Enders, R. Skomski, and J. Honolka. Magnetic surface nanostructures. Journal of Physics: Condensed Matter, 22(43):433001, 2010.

[49] I. Röder, E. Hahn, I. Brune, J. P. Buoher, and K. Kern. Building one-and two-dimensional nanostructures by diffusion-controlled aggregation at surfaces. Nature, 366:141, 1993.

[50] A. F. Voter. Introduction to the Kinetic Monte Carlo Method, in Radiation Effects in Solids. Springer, NATO Publishing Unit, Dordrecht, The Netherlands, 2005.

[51] J. Heulens and N. Moelans. On the rotation invariance of multi-order parameter models for grain growth. Scripta Materialia, 62(11):827, 2010.

[52] R. Kobayashi, J. A. Warren, and W. C. Carter. Vector-valued phase field model for crystallization and grain boundary formation. Physica D-Nonlinear Phenomena, 119:415, 1998.

[53] R. Kobayashi, J. A. Warren, and W. C. Carter. A continuum model of grain boundaries. Physica D-Nonlinear Phenomena, 140:141, 2000.

[54] N. Moelans, B. Blanpain, and P. Wollants. Quantitative analysis of grain boundary properties in a generalized phase field model for grain growth in anisotropic systems. Physical Review B, 78(2):024113, 2008.

[55] N. Moelans, B. Blanpain, and P. Wollants. Quantitative phase-field approach for simulating grain growth in anisotropic systems with arbitrary inclination and misorientation dependence. Physical Review Letters, 101(2):025502, 2008.

[56] B. Morin, K. R. Elder, M. Sutton, and M. Grant. Model of the Kinetics of Polymorphous Crystallization. Physical Review Letters, 75(11):2156, 1995.

[57] Y. M. Jin and A. G. Khachaturyan. Phase field microelasticity theory of dislocation dynamics in a polycrystal: model and three-dimensional simulations. Philosophical Magazine Letters, 81(9):607, 2001.

[58] D. Rodney, Y. Le Bouar, and A. Finel. Phase field methods and dislocations. Acta Materialia, 51(1):17, 2003.

[59] Y. U. Wang, Y. M. Jin, A. M. Cuitino, and A. G. Khachaturyan. Nanoscale phase field microelasticity theory of dislocations: Model and 3d simulations. Acta Materialia, 49(10):1847, 2001.

[60] Y. Wang and J. Li. Phase field modeling of defects and deformation. Acta Materialia, 58(4):1212, 2010.

[61] R. Evans. Nature of the liquid-vapor interface and other topics in the statistical-mechanics of nonuniform, classical fluids. Advances in Physics, 28(2):143, 1979.

[62] R. Evans. Fundamentals of Inhomogeneous Fluids. Marcel Dekker, New York, 1992.

[63] Y. Singh. Density-functional theory of freezing and properties of the ordered phase. Physics Reports (Review Section of Physics Letters), 207(6):1, 1991.

[64] K. R. Elder, M. Katakowski, M. Haataja, and M. Grant. Modeling elasticity in crystal growth. Physical Review Letters, 88(24):245701, 2002.

[65] K. R. Elder and M. Grant. Modeling elastic and plastic deformations in nonequilibrium processing using phase field crystals. Physical Review E, 70(5):051605, 2004.

[66] N. Provatas, J. A. Dantzig, B. Athreya, P. Chan, P. Stefanovic, N. Goldenfeld, and K. R. Elder. Using the phase-field crystal method in the multi-scale modeling of microstructure evolution. JOM, 59(7):83, 2007.

[67] T. V. Ramakrishnan and M. Yussouff. First-principles order-parameter theory of freezing. Physical Review B, 19(5):2775, 1979.

[68] T.V. Ramakrishnan. Density wave theory of freezing and the solid. Pramana, 22(3-4):365, 1984.

[69] A. J. Archer and R. Evans. Dynamical density functional theory and its application to spinodal decomposition. Journal of Chemical Physics, 121(9):4246, 2004.

[70] U. M. B. Marconi and P. Tarazona. Dynamic density functional theory of fluids. Journal of Physics: Condensed Matter, 12(8A):A41, 2000.

[71] U. M. B. Marconi and P. Tarazona. Dynamic density functional theory of fluids. Journal of Chemical Physics, 110(16):8032, 1999.

[72] A. F. Volter. Hyperdynamics: accelerated molecular dynamics of infrequent events. Physical Review Letters, 78(20):3908, 1997.

[73] A. F. Volter. A method for accelerating the molecular dynamics simulation of infrequent events. Journal of Chemical Physics, 106(11):4665, 1997.

[74] J. Li, S. Sarkar, W. T. Cox, T. J. Lenosky, E. Bitzek, and Y. Wang. Diffusive molecular dynamics and its application to nanoindentation and sintering. Physical Review B, 84(5):054103, 2011.

[75] D. W. Oxtoby and R. Evans. Nonclassical nucleation theory for the gas–liquid transition. Journal of Chemical Physics, 89(12):7521, 1988.

[76] K. R. Elder, N. Provatas, J. Berry, P. Stefanovic, and M. Grant. Phase-field crystal modeling and classical density functional theory of freezing. Physical Review B, 75(6):064107, 2007.

[77] J. Swift and P.C. Hohenherg. Hydrodynamic fluctuations at convective instability. Physical Review A, 15(1):319, 1977.

[78] K.-A. Wu, A. Adland, and A. Karma. Phase-field-crystal model for FCC ordering. Physical Review E, 81(6):061601, 2010.

[79] D. C. Wallace. Solid State Physics, volume 25. Academic Press, New York, 1970.

[80] D. C. Wallace. Thermodynamics of Crystals. Dover Publications, New York, 1998.

[81] D. C. Wallace. Thermoelasticity of stressed materials and comparison of various elastic constants. Physical Review, 162(3):776, 1967.

[82] H. Xu and M. Baus. Elastic constants of the hard-sphere solid from density-functional theory. Physical Review A, 38(8):4348, 1988.

[83] G. L. Jones. Elastic-constants in density-functional theory. Molecular Physics, 61(2):455, 1987.

[84] B. B. Laird. Weighted-density-functional theory calculation of elastic-constants for face-centered-cubic and body-centered-cubic hard-sphere crystals. Journal of Chemical Physics, 97(4):2699, 1992.

[85] K. J. Runge and G. V. Chester. Monte-carlo determination of the elastic-constants of the hard-sphere solid. Physical Review A, 36(10):4852, 1987.

[86] S. K. Schiferl and D. C. Wallace. Elastic-constants of crystalline-Sodium from molecular-dynamics. Physical Review B, 31(12):7662, 1985.

[87] O Beckstein, J. E. Klepeis, G. L. W. Hart, and O Pankratov. First-principles elastic constants and electronic structure of -Pt2Si and PtSi. Physical Review B, 63(13):134112, 2001.

[88] K. B. Panda and K. S. Ravi Chandran. First principles determination of elastic constants and chemical bonding of titanium boride (TiB) on the basis of density functional theory. Acta Materialia, 54(6):1641–1657, 2006.

[89] G. V. Sin'ko and N. A. Smirnov. Ab initio calculations of elastic constants and thermodynamic properties of BCC, FCC, and HCP Al crystals under pressure. Journal Of Physics: Condensed Matter, 14(29):6989, 2002.

[90] F. Larché and J. W. Cahn. Linear theory of thermochemical equilibrium of solids under stress. Acta Metallurgica, 21(8):1051, 1973.

[91] F. Larché and J. W. Cahn. Non-linear theory of thermochemical equilibrium of solids under stress. Acta Metallurgica, 26(1):53, 1978.

[92] P. W. Voorhees and W. C. Johnson. Solid State Physics, volume 59. Elsevier Academic Press, 2004.

[93] V. Volterra. Sur l'équilibre des corps élastiques multiplement connexes. Annales Scientifiques de l'Ecole Normale Superieure, 24:401, 1907.

[94] J. H. van der Merwe. Crystal interfaces. II. Finite overgrowths. Journal of Applied Physics, 34(1):123, 1963.

[95] J. H. van der Merwe. Crystal interfaces. I. Semi-infinite crystals. Journal of Applied Physics, 34(1):117, 1963.

[96] J. Hirth and J. Lothe. Theory of Dislocations. John Wiley and Sons, Inc., 1982.

[97] J. H. Michell. On the direct determination of stress in an elastic solid, with application to the theory of plates. Proceedings of the London Mathematical Society, 1899.

[98] A. E. H. Love. Treatise on the Mathematical Theory of Elasticity, page 152. Dover Publications, 1927.

[99] J. Frenkel. The theory of the elastic limit and the solidity of crystal bodies. Zeitschrift für Physik, 37(7/8):572, 1926.

[100] J. D. Eshelby. Edge dislocations in anisotropic materials. Philosophical Magazine, 40(308):903, 1949.

[101] J. H. van der Merwe. Misfitting monolayers and oriented over-growth. Faraday Discussions, 5:201, 1949.

[102] J. H. van der Merwe. On the stresses and energies associated with inter-crystalline boundaries. Proceedings of the Physical Society. Section A, 63:616, 1950.

[103] J. H. van der Merwe. Equilibrium structure of a thin expitaxial film. Journal of Applied Physics, 41(11):4725, 1970.

[104] J. Frenkel and T. Kontorova. On the theory of plastic deformation and twinning. Physikalische Zeitschrift der Sowjetunion, 13:1, 1938.

[105] A. J. Foreman, M. A. Jaswon, and J. K. Wood. Factors controlling dislocation widths. Proceedings of the Physical Society. Section A, 64(374):156, 1951.

[106] C. A. B. Ball and J.H. van der Merwe. On bonding and structure of epitaxial bicrystals I. Semi-infinite crystals. Physica Status Solidi (b), 38(1):335, 1970.

[107] A. J. E. Foreman. Dislocation energies in anisotropic crystals. Acta Metallurgica, 3(4):322, 1955.

[108] V. Vitek. Intrinsic stacking faults in body-centred cubic crystals. Philosophical Magazine, 18(154):773, 1968.

[109] B. Joos and M.S. Duesbery. The Peierls stress of dislocations: an analytic formula. Physical Review Letters, 78(2):266, 1997.

[110] S. Kibey, J. B. Liu, D. D. Johnson, and H. Sehitoglu. Generalized planar fault energies and twinning in Cu-Al alloys. Applied Physics Letters, 89(19):191911, 2006.

[111] C. Brandl, P. M. Derlet, and H. Van Swygenhoven. General-stacking-fault energies in highly strained metallic environments: Ab initio calculations. Physical Review B, 76(5):054124, 2007.

[112] L. D. Landau and E. M. Lifshitz. Statistical Physics. Pergamon, Oxford, 1958.

[113] N. Provatas and K. Elder. Phase-Field Methods in Materials Science and Engineering. Wiley-VCH, 2010.

[114] A. G. Khachatryan. Theory of Structural Transformation in Solids. John Wiley and Sons, Inc., New York, 1983.

[115] H. E. Cook, D. de Fontaine, and J. E. Hilliard. A model for diffusion on cubic lattices and its application to the early stages of ordering. Acta Metallurgica, 17(6):765, 1969.

[116] M.C. Cross and P.C. Hohenberg. Pattern-formation outside of equilibrium. Reviews of Modern Physics, 65(3, Part 2):851, 1993.

[117] A. Jaatinen. Extended phase diagram of the three-dimensional phase field crystal model. Journal Of Physics: Condensed Matter, 22:205402, 2010.

[118] R. Prieler, J. Hubert, D. Li, B. Verleye, R. Haberkern, and H. Emmerich. An anisotropic phase-field crystal model for heterogeneous nucleation of ellipsoidal colloids. Journal Of Physics: Condensed Matter, 21(46):464110, 2009.

[119] H. Löwen. A phase-field-crystal model for liquid crystals. Journal Of Physics: Condensed Matter, 22(36):364105, 2010.

[120] S. van Teeffelen, R. Backofen, A. Voigt, and H. Löwen. Derivation of the phase-field-crystal model for colloidal solidification. Physical Review E, 79(5):051404, 2009.

[121] A. Jaatinen, C. V Achim, K. R Elder, and T Ala-Nissila. Thermodynamics of BCC metals in phase-field-crystal models. Physical Review E, 80(3):031602, 2009.

[122] M. Greenwood, N. Provatas, and J. Rottler. Free energy functionals for efficient phase field crystal modeling of structural phase transformations. Physical Review Letters, 105(4):045702, 2010.

[123] Z.-F. Huang, K. R. Elder, and N. Provatas. Phase-field-crystal dynamics for binary systems: Derivation from dynamical density functional theory, amplitude equation formalism, and applications to alloy heterostructures. Physical Review E, 82(2):021605, 2010.

[124] J. Berry, K. R. Elder, and M. Grant. Melting at dislocations and grain boundaries: A phase field crystal study. Physical Review B, 77(22):224114, 2008.

[125] J. Berry, K. R. Elder, and M. Grant. Simulation of an atomistic dynamic field theory for monatomic liquids: freezing and glass formation. Physical Review E, 77(6):061506, 2008.

[126] G. Tegze, L. Gránásy, G. I. Tóth, and F. Podmaniczky. Diffusion-controlled anisotropic growth of stable and metastable crystal polymorphs in the phase-field crystal model. Physical Review Letters, 103(3):035702, 2009.

[127] A. J. Archer and M. Rauscher. Dynamical density functional theory for interacting brownian particles: stochastic or deterministic? Journal of Physics A: Mathematical and General, 37(40):9325, 2004.

[128] S. W. Rick and A. D. J. Haymet. Density functional theory for the freezing of Lennard-Jones binary-mixtures. Journal of Chemical Physics, 90(2):1188, 1989.

[129] A. J. Archer. Dynamical density functional theory: binary phase-separating colloidal fluid in a cavity. Journal of Physics: Condensed Matter, 17(10):1405, 2005.

[130] K. R. Elder, Z.-F. Huang, and N. Provatas. Amplitude expansion of the binary phase-field-crystal model. Physical Review E, 81(1):011602, 2010.

[131] G. I. Tóth, G. Tegze, T. Pusztai, G. I. Tóth, and L. Gránásy. Polymorphism, crystal nucleation and growth in the phase-field crystal model in 2D and 3D. Journal of Physics: Condensed Matter, 22(36):364101, 2010.

[132] K. R. Elder, K. Thornton, and J. J. Hoyt. The Kirkendall effect in the phase field crystal model. Philosophical Magazine, 91(1):151, 2011.

[133] M. Greenwood, J. Rottler, and N. Provatas. Phase-field-crystal methodology for modeling of structural transformations. Physical Review E, 83(3):031601, 2011.

[134] M. Bestehorn and H. Haken. Transient patterns of the convection instability: A model-calculation. Zeitschrift fur Physik B Condensed Matter, 57:329, 1984.

[135] H. Herrero, C. Perez-Garcia, and M. Bestehorn. Stability of fronts separating domains with different symmetries in hydrodynamical instabilities. Chaos: An Interdisciplinary Journal of Nonlinear Science, 4(1):15, 1994.

[136] C. Kubstrup, H. Herrero, and C. Pérez-García. Fronts between hexagons and squares in a generalized swift-hohenberg equation. Physical Review E, 54(2):1560, 1996.

[137] K.-A. Wu and M. Plapp. Controlling crystal symmetries in phase-field crystal models. Journal of Physics: Condensed Matter, 22:364102, 2010.

[138] M. A. Choudhary, D. Li, H. Emmerich, and H. Löwen. DDFT calibration and investigation of an anisotropic phase-field crystal model. Journal Of Physics: Condensed Matter, 23(26):265005, 2011.

[139] R. Wittkowski, H. Löwen, and H. R. Brand. Derivation of a three-dimensional phase-field-crystal model for liquid crystals from density functional theory. Physical Review E, 82(3):031708, 2010.

[140] C. Achim, R. Wittkowski, and H. Löwen. Stability of liquid crystalline phases in the phase-field-crystal model. Physical Review E, 83(6):061712, 2011.

[141] P. Stefanovic, M. Haataja, and N. Provatas. Phase-field crystals with elastic interactions. Physical Review Letters, 96(22):225504, 2006.

[142] P. Stefanovic, M. Haataja, and N. Provatas. Phase field crystal study of deformation and plasticity in nanocrystalline materials. Physical Review E, 80(4):046107, 2009.

[143] S. Ichikawa, K. Miyazawa, H. Ichinose, and K. Ito. The microstructure of deformed nanocrystalline Ag and Ag/Fe alloy. Nanostructured Materials, 11(8):1301, 1999.

[144] K. S. Kumar, H. van Swygenhoven, and S. Suresh. Mechanical behavior of nanocrystalline metals and alloys. Acta Materialia, 51(19):5743, 2003.

[145] P. Galenko and D. Danilov. Phase-field-crystal and Swift-Hohenberg equations with fast dynamics. Physical Review E, 79(5):051110, 2009.

[146] P. Galenko and D. Jou. Diffuse-interface model for rapid phase transformations in nonequilibrium systems. Physical Review E, 71(4):046125, 2005.

[147] S. Majaniemi and M. Grant. Dissipative phenomena and acoustic phonons in isothermal crystals: A density-functional theory study. Physical Review B, 75(5):054301, 2007.

[148] N. Goldenfeld, B. P. Athreya, and J. A. Dantzig. Renormalization group approach to multiscale modelling in materials science. Journal of Statistical Physics, 125(5/6):1019, 2006.

[149] B. P. Athreya, N. Goldenfeld, and J. A Dantzig. Renormalization-group theory for the phase-field crystal equation. Physical Review E, 74(1):011601, 2006.

[150] N. Goldenfeld, B. P. Athreya, and J.A. Dantzig. Renormalization group approach to multiscale simulation of polycrystalline materials using the phase field crystal model. Physical Review E, 72(2):020601, 2005.

[151] B. P. Athreya, N. Goldenfeld, J. A. Dantzig, M. Greenwood, and N. Provatas. Adaptive mesh computation of polycrystalline pattern formation using a renormalization-group reduction of the phase-field crystal model. Physical Review E, 76(5):056706, 2007.

[152] D.-H. Yeon, Z.-F. Huang, K. R. Elder, and K. Thornton. Density-amplitude formulation of the phase-field crystal model for two-phase coexistence in two and three dimensions. Philosophical Magazine, 90(1-4):237, 2010.

[153] K.-A. Wu and A. Karma. Phase-field crystal modeling of equilibrium BCC-liquid interfaces. Physical Review B, 76(18):184107, 2007.

[154] K.-A. Wu, A. Karma, J. J. Hoyt, and M. Asta. Ginzburg-Landau theory of crystalline anisotropy for BCC-liquid interfaces. Physical Review B, 73(9):094101, 2006.

[155] S. Majaniemi and N. Provatas. Deriving surface-energy anisotropy for phenomenological phase-field models of solidification. Physical Review E, 79(1):011607, 2009.

[156] N. Provatas and S. Majaniemi. Phase-field-crystal calculation of crystal-melt surface tension in binary alloys. Physical Review E, 82(4):041601, 2010.

[157] J. W. Matthews. Dislocations in Solids, volume 2. North-Holland, Amsterdam, 1979.

[158] R. Popescu, H. L. Meyerheim, D. Sander, J. Kirschner, P. Steadman, O. Robach, and S. Ferrer. Surface X-ray structure analysis of periodic misfit dislocations in Fe/W(110). Physical Review B, 68(15):155421, 2003.

[159] Y. Yao, T. Wang, and C. Wang. Peierls-Nabarro model of interfacial misfit dislocation: An analytic solution. Physical Review B, 59(12):8232, 1999.

[160] R. C. Cammarata, K. Sieradzki, and F. Spaepen. Simple model for interface stresses with application to misfit dislocation generation in epitaxial thin films. Journal of Applied Physics, 87(3):1227, 2000.

[161] J. R. Willis, S. C. Jain, and R. Bullough. The energy of an array of dislocations: implications for strain relaxation in semiconductor heterostructures. Philosophical Magazine A, 62(1):115, 1990.

[162] S. Nakahara. Van der Merwe misfit dislocation theory: reconsideration of the Peierls-Nabarro model. Thin Solid Films, 72(1):171, 1980.

[163] N. Takeuchi, C. T. Chan, and K. M. Ho. Au(111) - A theoretical-study of the surface reconstruction and the surface electronic-structure. Physical Review B, 43(17):13899, 1991.

[164] G. Kresse and J. Hafner. Ab-initio molecular-dynamics simulation of the liquid-metal amorphous-semiconductor transition in Germanium. Physical Review B, 49(20):14251, 1994.

[165] G. Kresse and J. Furthmuller. Efficient iterative schemes for ab initio total-energy calculations using a plane-wave basis set. Physical Review B, 54(16):11169, 1996.

[166] G. Kresse and J. Furthmuller. Efficiency of ab-initio total energy calculations for metals and semiconductors using a plane-wave basis set. Computational Materials Science, 6(1):15, 1996.

[167] P. E. Blochl. Projector augmented-wave method. Physical Review B, 50(24):17953, 1994.

[168] G. Kresse and D. Joubert. From ultrasoft pseudopotentials to the projector augmented-wave method. Physical Review B, 59(3):1758, 1999.

[169] J. P. Perdew, K. Burke, and M. Ernzerhof. Generalized gradient approximation made simple. Physical Review Letters, 77(18):3865, 1996.

[170] N. Pisutha-arnond, B. Yang, D. H. Lim, M. Asta, and K. Thornton. Stability of strained thin films with interface misfit dislocations: A multiscale computational study. Thin Solid Films, 519:809, 2010.

[171] M. D. J. Powell. Numerical Methods for Nonlinear Algebraic Equations. Gordon and Breach, London, 1970.

[172] J. W. Cahn. Segregation to Interfaces. American Society for Metals, Ohio, 1978.

[173] B. Yang, T. Muppidi, V. Ozolins, and M. Asta. First-principles theory of nanoscale pattern formation in ultrathin alloy films: A comparative study of Fe-Ag on Ru(0001) and Mo(110) substrates. Physical Review B, 77(20):205408, 2008.

[174] R. C. Cammarata. Surface and interface stress effects in thin films. Progress in Surface Science, 46(1):1, 1994.

[175] K.-A. Wu. (private communication).

[176] J. Mellenthin, A. Karma, and M. Plapp. Phase-field crystal study of grain-boundary premelting. Physical Review B, 78(18):184110, 2008.

[177] D. Y. Sun, M. Asta, J. J. Hoyt, M. I. Mendelev, and D. J. Srolovitz. Crystal-melt interfacial free energies in metals: fcc versus bcc. Physical Review B, 69(2), 2004.

[178] L. N. Trefethen and D. Bau III. Numerical Linear Algebra. SIAM, Philadelphia, 1997.

[179] A. Greenbaum. Iterative Methods for Solving Linear Systems, volume 17 of Frontiers in Applied Mathematics. SIAM, Philadelphia, 1997.

[180] H. A. van der Vorst. Iterative Krylov methods for large linear systems, volume 13 of Cambridge Monographs on Applied and Computational Mathematics. Cambridge University Press, Cambridge, 2003.

[181] D. M. Young. Iterative Solution of Large Linear Systems. Academic Press, Inc., 1971.

[182] P. R. Amestoy, I. S. Duff, J.-Y. L'Excellent, and J. Koster. A fully asynchronous multifrontal solver using distributed dynamic scheduling. SIAM Journal on Matrix Analysis and Applications, 23(1):15, 2001.

[183] P. R. Amestoy, A. Guermouche, J.-Y. L'Excellent, and S. Pralet. Hybrid scheduling for the parallel solution of linear systems. Parallel Computing, 32(2):136, 2006.

[184] O. Schenk and K. Gärtner. On fast factorization pivoting methods for sparse symmetric indefinite systems. Electronic Transactions on Numerical Analysis, 23:158, 2006.

[185] O. Schenk and K. Gärtner. Solving unsymmetric sparse systems of linear equations with PARDISO. Future Generation Computer Systems, 20(3):475, 2004.

[186] X. S. Li and J. W. Demmel. SuperLU DIST: A scalable distributed-memory sparse direct solver for unsymmetric linear systems. ACM Transactions on Mathematical Software, 29(2):110, 2003.

[187] Y. A. Erlangga. Advances in iterative methods and preconditioners for the Helmholtz equation. Archives of Computational Methods in Engineering, 15(1):37, 2008.

[188] O. G. Ernst and M. J. Gander. Why is it difficult to solve Helmholtz problems with classical iterative methods. Numerical Analysis of Multiscale Problems, 83:325, 2012.

[189] G. R. Hadley. A complex Jacobi iterative method for the indefinite Helmholtz equation. Journal of Computational Physics, 203(1):358, 2005.

[190] Y. Saad and M. H. Schultz. GMRES - A generalized minimal residual algorithm for solving nonsymmetric linear-systems. SIAM Journal on Scientific and Statistical Computing, 7(3):856, 1986.

[191] M. Frigo and S. G. Johnson. The design and implementation of FFTW3. Proceedings of the IEEE, 93(2):216, 2005.

[192] S. Filippone. Applied Parallel Computing: Computations in Physics, Chemistry and Engineering Science, volume 1041 of Lecture Notes in Computer Science. Springer-Verlag, Berlin/Heidelberg, 1995.

[193] D. Pekurovsky. P3DFFT: A framework for parallel computations of Fourier transforms in three dimensions. Siam Journal on Scientific Computing, 34(4):C192, 2012.

[194] M. Cheng and J. A. Warren. An efficient algorithm for solving the phase field crystal model. Journal of Computational Physics, 227(12):6241, 2008.

[195] H. Gomez and X. Nogueira. An unconditionally energy-stable method for the phase field crystal equation. Computer Methods in Applied Mechanics and Engineering, 249-252(C):52, 2012.

[196] Z. Hu, S. M. Wise, C. Wang, and J. S. Lowengrub. Stable and efficient finite-difference nonlinear-multigrid schemes for the phase field crystal equation. Journal of Computational Physics, 228(15):5323, 2009.

[197] G. Tegze, G. Bansel, G. I. Tóth, T. Pusztai, Z. Fan, and L. Gránásy. Advanced operator splitting-based semi-implicit spectral method to solve the binary phase-field crystal equations with variable coefficients. Journal of Computational Physics, 228(5):1612, 2009.

[198] C. Wang and S. M. Wise. An energy stable and convergent finite-difference scheme for the modified phase field crystal equation. Siam Journal on Numerical Analysis, 49(3):945, 2011.

[199] S. Yamakawa and S-A. Hyodo. Gaussian finite-element mixed-basis method for electronic structure calculations. Physical Review B, 71(3):035113, 2005.

[200] V. Gavini, K. Bhattacharya, and M. Ortiz. Quasi-continuum orbital-free density-functional theory: A route to multi-million atom non-periodic DFT calculation. Journal of the Mechanics and Physics of Solids, 55(4):697, 2007.

[201] M. Iyer and V. Gavini. A field theoretical approach to the quasi-continuum method. Journal of the Mechanics and Physics of Solids, 59(8):1506, 2011.

[202] J. H. Weiner. Statistical Mechanics of Elasticity. Dover, 2002.

[203] A. G. McLellan. The Classical Thermodynamics of Deformable Materials. Cambridge Monographs on Physics. Cambridge University Press, New York, 1980.

[204] B. B. Karki, L. Stixrude, S. J. Clark, M. C. Warren, G. J. Ackland, and J. Crain. Structure and elasticity of MgO at high pressure. American Mineralogist, 82:51, 1997.

[205] G. Steinle-Neumann, L. Stixrude, and R. E. Cohen. First-principles elastic constants for the hcp transition metals Fe, Co, and Re at high pressure. Physical Review B, 60(2):791, 1999.

[206] D. J. Rasky and F. Milstein. Pseudopotential theoretical study of the alkali metals under arbitrary pressure: density, bulk modulus, and shear moduli. Physical Review B, 33(4):2765, 1986.

[207] S. M. Foiles. Temperature dependence of grain boundary free energy and elastic constants. Scripta Materialia, 62(5):231, 2010.

[208] S. M. Foiles. private communication.

[209] M. I. Mendelev, S. Han, D. J. Srolovitz, G. J. Ackland, D. Y. Sun, and M. Asta. Development of new interatomic potentials appropriate for crystalline and liquid iron. Philosophical Magazine, 83(35):3977, 2003.

[210] X. Sha and R. E. Cohen. First-principles thermoelasticity of BCC Iron under pressure. Physical Review B, 74(21):214111, 2006.